UNIVERSITY
OF TRENTO - Italy
Department of Physics

CONFINDUSTRIA TRENTO

POLO
MECCATRONICA
Impresa Innovazione Formazione

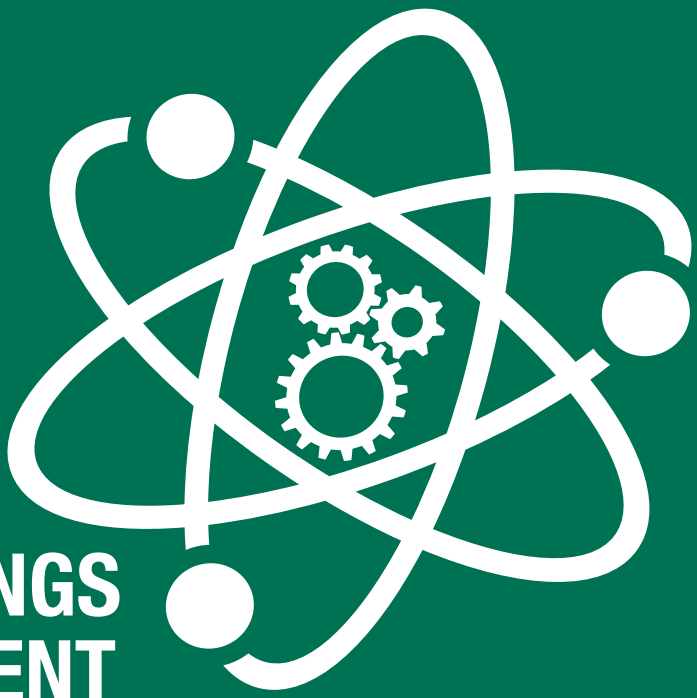

# PROCEEDINGS OF THE EVENT

# INDUSTRIAL PROBLEM SOLVING WITH PHYSICS

## Trento (Italy)
## July 18 – 23, 2016




# Proceedings of the event

Industrial Problem Solving with Physics

Trento, July 18 – 23, 2016

**Editors**
Maddalena Bertolla
Claudio Castellan
David Roilo

Trento
Università degli Studi di Trento

Proceedings of the event Industrial Problem Solving with Physics. Trento, July 18 – 23, 2016 / editors Maddalena Bertolla, Claudio Castellan, David Roilo. - Trento: Università degli Studi di Trento, 2016. - 87 p.: ill. - ISBN: 978-88-8443-712-9.


Document Class available at `https://github.com/mrgrass/IPSP_latex_Class`

# PREFACE

Confindustria Trento has been a partner of IPSP since the very first edition. When the founders of the competition - three PhD students of the Physics Department of the University of Trento - presented us their idea, we decided to join the project mainly for three reasons. First of all, it is a bottom-up initiative, managed by proactive students. Moreover, it contributes to promote the role of graduates and PhD students in Physics within the industrial sector. Finally, it can really help to narrow the gap between research and industry.
So far, our experience with IPSP has been extremely positive. Companies who have participated in IPSP have obtained innovative solutions to their technical problems, with important effects on their products and productive processes.
For these reasons we will support IPSP in the future too. Let's innovate together!

*Alessandro Santini, Confindustria Trento*

Industrial Problem Solving with Physics reached its third edition in 2016. In three editions ten companies and almost one hundred students have participated. From a Technology Transfer perspective, this unique event consolidates a new model of industry-academia collaborations which allows industrial problems to be solved quickly and effectively in just one week.
This model is consistent with "traditional" technology transfer tools; from the three editions of Industrial Problem Solving with Physics different technology transfer initiatives have been generated such as new patents, collaborative research projects, industrial doctoral programs. Furthermore, the project allows the reinforcement of collaboration between the University of Trento, Trentino Sviluppo - Polo Meccatronica and Confindustria Trento. During 2017 Industrial Problem Solving with Physics will be included as a best practice in technology transfer in a publication printed by ItaliaDecide.

*Vanessa Ravagni, Research Support and Knowledge Transfer Division,*
*University of Trento*

Trentino Sviluppo strongly believes in the potential of the Physics students' fresh minds which are involved in IPSP. As a matter of fact, IPSP is based on the very same foundations as Trentino Sviluppo's project Polo Meccatronica, a technology-industry park in which no boundary exists between research, industry and training, which collaborate with the aim of solving common problems and meeting the challenges posed by the industrial revolution called "Industry 4.0".
Gathering together the know-how of companies and a touch of "rational madness" that only young, unbiased students possess allows us to break from the usual way of thinking imposed by industrial production and encourages the development of creative ideas.
Recognizing the importance of the synergy between the world of education and that of business, Polo Meccatronica confirms its commitment to involve the companies settled within it also in the next edition of IPSP.

*Paolo Gregori, Polo Meccatronica*

# INTRODUCTION

Industrial Problem Solving with Physics (IPSP) is an event organized by the Department of Physics, the Doctorate School in Physics and the Research Support and Knowledge Transfer Division of the University of Trento, in collaboration with Confindustria Trento and Trentino Sviluppo – Polo Meccatronica.

The aim of this initiative is to promote the collaboration between the Department of Physics and the industrial world. What is new is that the idea comes from three PhD students, who decided to propose and organize it in 2014. Due to its great success, IPSP has reached its third edition, and also this year the Scientific Committee of IPSP2016 is composed of three PhD students in Physics. The Advisory Board, made up of the representatives of the co-organizers, supported by the Scientific Committee.
During IPSP, the participants work in teams to solve the problems presented by the participating companies, and in one week they have to find an answer to them. The "brains" comprise master's students, PhD students and research fellows working in the scientific area. The satisfaction of the participating companies proves that the skills of physicists represent a resource to find alternative solutions to industrial problems.
In this third edition of the event, some innovations have been introduced. The increased interest towards the initiative resulted in the application of 9 companies with 14 interesting problems, hence four companies were selected for IPSP2016 instead of three. Moreover, particular attention has been paid to the promotion of the initiative in other universities: this effort has brought to IPSP2016 several participants not belonging to the University of Trento.

These proceedings are a detailed description of the activities carried out by the four teams taking part in IPSP2016. Each chapter contains a brief overview of the company and a description of the proposed problem, followed by the illustration of the different approaches that have been adopted in the search for the solution.

*Maddalena Bertolla, Claudio Castellan, David Roilo*

IPSP2016 Scientific Committee

CHAPTER

**ONE**

# REVERSE GRAVURE FOR ADHESIVE DEPOSITION

**M. Bertolla, A. Cernuto, C. Corrà, R. Isola, A. Lugnan, C. A. Maestri, M. Mancinelli, A. Mazzi, C. Piotto**

## 1.1 Introduction

### 1.1.1 The company

Arconvert S.p.A., founded in 1989 is located in Arco (Trento) and is part of the Fedrigoni Group.
It is devoted to the production of self-adhesive paper and films used to obtain labels of two different types: sheet and reel [1]. The first one is mainly used for bound inserts and stickers, while the latter is used in the Industrial-Chemical sector, e.g. for primary product labels and batch codes and in the food and beverage industry.
In particular, the activity of Arconvert consists in the deposition of a silicone layer on the liner (base material) followed by an adhesive layer. Finally, the resulting sheet and the face material are stuck together as shown in Fig. 1.1.

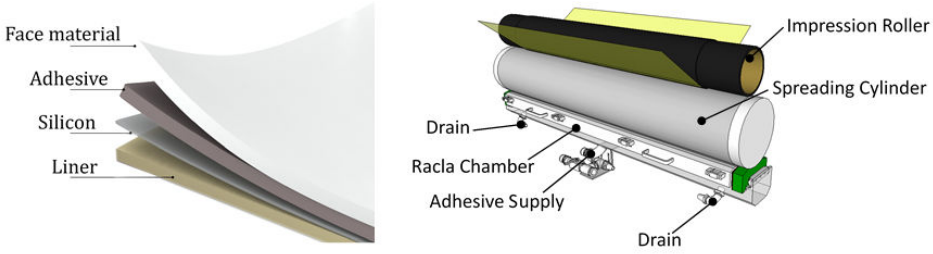


**Figure 1.1:** Different components of an adhesive sheet produced by Arconvert (left), scheme of the reverse gravure geometry (right).

### 1.1.2 The production process

The main components of the system are shown in Fig. 1.1 (right). The spreading cylinder resembles an endless screw with grooves of micrometer size. The cylinder lays over the racla chamber that contains the liquid adhesive. This cylinder rotates, collecting the adhesive and filling the small chambers of the screw. The adhesive is then deposited on the face material, on the top of the apparatus. The sheet is pressed against the face material by the impression roller (not shown in figure) and it moves with an opposite direction with respect to the cylinder.

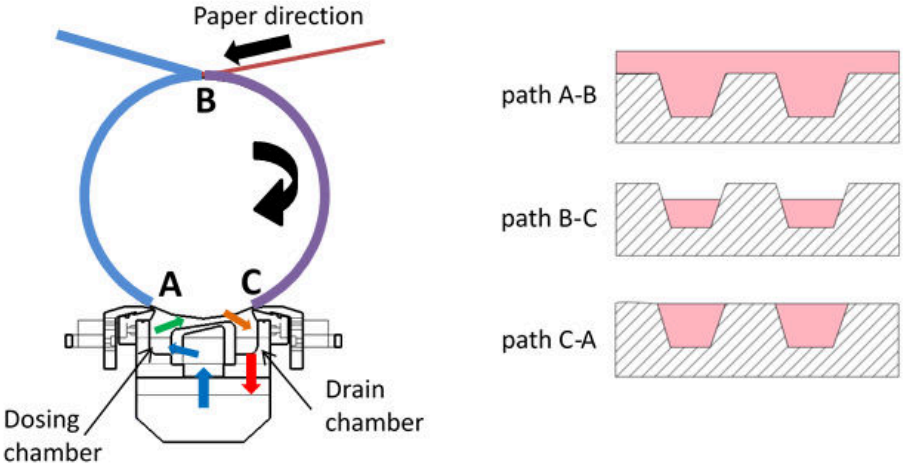


**Figure 1.2:** Illustration of different steps of the reverse gravure process. The filling level of the cylinder chambers in the different moments (right).

The main steps of the process (shown in Fig. 1.2 (left)) are the following:

- A: the cells of the cylinder are filled with the adhesive;
- B: the adhesive is deposited on the paper;
- C: the residual adhesive is removed from the cells and recycled.

The adhesive levels on the cylinder's surface are different in the three steps of the process, as shown in Fig. 1.2 (right). Between A and B the cells are overfilled by the liquid, while after the deposition (B-C path) the cells are partially emptied. Finally, in C-A the cells are *cleaned* and filled again.
The amount of adhesive deposited on the face material (also called *grammage*) can be varied regulating two parameters: the pressure of the adhesive into the dosing chamber and the velocity of the spreading cylinder.

### 1.1.3 The problem

The company needed to understand the origin of some problems that could occur during the spreading process. The first one is related to the deposition of low quantities of adhesive (below 13 g/m$^2$). Indeed, in this condition the deposition is not uniform: there are areas with no adhesive at all (fish eyes) or it can occur that the pattern of the cylinder is imprinted on the adhesive surface. In normal grammage condition, another observed problem is the response of different adhesives that shows the same defects mentioned above and different lower limits in grammage. Furthermore, the company observed a lower performance recycling the same adhesive for a long time.
The company asked us to investigate a way to deposit low quantities of adhesive, to understand the reasons underlying the presence of defects and finally to rationalize the reverse gravure process, in order to get a higher control on the different parameters.

### 1.1.4 The strategies

In order to approach the requests, three strategies have been adopted:

1. investigation of the upper and lower limits of the grammage;
2. individuation of the possible causes of the defects, such as the chemical-physical degradation of the adhesive and air bubbles;
3. implementation of a model for the system (Finite Element Method, FEM).

Arconvert provided us with samples of three different adhesives (here called A1, A2, A3) both new and recycled and allowed us to perform measurements in the company.

## 1.2 Parameters characterizing the adhesive

Three parameters are important to perform the physical characterization of the adhesive: density, viscosity and surface tension.

### 1.2.1 Density

The adhesive's density $\rho$ is measured in a simple way from the ratio of the mass of the samples and their volumes, according to the definition $\rho = m/V$, where $m$ is the adhesive's mass and $V$ its volume.
The average value of $1010 \pm 6$ g/dm$^3$ is obtained.

### 1.2.2 Viscosity

This fluid property measures the resistance to a gradual deformation by shear stress when adjacent layers move parallel to each other.
For this reason, a *cone and plate rheometer* has been used to analyze substances

at high viscosity. The torsion bar has conic shape and the fixed one is the plate: the angle between the surface of the two parts is around 4°.
The shear rate range explored is the typical range acting on the adhesive during normal operations at Arconvert (about 60 Hz, corresponding to 350 m/min, the cylinder velocity). Measurements at higher frequencies (up to 500 Hz) were performed to check its non-Newtonian behavior and to simulate a long time degradation to verify the presence of hysteresis.
The data points of viscosity vs. shear rate for the new adhesives were interpolated to have a continuous function to feed into the simulation (section 1.5).

### 1.2.3 Surface Tension

Surface tension is measured by taking advantage of the capillarity phenomenon, measuring the contact angle $\theta$ between the fluid and the glass capillary.
The surface tension $\gamma$ was measured using the relation [6]

$$\gamma = \frac{hgR\rho}{2cos(\theta)}, \tag{1.1}$$

where $h$ is the height reached by the adhesive in the capillary, $g$ is the gravitational acceleration, $R$ is the inner radius of the glass capillary, $\rho$ is the density and $\theta$ is the contact angle.

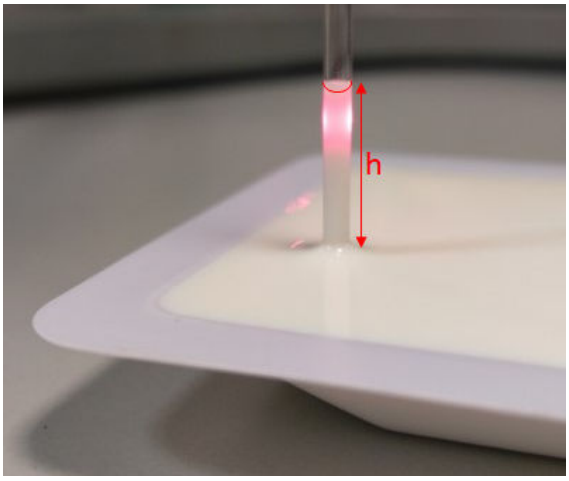


**Figure 1.3:** Apparatus for the measurement of the surface tension.

A laser is used to better identify the contact angle and the meniscus, as shown in Fig. 1.3. The resulting value is 0.03 N/m.

## 1.3 Grammage

The first task was to investigate the grammage in terms of its dependence on velocity and pressure and on the different types of adhesive.

### 1.3.1 Dependence on velocity and pressure

To evaluate the limits on grammage, we decided to monitor the process varying the pressure (80 mbar and 200 mbar over the atmospheric pressure) and the cylinder velocity (175 ÷ 230 m/min).
For each couple of pressure-velocity values, we measured different adhesive fluxes:

- the Output Flux ($F_{out}$) is the overall output adhesive flux. It is given by the sum of the weights of the adhesive from the drainpipe of Fig. 1.1 $F_{drain}$ and from the blades ($F_{blades}$), located in entrance and exit of the racla chamber;
- the amount of adhesive transferred to the silicone substrate ($F_{silicone}$), measured taking into account the silicone weight (estimated using the IR detector) and the cylinder velocity;
- the Input Flux ($F_{in}$), calculated adding $F_{out}$ and $F_{paper}$.

The relations between the grammage and the considered set-up parameters (output pressure and velocity) have been investigated with two different approaches, starting from the assumption that the more adhesive is collected by the cylinder, the higher is the grammage.
The first approach was a qualitative technique implying the use of a *laser beam* that hit the cylinder. The reflected light on a flat surface gave insights into the adhesive film uniformity. We used this procedure for different output pressures and velocities.

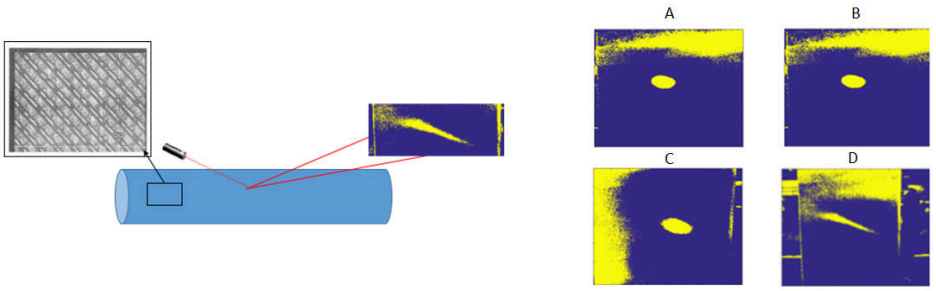


**Figure 1.4:** Scheme of the experimental setup (left). Diffraction pattern at different velocities (right).

Varying the velocity for a fixed pressure, the pattern created by the reflected light changed. In particular, for low velocities we observed a defined spot (Fig. 1.4 A, B, C), suggesting that the adhesive is spread in a smooth and uniform way. Instead, at higher velocities, the pattern becomes elongated and less defined (Fig. 1.4 D).
This phenomenon is due to an irregular adhesive coating on the cylinder. In this case, the adhesive does not entirely cover the cylinder and its texture scatters the light beam, giving the observed pattern (Fig. 1.4 left).
This qualitative approach showed that increasing the cylinder velocity, the adhesive distribution becomes less uniform.

This result was confirmed also considering a quantitative parameter correlated to the grammage, the *cylinder overfilling*. It was measured taking into account the cylinder height, the blades length, $F_{blades}$ and the cylinder velocity and hypothesizing that the blades remove just the overfilling and not the adhesive inside the channels.
Also in this case, we changed pressure and velocity as previously.

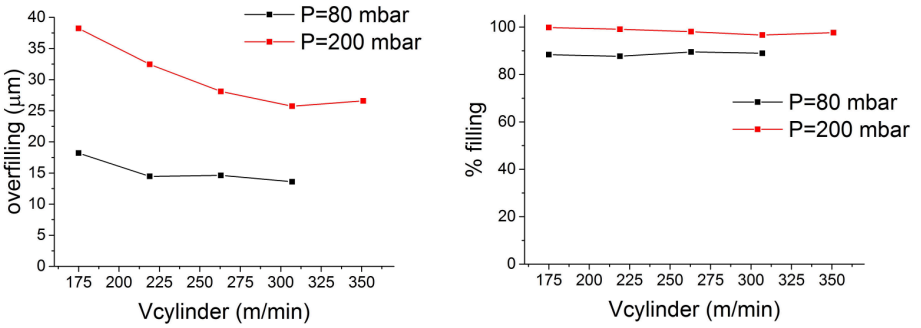


**Figure 1.5:** Overfilling of the cylinder (left) and percentace of filling of the cylinder cells (right) as a function of velocity.

As reported in Fig. 1.5 (left), we observed that at 80 mbar the overfilling is around 15 µm thick and it does not strongly depend on the cylinder velocity. Instead, at 200 mbar the data show an initial decrease in the overfilling with increasing cylinder velocity (as in the qualitative approach) followed by a plateau around 27 µm for velocities higher than 250 m/min.
We can conclude that the overfilling depends strongly on the output pressure; in particular, a lower overfilling is obtained with lower pressure. In addition, we found out that the lower limit in the grammage depends just on the pressure at high velocity.
Another investigated parameter is the *residual filling* of the cells between B and C points in Fig. 1.2. The residual filling percentage was estimated from the adhesive fluxes balance already described, knowing the cylinder rotation velocity and the resulting paper weight.
The dependence of the filling percentage on the cylinder velocity and pressure is reported in Fig. 1.5 (right).
It seems that the filling percentage is not related to the cylinder velocity. Regarding the pressure, it appears that the filling percentage is about 100% at 200 mbar and 90% at 80 mbar, but considering that these results are based on estimations, we cannot consider this difference significant.
All these considerations brought us to the conclusion that the filling percentage is neither related to the cylinder velocity nor to the input pressure.

### 1.3.2 Dependence on the adhesive type

The company observed that different adhesives give different performances. Only the acrylic nature of the adhesive is known, since it is supplied by an external

company. So we supposed that the observed behavior might be caused by differences in the molecular structure of the major components of the adhesive.
*FT-IR measurements* performed on the three samples of not used adhesive did not show differences in the functional groups (Fig. 1.6), meaning that the behavior observed does not depend on the molecular structure.

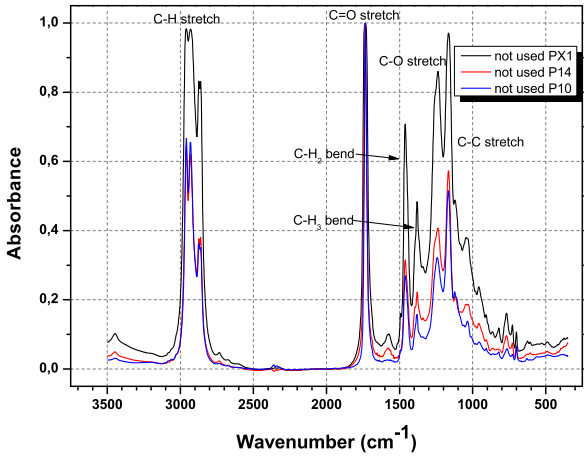


**Figure 1.6:** Comparison of FT-IR spectra of the different not-used adhesives, with the functional groups corresponding to each peak.

At this point, we looked for a different approach, that took into account the affinity of the adhesive for the substrate [7], considering the *contact angle* (Fig. 1.7) for the three adhesives on silicone and on the spreading cylinder.

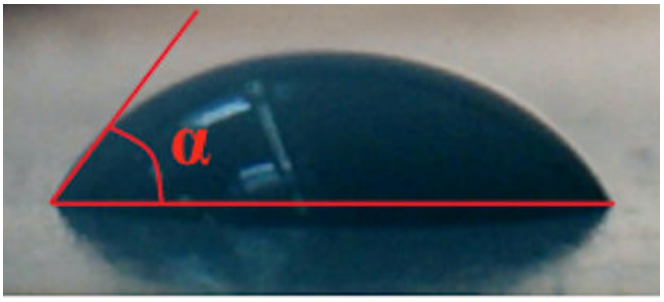


**Figure 1.7:** The contact angle $\alpha$.

We observed that the contact angle on the silicone substrate is the same for the three adhesives (Table 1.1), thus showing the same affinity for the silicone surface. Instead, the contact angle on the cylinder for the A3 adhesive is higher than those for A1 and A2.

| Sample | $\alpha_{silicone}$ | $\alpha_{cylinder}$ | $\alpha_{ratio}$ |
|---|---|---|---|
| A1 | $53° \pm 1°$ | $55° \pm 1°$ | $1.04 \pm 0.04$ |
| A2 | $53° \pm 1°$ | $51° \pm 1°$ | $0.96 \pm 0.04$ |
| A3 | $53° \pm 1°$ | $67° \pm 1°$ | $1.26 \pm 0.04$ |

**Table 1.1:** Values of contact angle for the three adhesives on silicone ($\alpha_{silicone}$) and on the surface of the cylinder ($\alpha_{cylinder}$) and ratio of the two values ($\alpha_{ratio} = \alpha_{silicone}/\alpha_{cylinder}$).

This suggests a lower affinity between A3 and the cylinder and a higher attitude to coat the silicone, with respect to the other two adhesives. According to our results, we expect a better performance of A3 adhesive in coating the silicone and this observation is confirmed by the company's know-how.
These results allowed us to suggest to evaluate not only the affinity between adhesive and silicone but also between adhesive and the cylinder substrate.
In general, we can define the absolute parameter $\alpha_{ratio}$ that is the ratio between $\alpha_{silicone}$ and $\alpha_{cylinder}$. The higher is $\alpha_{ratio}$, the wider is the grammage range of that adhesive, since the adhesive is more prone to leave the cylinder to cover the silicone.

## 1.4 Causes of defects

The company observed a loss of adhesive performances after a few hours of use. Chemical and physical degradations have been proposed as causes of this problem and specific measurements and analyses on the adhesive samples have been performed in order to verify these hypotheses.

### 1.4.1 Chemical degradation

*FT-IR spectroscopy* has been used to investigate the chemical decomposition of the polymeric chains. In fact, during the industrial process, the adhesive could be involved in undesired chemical reactions, breaking the molecules in smaller fragments or changing the functional groups. In this context, a useful result has been obtained analysing and comparing the spectra of the adhesives before and after the use. If the chemical structure underwent a change (e.g. transformation from an ester to a carboxylic acid), the spectra should show peaks at different wave numbers. Only the spectra of A3 adhesive are reported in Fig. 1.8, but similar results have been obtained for the other samples.
Both spectra are in agreement, without significant differences in absorbance peaks. We conclude that no chemical degradation is involved during the process.

### 1.4.2 Physical degradation

*Dynamic viscosity* of the adhesive suspensions has been studied to investigate a possible physical degradation. With the apparatus described in section 1.2.2,

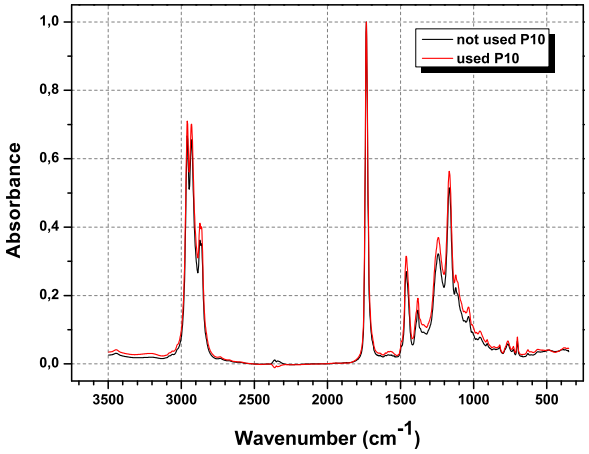


**Figure 1.8:** Comparison of not used (in black) and used (in red) A3 FT-IR spectra.

viscosity [Pa s] and shear stress [Pa] have been measured as a function of the shear rate [$s^{-1}$] and they are shown in Fig. 1.9. We can observe and conclude that:

- the viscosity decreases increasing the shear rate. Therefore, the adhesives behave as non-Newtonian fluids;
- viscosity and shear stress trends are similar increasing or decreasing the shear rate: no presence of hysteresis means that the adhesive is not subjected to physical degradation by shear stress;
- used and not used A1 and A2 samples have different viscosity;
- used A1 and A2 samples show scattered viscosity values at low shear rate, caused by the presence of lumps.

So, the significant results are just different viscosity values between the samples and the presence of impurities (lumps) in the used adhesives.
These two phenomena might be the consequence of the adhesive dehydration: water molecules are removed from the suspension promoting the polymer aggregation. Furthermore, the circulation of the adhesive in a recycling system increases the probability to have these impurities.
Lumps (and more generally defects) might be a real problem for a uniform adhesive distribution.
The company is aware of the problem and therefore it is used a filter to limit the impurities in the industrial apparatus; the filter is characterized by a mesh of 400 µm.
To check if the size of the filter mesh is suitable, the size of the lumps has been characterized.
For this aim, used adhesive samples have been placed on microscope slides and

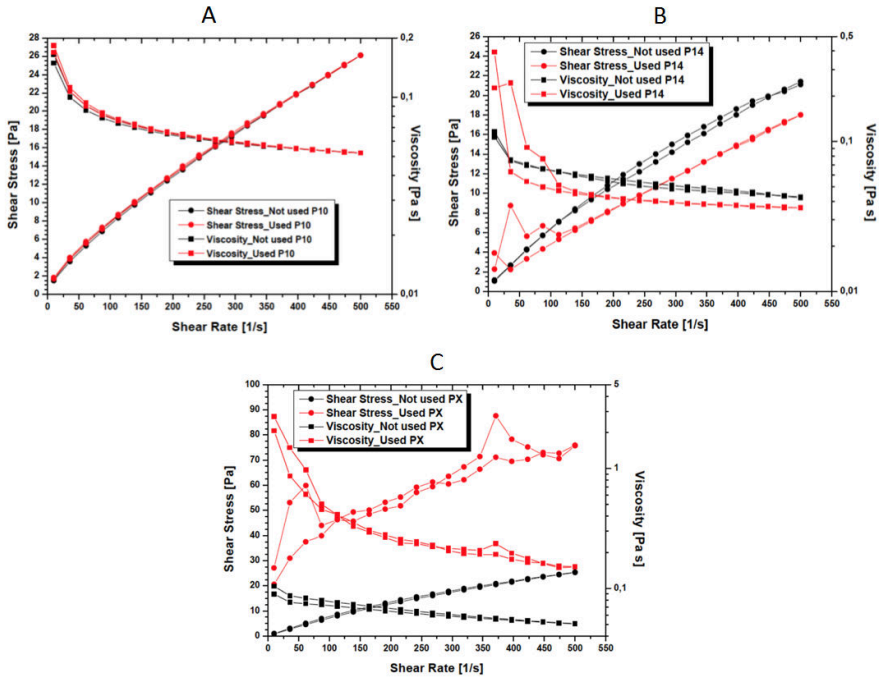


**Figure 1.9:** Comparison of not used (in black) and used (in red) viscosity measurements for A3 (left), A2 (center) and A1 (right).

after its drying, the images have been analyzed through the ImageJ software. The results show the presence of lumps with dimensions lower than 400 µm (Fig. 1.10): it means that these defects are not eliminated by the filters adopted by the company. From these considerations, we suggest the company to adopt finer filters in order to avoid the presence of lumps in the used adhesive.

### 1.4.3 Air bubbles

The presence of air bubbles is caused by the foam formation during the production process, and these bubbles might play a role in the not uniform adhesive deposition. The problem has already been faced by the company using a chemical compound that removes the foam. On the other hand, this treatment is strongly invasive and reduces the performance of the adhesive. Therefore, an alternative solution is needed.
Our primary goal was to understand if the air bubbles were produced directly in the racla chamber, on the cylinder due to the fluid dynamics of the adhesive or if they were already present in the incoming adhesive.
The fluid adhesive is supplied to the chamber from a collecting vessel equipped with three input pipes: one from the container of the fresh adhesive, one from the chamber drains and the last one from the blades that collect the adhesive

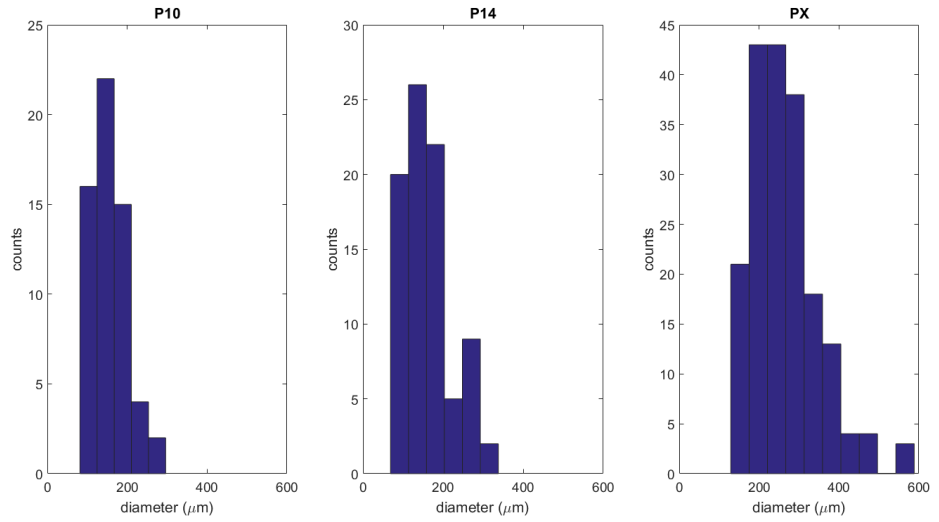


**Figure 1.10:** Size distribution of lumps for A3 (left), A2 (center) and A1 (right), considering an upper threshold of 600 $\mu m$.

excess. We decided to exclude the recycled adhesive (from the outlet and from the blades) so that the adhesive in the collecting vessel was only the fresh one.
The experiment was carried out in the facility using the A2 adhesive, that was provided to the vessel by a discontinuous-flow system, that allowed keeping the liquid level between a minimum and a maximum filling.
During the operations, we observed that a significant amount of foam appeared in the collecting vessel.
In order to obtain a qualitative characterization of the air bubbles absorbed by the adhesive, we studied their typical size and size distribution.
We collected a series of adhesive samples, taken from the collecting vessel, avoiding to pick up the macroscopic foam. Some adhesive drops were enclosed between two microscope slides. Once the adhesive was dried, we took some pictures of the samples then processed via the ImageJ software in order to compute the bubble size. This technique was sufficient to detect bubbles of size down to 50 µm.
A typical size distribution of the bubbles is shown in Fig. 1.11. The distribution is peaked around $100 \div 150$ µm. The air bubbles observed might be carried to the chamber. The main issue related to the gas bubbles entrapped in the adhesive regards the possible formation of defects in the adhesive layer deposited on the support, such as craters and fish eyes.
Even if the typical size of the gas bubbles that could be injected into the chamber is too small to cause significant defects, the hydrodynamic of the adhesive in the chamber might lead to bubbles agglomeration, with the formation of millimeter-sized bubbles.
The finite-element simulation (described in details in the next chapter) showed the presence of vortices in the racla chamber (see Fig. 1.12), causing the adhesive stagnation that increases the retention time of the liquid in the chamber. The

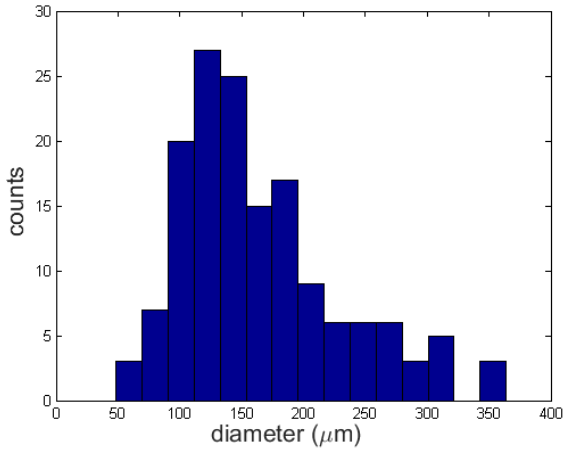


**Figure 1.11:** Experimental size distribution of the gas bubbles in the A2 adhesive.

whirling flow traps the small bubbles causing their aggregation.

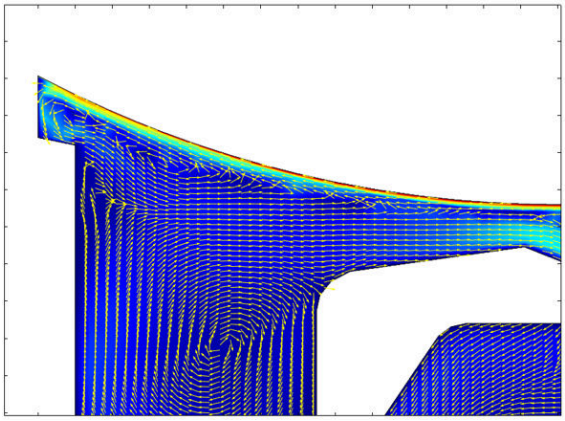

**Figure 1.12:** Finite elements simulation of the fluid dynamics in the chamber. The arrows indicate the velocity vector field, while the color map represents the velocity magnitude. Cylinder velocity 240 m/min.

We sketched out how the vapor bubble injection into the chamber could cause defects in the application of the liquid adhesive. Now we will discuss some hints to avoid this issue.
Of course, the Archimedes' principle suggests that the gas bubbles tend to come to the surface of the adhesive so that they should be spontaneously expelled in the collecting vessel. How long does this process take?
In a viscous fluid, buoyancy is opposed to the weight of the immersed object and the resulting force is contrasted by the viscous friction. The last term depends on

the motion regime and on the object's shape, but in the simple case of a spherical object moving in a laminar flow, it is expressed by the Stokes drag force [2].

$$F_D = 6\pi\mu a U, \tag{1.2}$$

where $a$ is the bubble radius, $U$ its velocity and $\mu$ is the dynamic viscosity of the fluid. Given the dependence of this expression on the velocity, we come to the classical result that a spherical object moving in a laminar, viscous flow has a limit velocity given by

$$U_{lim} = \frac{2}{9}\frac{a^2 g}{\mu}(\rho_f - \rho_g), \tag{1.3}$$

where $g$ is the gravitational acceleration, $\rho_f$ and $\rho_g$ are the fluid and gas densities, respectively.

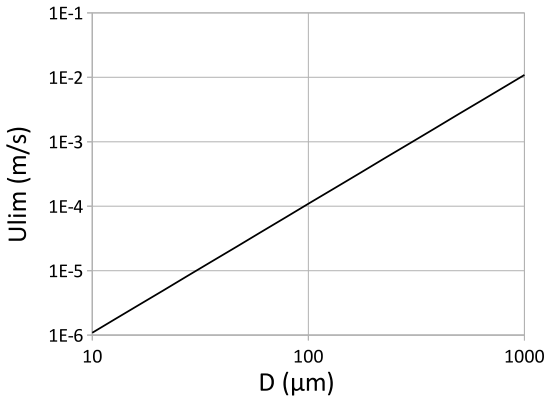


**Figure 1.13:** Limit velocity of gas bubbles in the adhesive as a function of the bubble size, calculated assuming $\rho_f = 1$ kg/m$^3$, $\mu = 0.1$ Pa s, which are consistent with an acrylic adhesive.

A plot of the limit velocity as a function of the bubble diameter is reported in Fig. 1.13. If we compare this result with the size distribution of Fig. 1.11, we obtain that the limit velocity is generally lower than 1 mm/s. This means that it would take tens of minutes to completely remove the gas bubbles from a container of tens centimeters height. If we consider that the capacity of the collecting vessel is of few tens of liters and that the flux provided to the chamber is about $10 \div 30$ liters per minute, the limit velocity found is too low to allow the elimination of all the bubbles.

Since we observed that the air bubbles are mainly formed due to the splashing of the fresh adhesive in the collecting vessel, this issue could be solved by modifying the adhesive supply system. In particular, the entrapment of gas bubbles occurs when the deforming inertial forces acting on the gas-liquid interface dominate the cohesive forces (i.e. surface tension). In the case of a liquid jet impinging on a liquid pool, this problem can be studied on the base of the two dimensionless

parameters $R_e$ and $W_e$, with

$$R_e = \frac{UD}{\mu} \qquad W_e = \frac{\rho_{liq} U^2 D}{\sigma}, \tag{1.4}$$

called Reynolds number and Weber number [3] respectively, where U is the jet velocity and D its lateral size. For a specific system geometry, it is possible to fix some threshold values for $R_e$ and $W_e$ above which the liquid entrains air. In general, at high Reynolds and Weber numbers, when the liquid surface is perturbed, the system is prone to air entrainment [4].
In order to avoid the formation of gas bubbles in the collecting vessel, it is necessary to reduce both the velocity and the size of the incoming jet. Of course, this should be done preserving the average flow of the adhesive.
Regarding the jet velocity, it is possible to reduce it choosing a more continuous pumping system. Since the demand of adhesive from the chamber is nearly constant, also the flux provided to the collecting vessel should be kept approximately constant, with a finer flow regulation.
On the other hand, it is possible to reduce the jet size, applying a properly designed flow laminarizer at the end of the input pipe. As an example, a honeycomb aluminum sheet some centimeters thick, with a cell size of few millimeters [5] could be used to laminarize the adhesive flow, thus reducing turbulence and foam formation.

## 1.5 Model of the system

To model the fluido-dynamics of the system, in particular the racla chamber, we used a Finite Element Method approach to solve the Navier-Stokes equations. From the extracted rheological parameters, it results that the fluid flow is laminar. Specific calculation has been performed for the A3 adhesive and the resulting Reynolds number is of about 200. From now on the rheological parameters chosen for the simulations are those extracted from the A3 adhesive.
Fig. 1.14 shows an example of the racla chamber divided in the mesh domain.
Since we found that the adhesive is non-Newtonian, the viscosity ($\mu$) varies with the shear stress, as reported in Fig. 1.15. The density is $1010\,\mathrm{kg/m^3}$.
The model takes into account the viscosity curve and at the end of the computation reports a 3D map of the actual viscosity. The velocity and viscosity maps are indeed linked.
The simulated system is schematized in Fig. 1.16. Since the system is symmetric, it has been simulated using a symmetry plane to reduce the computation weight (in a way to halve the mesh domains).
We started from a 2D CAD of the chamber section to reproduce the full 3D chamber. From now on, all the simulations will refer to the adhesive A3 considering three values of pressure (80, 140, 200 mbar) and cylinder speed of up to 250 m/min (4 m/s).
The fluid is injected inside the racla chamber from the adhesive supply channel (rectangular pipe of Fig. 1.16) and can exit from the Drain 1 channel, from the

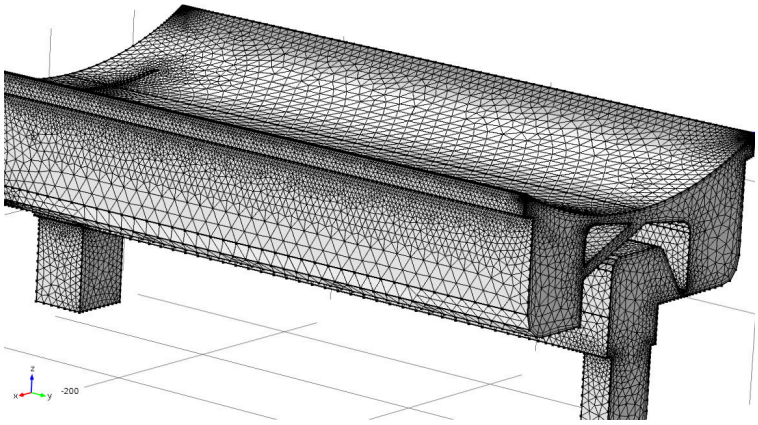

**Figure 1.14:** Racla chamber divided in the mesh domain.

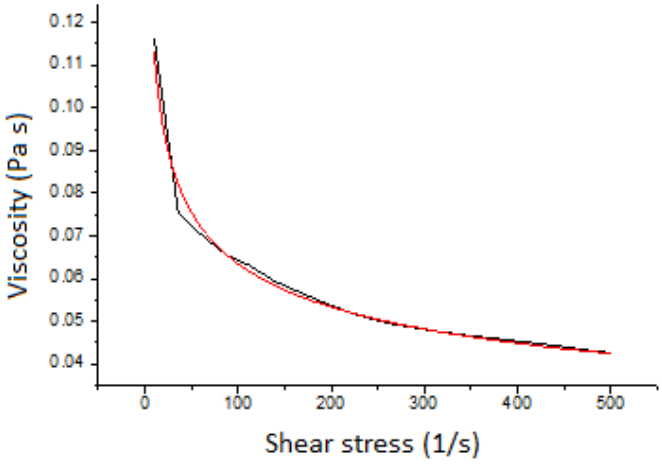


**Figure 1.15:** (Black) Dynamic viscosity as a function of the shear stress. (Red) Power law fit to be used with the model, the fitting curve was $\mu = m\gamma^{n-1}$ with m=0.2 kg/m s and n=-0.15.

Drain 2 channel (automatically considered by the symmetry) and from the cylinder out (the adhesive deposited on the paper). The cylinder out channel was approximated by a rectangle long as much as the whole chamber and 200 µm tall. The channel height was chosen to be half of the cylinder channel height in order to maintain the total exit area. The cylinder in is an "open boundary", with the same area of cylinder out, from which the fluid can enter depending on the fluido-dynamics of the chamber.

One of the most difficult computational problems was how to include the cylinder rotation into a model that does not contemplate a moving mesh, that would imply

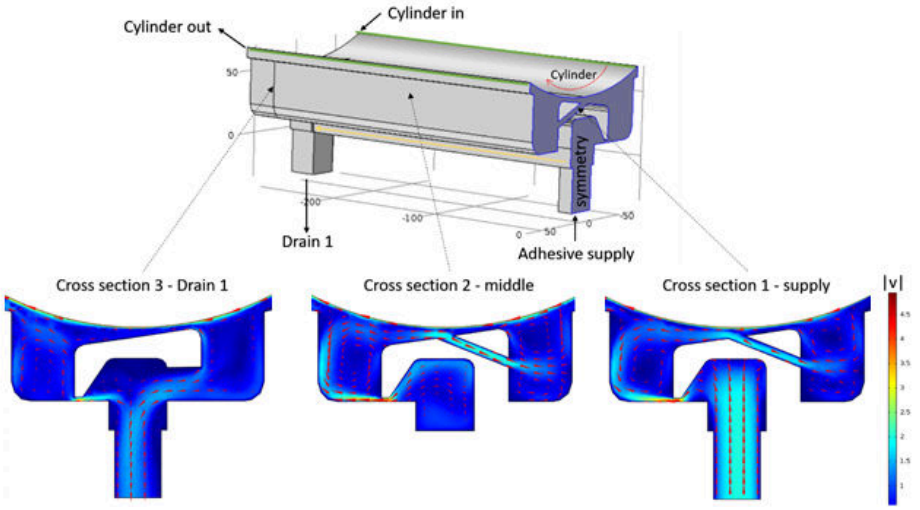


**Figure 1.16:** (Top) 3D CAD of the racla chamber. (Bottom) Cross-sections reporting the fluid velocity fields with cones to indicate the direction of the vector field. The velocity magnitude is reported in the colorbar in m/s. The length scale is in mm, the pressure 200 mbar and cylinder velocity 4 m/s.

a variation of the simulation domain during the computation. By including this kind of phenomenon, the simulation would last a week.
In order to overcome this problem, the cylinder rotation was included by imposing the "moving wall condition": this condition imposes that the cylindrical surface moves with a tangential speed equal to the tangential speed of the cylinder (m/min). In this way the fluid will be perturbed by the wall because of its local viscosity.
The fluid-dynamics of the chamber reported in Fig. 1.16 will be described using 3 cross-sections.

1. The supply pipe input surface is under pressure (fraction of bar). The fluid is injected from the supply pipe, enters in a pre-chamber that is linked to the racla through a small aperture (couple of mm). This helps to avoid the formation of vortices and to have and ordered stream at its output.
   Due to the Bernoulli's principle the fluid reaches the highest speed of 4 m/s at 200 mBar. The fluid is attracted by the low pressure on the right side and encounters the fluid that is moving on the opposite side (moved by the cylinder). The small channel on the right side of the chamber helps to let the fluid out and refill the right chamber. In this way the cylinder will grab new adhesive instead of recycling the one that comes back from *cylinder in*. Note that, close to the cylinder, there is always a small volume of fluid that moves similarly.

2. The fluid then travels following mainly the orange arrow (from right to left) reaching the cross section 2. The scenario here is similar to that of the section 1 and it is stable along the central part of the racla.

3. The fluid is forced to go into the right and left chamber to exit from the drain 1 that is imposed to be at 0 bar.

As reported in Section 1.4.3, the presence of vortices can increase the bubbles concentration. Fig. 1.17 reports a zoom of the section 2 (left) and (right) the average vorticity within the red rectangle as a function of cylinder velocity for three input pressures: 80, 140, 200 mbar. The vorticity tells how many revolutions the fluid is doing within a second.

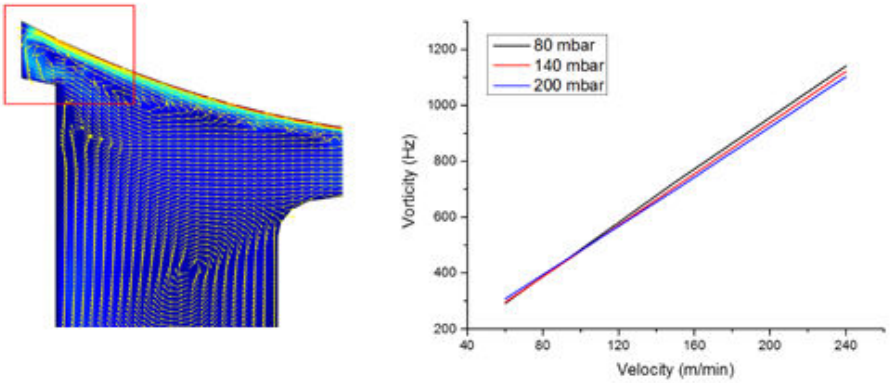


**Figure 1.17:** (Left) Zoom of the cross section 2. (Right) Average vorticity as a function of the cylinder velocity for several input pressure.

The simulations tell that the input pressure barely influences the vorticity that instead is linearly influenced by the cylinder rotation. This means that the cylinder speed and the bubble density are directly related.
To validate the fluid-dynamics model, we compared the mass flow rate from the cylinder in and out to those measured during the experiments at Arconvert. The reported mass flow rates are calculated by using the normal average speed at the out/in surface extracted from the model. The mass flow rate is defined as

$$\phi = v_{norm} A \rho \, [\mathrm{kg/min}] \,, \tag{1.5}$$

where $A$ is the output/input channel area, $v_{norm}$ the normal fluid speed and $\rho$ the density. The results are reported in Fig. 1.18. The mass flow rate is linearly influenced by the cylinder speed and increases with the pressure.
What is important to note is that for 3 data sets the model and the experiment are in agreement. This means that, despite the approximation used for the cylinder rotation, the physics within the model is well reproduced. On the other hand, the data sets identified by circles are not in agreement. The reason is probably linked to the fact that at high pressure the laminar flow approximation is not sufficient to find the proper solution. Another possibility is that the experimental data are affected by an error occurred during the measuring procedure, since we encountered a lot of problems related to the bubbles formation.
Fig. 1.19 reports the average fluid speed of the refill channel (within the red

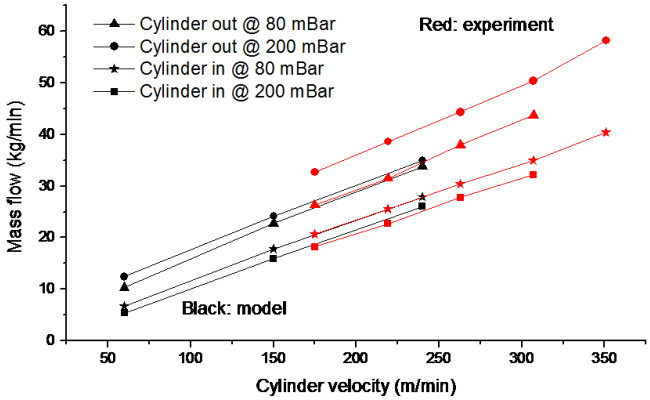


**Figure 1.18:** Simulated (black) and measured (red) mass flow rate as a function of the cylinder velocity for the cylinder out port (triangle, circles) and cylinder in port (star, square).

rectangle) as a function of the cylinder speed for two pressures. It is interesting to note that the refill channel helps to let the fluid flow from the left chamber to the right chamber especially at high rotation speed.
The channel presence is thus important at high paper volume production and avoids the stagnation of the adhesive into the left chamber.

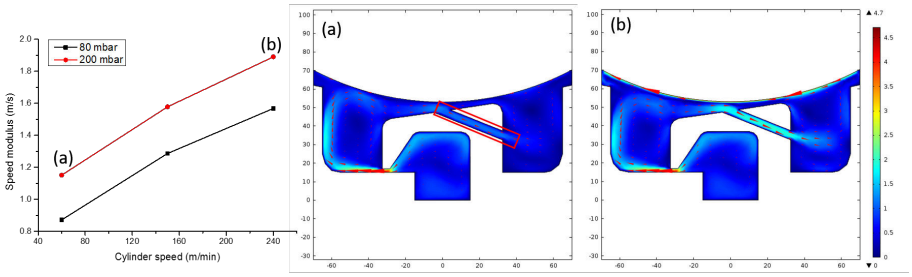


**Figure 1.19:** (left) Average fluid speed in the channel as a function of cylinder speed for two pressures: 200 mbar (red) and 80 mbar (black). Fluid speed map for a cylinder rotation and pressure of 60 m/min, 200 mbar (center ) and 240 m/min, 200 mbar (rigth). The red rectangle identifies the area over which the average has been computed.

This effect can be seen in the cross sections reported in Fig. 1.19 that are related to different cylinder speeds but same pressure. Also the pressure influences the flux within the refill channel but to a lesser extent compared to cylinder velocity, as reported in the graph of Fig. 1.19.
The last modelling attempt is related to the study of the adhesive-air interface by using a time domain FEM simulation. With this method it is possible to describe the time evolution of the adhesive-fluid interface when subjected to the centrifuge force and air drag. A sketch of the simulation is reported in Fig. 1.20.

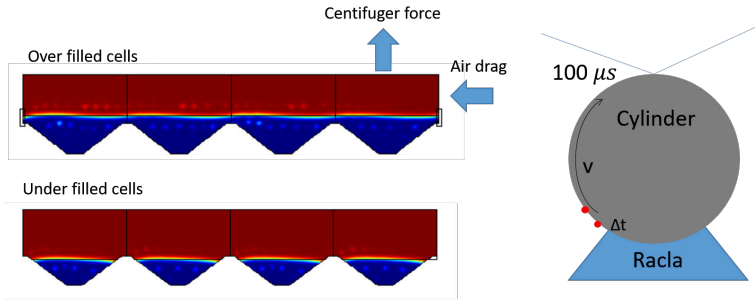


**Figure 1.20:** Adhesive-air interface shapes for two different initial conditions: over filled cell (top), under filled cell (bottom). (left) Sketch of the simulated system: the two red points identify the intial and the final simulation time. The used adhesive is the A2.

The adhesive-air interface is identified by the blue-red transition. The cylinder texture is represented by the trapezoidal geometry on the bottom of the simulation. The starting point is of course a flat interface and what is reported here is the interface shape after 10 µs of evolution for under filled cells (Fig. 1.20 bottom) and over filled cells (Fig. 1.20 top). The scope of the simulation is to investigate how the cylinder rotation affects the adhesive distribution.
The simulation predicts a modification of the fluid-air interface that is characterized by periodic modulations that are related to the cylinder texture. For overfilled cells this is even more important. Unfortunately, our computational power did not allow us to let the simulation evolve for all the racla-paper transit time of 100 µs.

## 1.6 Conclusions

Thanks to the investigations performed during the IPSP2016 week, several suggestions were proposed to the Arconvert Company.
We found that two parameters play a crucial role in the control of the grammage.

- Pressure is the limiting factor in the deposition of low quantities of adhesive;
- The absolute parameter $\alpha_{ratio}$ defined in section 1.3.2 predicts the performance of an adhesive.

In these terms, we suggest to Arconvert to neglect the velocity to reach low grammage, but to "play" only with pressure. Furthermore, we recommend evaluating not only the affinity for the silicone substrate, but also for the cylinder. In this way the company might know *a priori* the performance of the adhesive.

The physical and chemical analyses lead to the conclusion that the main causes of defects might be attributed only to the physical degradation. In fact, the recycling of the adhesive produces lumps that decrease the quality. For this reason,

we recommend using a filter with a finer mesh than 400 µm, substituting the normally used one, that is not proved to be efficient enough.

We identified the foam and the air bubbles in the adhesive as another source of defects. We demonstrated that the size of air bubbles is increased by the presence of vortices into the racla chamber. In order to avoid the formation of gas bubbles, we suggest to decrease the velocity of the incoming flux having a continuous pumping system and to reduce the jet size, applying a flow laminarizer at the end of the input pipe.

The fluido-dynamics of the racla chamber has been successfully described. Using a full 3D FEM method to solve the Navier-Stokes equation in laminar regime it was possible to predict and reproduce part of the experimental data.
The model revealed:

- the presence of vortices that can be related to the dimension and retention of the bubbles;
- the role of the refill channel, that links the left chamber to the right chamber and helps the refresh of the adhesive in the right part of the racla chamber. The importance of the role of the channel increases with the cylinder velocity.
- the air drag onto the adhesive surface can induce spatial modulations that are related to the cylinder texture.

This study demonstrates that the model is effective to simulate the fluido-dynamics of the racla chamber and can be used to engineer and optimize the system performances; the simulation was indeed in agreement with the experimental data.

The solutions proposed represent the basis for an improvement in the production process of the company and an interesting starting point for further investigations.

# Bibliography

[1] `http://www.arconvert.com`

[2] Choudhuri, A. R., *The physics of fluids and plasmas: an introduction for astrophysicists.* Cambridge University Press: 1998.

[3] Frohn, A.; Roth, N., *Dynamics of droplets.* Springer Science & Business Media: 2000.

[4] Zhu, Y.; Oguz, H. N.; Prosperetti, A, *On the mechanism of air entrainment by liquid jets at a free surface.* Journal of Fluid Mechanics: 2000, 404, 151-177.

[5] CEL Components S.r.l. `http://www.honeycombpanels.eu/20/aluminium-honeycomb`

[6] Sears, F. W.; Zemansky, M. W., *University physics.* Addison-Wesley: 1955.

[7] Oura, K.; Lifshits, V. G.; Saranin, A. A.; Zotov, A. V.; Katayama, M., *Surface Science: An Introduction.* Spinger-Verlag Berlin: 2001.

CHAPTER

# TWO

# IRON FOIL MAGNETIC PROPERTIES DEGRADATION

**M. Barbiero, E. Fava, G. Giacomozzi, A. Marchesini, C. Mordini, E. Mulas, M. Quaglia, A. Trenti**

## 2.1 Introduction

### 2.1.1 The company

Bonfiglioli S.p.A. has been working in the field of industrial power transmission since 1956. It is a multinational widespread in 80 different countries in the world. The research centre in Rovereto, BMR (Bonfiglioli Mechatronics Research) is dedicated to the design of mechatronic power transmission solutions integrating informatics, electronics, electrotechnics and mechanics. BMR works in the development of permanent magnet brushless motors and low backlash planetary gearboxes, aiming at combining high efficiency with complex functionalities.

### 2.1.2 The problem

Global warming is a serious issue for our society that needs to be overcome in this century. Legislation throughout the globe, points towards laws and standards that allow the reduction of emissions. Motors play a major role in this stage, as it has been estimated that, in the industrial sector, approximately 60 % of the total energy consumption can be ascribed to electric motors. At the time of IPSP2016, increasing efficiency is imposed worldwide by the International Electrotechnical Commission (IEC) through the International Standard IEC 60034 to companies. This standard defines efficiency classes for electric motors and requires manufacturers to reduce losses as much as possible. In the designing of a motor it is therefore important to possess a deep knowledge about the phenomena involved in the conversion of electrical energy in mechanical energy. In particular, to maximize an electric motor's efficiency, it is crucial to accurately know the losses (such

as hysteresis and eddy currents) occurring in the steel making up for the motor's magnetic circuit. One of the main sources of indetermination, hindering the exact modeling of the magnetic properties of the active parts of the motors, is the influence of the manufacturing processes on them.
The problem presented by Bonfiglioli for IPSP2016 consists in investigating the degradation of the magnetic properties of the M270-50A electrical steel foils (FeSi alloy, Si at 3.2 %), induced by the manufacturing cutting processes used to create the necessary geometries for the electric motor.
The two main cut processes are:

- laser cut (thermal);
- guillotine cut (mechanical).

Experimental measurements from literature show that the laser cut affects the magnetic properties more than the guillotine cut [2].
Currently the company uses the software *Flux* to simulate via a FEM (Finite Element Method) model the properties of the motor and predict the efficiency of the final prototype. Regarding the magnetic properties of the foils, the main two quantities assigned in the FEM model are magnetic permeability and power losses. The former is measured and tabulated from the manufacturing company before the cutting process occurs. The latter is found by fitting the *Bertotti model*, where the specific iron losses ($P_{\text{Bertotti}}$) are a summation of hysteresis, classical eddy-current and excess loss [1], to BH curves measured at 50 Hz:

$$P_{\text{Bertotti}} = k_{\text{hyst}} f B^{\alpha} + k_{\text{eddy}} f^2 B^2 + k_{\text{excess}} f^{1.5} B^{1.5}, \tag{2.1}$$

with $B$ the magnetic flux density and the coefficients $k_{hyst}$, $k_{eddy}$, $k_{excess}$ and $\alpha$ are determined from the measured data at a fixed frequency $f$ (50 Hz) by using an error minimization algorithm and are assumed for simplicity to be constant. Bonfiglioli experiences that the electric motor shows always a lower efficiency than the simulated one.
The aim for the IPSP group is to provide a theoretical model that fully accounts for the magnetic degradation of the laminations after the cut, in order to effectively simulate in the software the related correct magnetic permeability and power losses.
The company provided the Standard IEC 404-2 to perform Epstein frame measurements and different sets of M270-50A laminations to work with:

- length: 30mm;
- widths: 5mm, 10mm, 20mm, 40mm;
- height: 0.5mm.

### 2.1.3 The strategies

The main quantity for representing the magnetic properties of the motor is the magnetic permeability $\mu$, which is strictly related to the material response to

external magnetic influences. Two degradation models for the laminations are presented in Fig.2.1. The two models suit differently for experimental reasons. If it is possible to scan locally the magnetic properties, then the use of two magnetic permeabilities to describe the material is recommended. If instead these properties can be measured only globally, then the second one must be used.

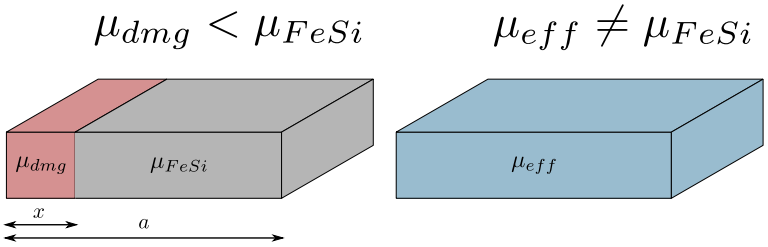


**Figure 2.1:** Two models representing degradation of magnetic properties through the magnetic permeability.

In order to approach the problem, three strategies have been adopted:

1. SEM (Scanning Electron Microscopy) analysis in order to visualize differences between the two cutting techniques;

2. magnetic measurements in order to characterize the foils, in particular hysteresis curves, power losses and frequency studies were performed;

3. simulations in order to evaluate the area damaged by cutting.

## 2.2 Scanning Electron Microscopy analysis

Here we report on the analysis done using the Scanning Electron Microscope (SEM), which is a special microscope used to image the surface morphology. More in detail, we present at first the images related to the laser cut foils, and we show then the images obtained for the foils cut with the guillotine technique.
The SEM is a microscope which uses an electron beam to image the sample's surface [3]. The electrons interact with the atoms of the specimen resulting in different types of signals, ranging from secondary electrons to back-scattered electrons or photons at different energies. From these signals, it is possible to obtain a wide range of information on the specimen. In particular, it is possible to image the sample surface with a resolution higher than 1 nm, as well as to obtain information on the distribution of the chemical elements constituting the sample. By detecting the spin polarization of the emitted secondary electrons, it is also possible to determine the magnetic properties of the specimen.

### 2.2.1 Results and discussion

The SEM analysis has been performed on the laser cut samples as well as on the guillotine cut ones. Samples 40 and 5 mm wide have been analyzed in both the

cases. In the following, we report the images collected at different positions along the cut profile. Fig. 2.2 is a guideline to illustrate how the SEM analysis has been performed.

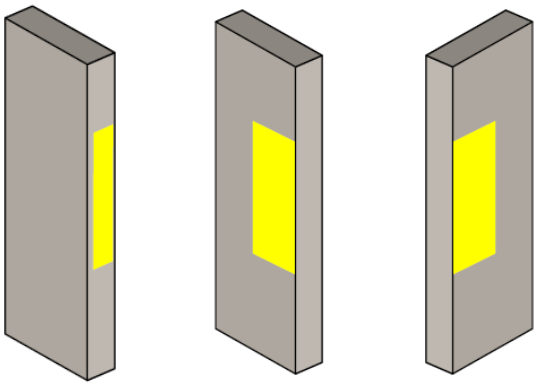

**(a)** Frontal **(b)** Side 1 **(c)** Side 2

**Figure 2.2:** Sketch of the different orientations at which SEM images have been taken.

The first images we present are related to the analysis of the laser cut foils. Fig. 2.3 represents the frontal view of the incision. In both the figures, a thin layer with a different morphology is clearly visible at the edges of the specimens. This thin layer corresponds to a FeSi coating which has been melted before solidifying again. The melting process is due to the laser passage, since it can determine temperatures of the order of the iron melting temperature. Fig. 2.4 shows a detail of the melt region close to the cut edge for the case of a 40 mm wide specimen. A similar morphology has been detected on the other side (side 2) of

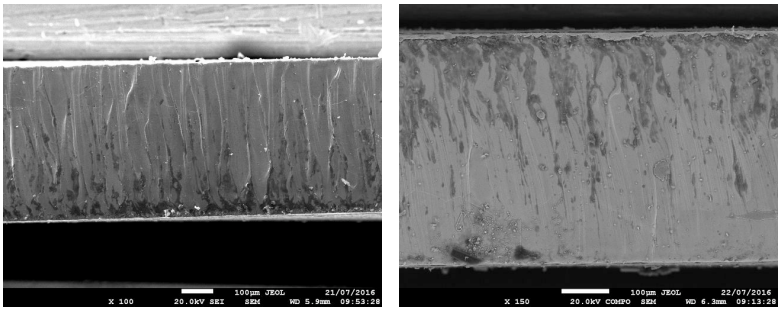

**(a)** LS 40 mm **(b)** LS 5 mm

**Figure 2.3:** Frontal SEM images of two different type of laser cut samples (LS).

the specimens, consequently we avoid to report the images of side 2.
From now on, we report on the analysis done of the foils cut using the guillotine

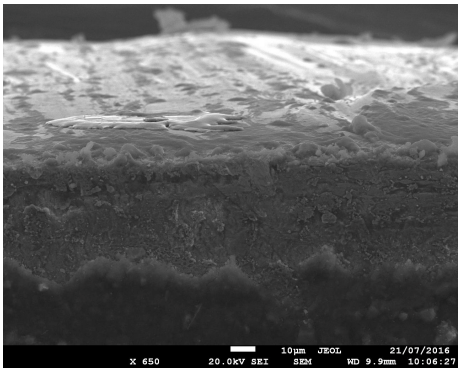


**Figure 2.4:** Detail of the melt region along the side 1 of the laser cut sample with a width of 40 mm.

technique. Fig. 2.5 shows a frontal view of the cutting profile. We can observe a region where the FeSi has been mechanically deformed. More in detail, it is possible to see a curvature in the upper part of the frontal view of the cutting. This effect can be explained considering that the guillotine effect is an initial bent of the material and a consecutive cut along the thickness of the foil. This hypothesis seems to be confirmed by the observation of insulating glue traces along the cutting profile, which correspond to the dark spots visible mainly in the sample of 5 mm. In fact, the guillotine blade drag the glue from the surface along the cutting. Figure 2.6 represents the upward view of the cut edge. Here

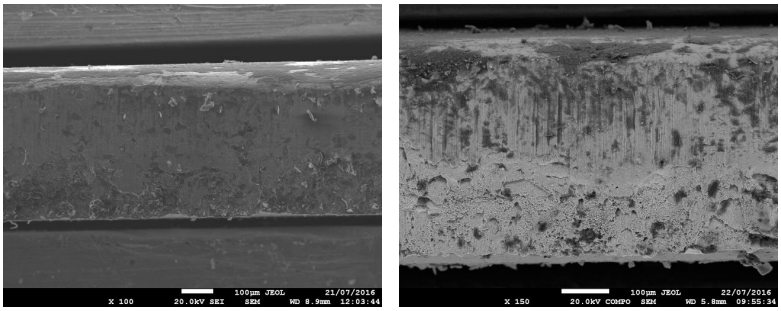


**(a)** CS 40 mm **(b)** CS 5 mm

**Figure 2.5:** Frontal SEM images of two different type of guillotine cut samples (CS).

the cutting edge has been clearly deformed by the pressure of the blade. This deformation region presents a width of about 40-50 µm.
Concluding, thanks to the SEM analysis, we underlined some differences between the two cutting techniques. In particular, in the case of laser cutting, we observed a small region of melted material (about few µm). A larger region where the insulating glue has been removed is also evident. From this analysis we can deduce that at least the melted area has lost its magnetic properties. In fact both

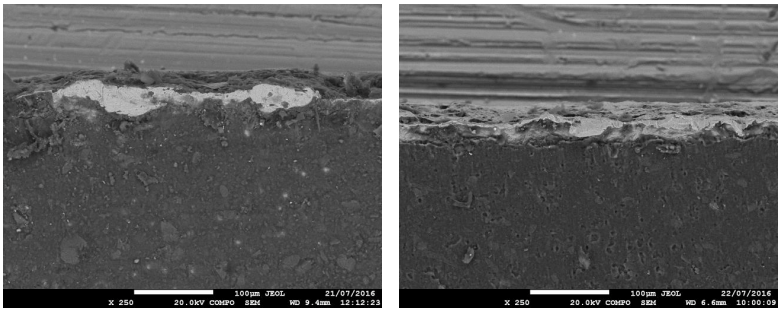


**(a)** CS 40 mm **(b)** CS 5 mm

**Figure 2.6:** Side 1 SEM images of two different type of guillotine cut samples (CS).

the high temperature and the loss of structural order of the material contribute to determine the magnetic response to external fields [4].
For what concerns the specimen cut using guillotine technique, we observed a structural bent 50 µm wide. In this case, it is not easy to correlate the mechanical stress with a degradation of the magnetic properties. However, from the data obtained we can deduce that, due to the cutting bent, the crystalline order of the atoms has been modified leading to a change in the magnetic properties of the sample. From the analysis of the SEM images, such mechanical deformation is less drastic than in the laser cut case.

## 2.3 Magnetic measurements

During the IPSP2016 week event we performed the following experimental magnetic measurements on the iron foils:

1. hysteresis curve;
2. power losses;
3. frequency study.

A detailed description on the methodology used and the results obtained is outlined in the next sections.

### 2.3.1 Hysteresis curve

The hysteresis curve (or B-H curve) describes both the non-linear response of the material to externally applied fields, and the fact that this response "has a memory" and depends on the history of the applied fields. Hysteresis is an intrinsic source of energy loss and it must be taken into special account in applications that require time-varying fields, such as those which run an electric motor. In a FEM simulation aiming to predict the efficiency of a motor, parameters such as the hysteresis curve are inserted into the software by the user, and are usually read

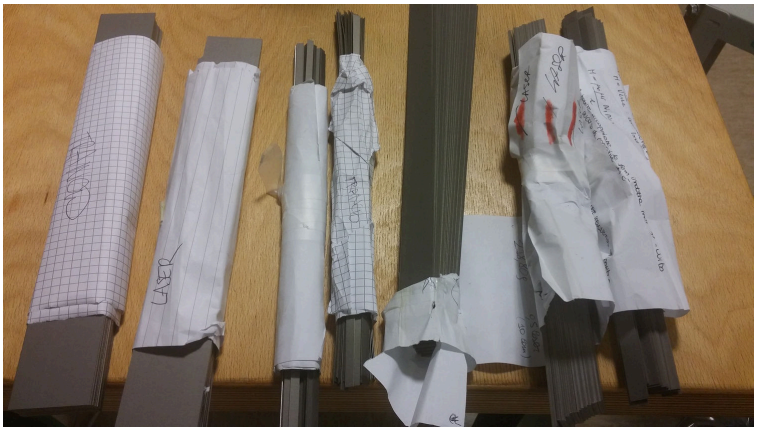

**Figure 2.7:** The laminated iron samples

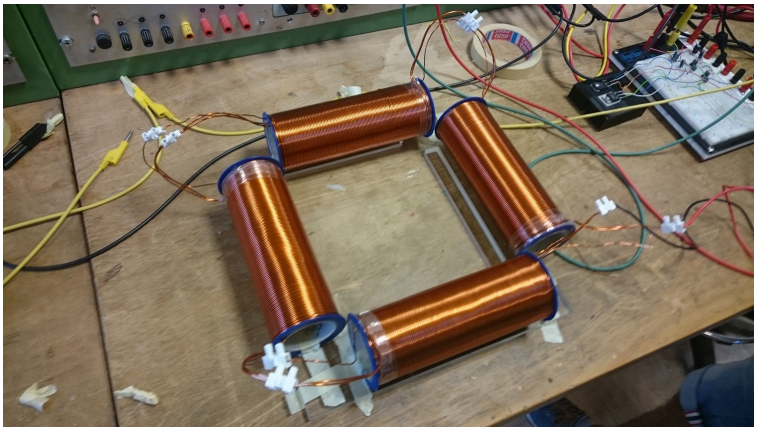

**Figure 2.8:** The Epstein frame

from standard tables or provided by the supplier who ships the laminated iron. However, it is known that those values do not take into account the influence of the manufacturing process, in particular the cutting. For this reason we wanted to repeat the measurements on the set of iron samples provided by the company, cut in different sizes and with different methods, to seek for some quantitative effects. According to the IEC 404-2 regulation, we built an Epstein frame, which is the instrument recommended by the International Electrotechnical Commission for measuring the magnetic properties of laminated iron samples. It constitutes an unloaded transformer in which the coupling between the primary and secondary windings is provided by the test specimen. The foils we tested are shown in Fig. 2.7, while the realized Epstein is photographed in Fig. 2.8.
Fig. 2.9 shows a schematic circuit of the apparatus. By applying a sinusoidal input voltage and measuring the voltage drop $V_R$ across a known resistor of resistance $R$, we can measure the current $I(t)$ in the primary coils, which is related to the

magnetic field inside the sample $H(t)$ by:

$$H(t) = \frac{N_1}{l} I(t) = \frac{N_1}{l} \frac{V_R(t)}{R}, \tag{2.2}$$

being $N_1$ the number of windings in the primary, $l$ the total length of the coils and $t$ the time. On the other hand, the open circuit voltage difference $V_{out}(t)$ measured on the secondary coils gives us the magnetic induction $B$ inside the iron sample by means of Faraday's law:

$$V_{out}(t) = -\frac{d}{dt}\phi(B) = -N_2 \frac{d}{dt} \left[ S_m \, B(t) + S_{air} \, \mu_0 H(t) \right], \tag{2.3}$$

with $\phi(B)$ the magnetic flux, $N_2$ the number of windings in the secondary (in our case $N_1 = N_2$) and $\mu_0$ the vacuum permittivity, while $S_m$ and $S_{air}$ are (respectively) the cross-section of the iron core and of the surrounding air.

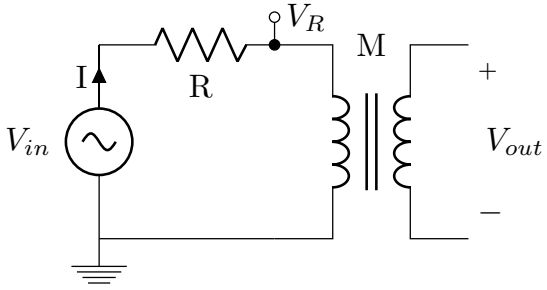


**Figure 2.9:** Schematic of the measuring circuit.

By simultaneously recording the time signals $V_R$ and $V_{out}$ with a two-channel oscilloscope we evaluated the field intensities $H(t)$ and $B(t)$, plotting then the B-H curve.
We repeated the measurement described above by loading the frame with a given number of iron strips (11 per side) but varying from time to time their width and typology (laser / mechanical cut). We used as an input source a variable AC transformer (a Variac), to be able to drive the circuit with high currents and reach high enough fields. The disadvantage of this was that we could only work at an AC frequency of 50 Hz, which prevented us to study the high-field response of the material also as a function of the frequency.
The curves that we obtained are shown in Fig. 2.10. We see that they vary significantly with the width of the iron samples. For limitations in our instrumentation we could only measure $V_{out}$ up to a maximum peak-to-peak value, which means a maximum amount of magnetic flux: for this reason in the 40 mm width samples, which have the greatest cross section, we could not reach a flux density high enough to see saturation.
We indeed reached saturation in the 20 mm wide samples, thus exploring the whole hysteresis curve. We see a striking difference between the samples cut with the two methods, confirming the expected qualitative behavior: the laser cut sample

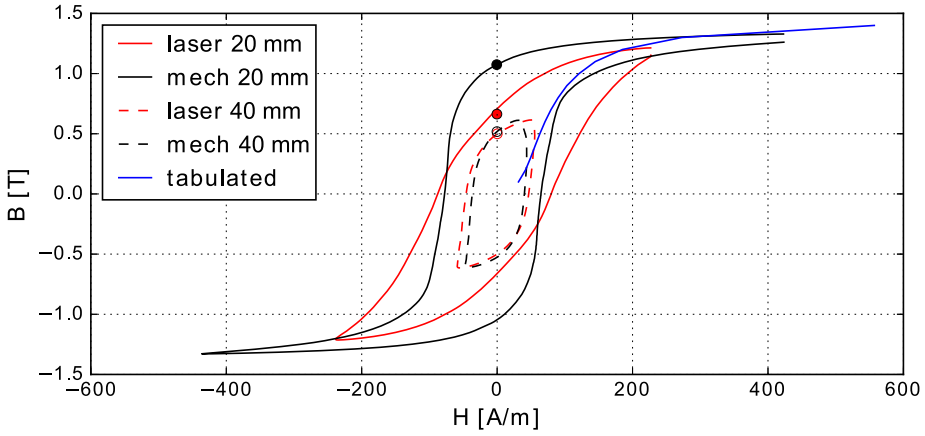


**Figure 2.10:** Hysteresis curves obtained from different samples. The blue curve corresponds to the virgin B-H curve (taken from [6]).

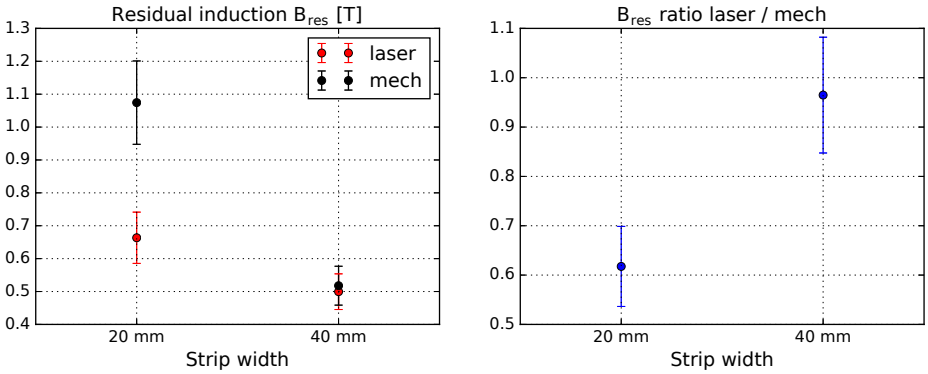


**Figure 2.11:** Comparison of the residual induction as a function of the sample width.

shows a reduced response (that is, a smaller magnetization at the same external field) with respect to the mechanical cut one. The same behavior can be seen in the 40 mm sample curves, even though it is much less appreciable.
A quantitative comparison can be made here by evaluating the residual induction $B_{res}$ for the two cut processes. $B_{res}$ is the value of the magnetic induction $B$ which remains at zero external field. This is a measure of the amount of magnetizable volume in the sample, and it is expected to be sensitive to the damage and degradation effects of the manufacturing [5]. Along the measured curves, we added for comparison a *virgin*[1] magnetization curve for the same material that we took from tabulated values available online [6]. The markers on the y axis sign the values of the residual induction.

[1] That is, from a sample which has not been magnetized earlier, starting then at zero induction for zero magnetic field.

| Foil width (mm) | Laser cut power losses (W $Kg^{-1}$) | Guillotine power losses (W $Kg^{-1}$) | Variation |
|---|---|---|---|
| 5 | 4.65 | 4.69 | -1% |
| 10 | 3.68 | 3.48 | 6% |
| 20 | 1.40 | 1.48 | -6% |
| 40 | 0.39 | 0.33 | 19% |

**Table 2.1:** Measured power loss per unit mass for different width foils obtained using laser cut and guillotine cut. The relative variation is shown in the last column.

Fig. 2.11 shows instead the extracted residual induction individually, and the ratio $B_{res}^{\text{laser}}/B_{res}^{\text{mech}}$ as a function of the strip width. From these measurements we still were not able to quantify the depth of the damaged area, but we could give a comparison of the damage entity between the two different cutting methods. We saw that the damage effect vanishes as the sample size increases, confirming that the damage is an effect localized at a finite depth from the border which has been subjected to the cut.
Probably the most important upgrade would then be to use a high current source with variable frequency as the input drive. In this way one could try to include the effect of other causes of low efficiency, such as iron core losses, which trigger at frequencies higher than the one we explored, but that are well in the range of normal working conditions for this kind of electric motors.

### 2.3.2 Power losses

Alongside the estimation of the hysteresis behavior of the iron samples, we performed directly a measurement of their core losses by finding the dissipated power per unit mass (a quantity which is measured in [W $kg^{-1}$]). In order to execute this task, we used the Epstein frame described in the previous section. The power losses set-up is shown in Fig. 2.12. The primary coils are connected to a variable voltage AC power supply consisting in an autotransformer feeding a 230 V to 24 V step-down transformer (the latter transformer allows us to work with currents that would cause the autotransformer to work above its VA rating). The nominal AC frequency is 50 Hz. The secondary coils of the frame are in open circuit conditions (the same configuration used in the hysteresis measurements). Both input current and input voltage are simultaneously acquired with an oscilloscope with a sampling rate much higher than the nominal AC grid frequency. This allows us to measure the real absorbed power without worrying about the power factor $\phi$ [7]. By measuring the mass of the iron sample, we are then able to calculate the specific power losses, i.e. the dissipated heat per unit mass. All the measurements are performed at a constant input RMS voltage of 20 V. An exception is made for the 0.5 mm wide samples (both laser and mechanical cut ones) whose lower mass caused the power supply to cut out at a lower voltage. The measurements for these smaller samples are made at an input RMS voltage of 15 V. The results are presented in Tab. 2.1. Unfortunately this measurement does not allow us to

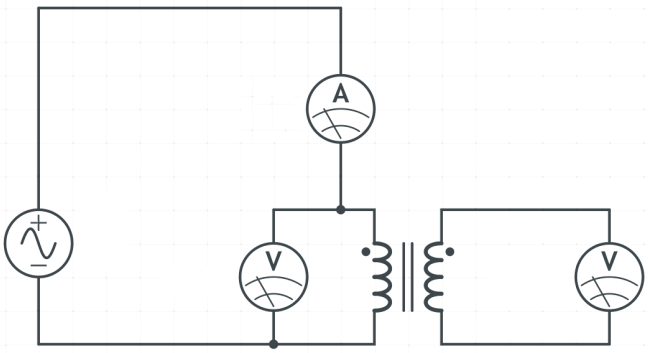


**Figure 2.12:** Power losses measurement setup.

associate the higher power loss per unit mass to one of the cut methods. Consistent results may be achieved in future by performing measurements with the same overall steel mass instead of the same number of samples with different sizes and normalizing for the mass *a-posteriori*.
Finally, it is worth noting that this kind of measurement is not able to distinguish the source of power loss (hysteresis, parasitic currents or other sources), but it is able to give an effective losses result, which is easy to implement in any finite element simulation.

### 2.3.3 Frequency study

In this section, the frequency study is presented. The goal is to perform a quantitative comparison between the mechanical cut and the laser-cut method. Once that the samples are loaded in the Epstein frame, the magnetic circuit is excited with an external AC signal and the the output signal is collected. It is useful to study the transfer function of the system, which is defined as the ratio between the output and the input signal, and is related to the proprieties of the system. While fixing the input voltage amplitude and by sweeping its frequency in the primary coils, the output voltage amplitude is recorded on the secondary coils. The transfer function of the system is computed according to the following formula:

$$|G(f)| = \left| \frac{V_{\text{out}}(f)}{V_{\text{in}}(f)}, \right| \tag{2.4}$$

where $V_{\text{in}}(f)$ is the input voltage at frequency $f$, $V_{\text{out}}(f)$ is the output voltage and $G(f)$ is the transfer function. In the following, we discuss only the absolute value $G(f)$.
Our idea is to model the transfer function behavior as a function of electrical macroscopic elements, such as the resistance of the coils and their inductance. In this way, we want to simulate the measured $G(f)$, as the transfer function of

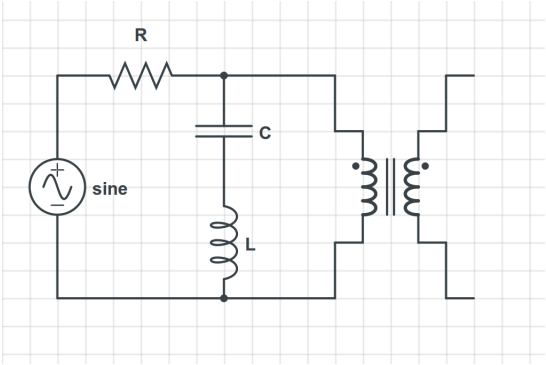


**Figure 2.13:** Circuit model of frequency analysis. The primary coils are fed by a sinusoidal voltage signal $V_{\text{in}}(f)$. The $V_{\text{out}}$ signal is measured on the secondary coils.

an electric circuit. This approach tries to be as general as possible and it can be further improved by considering secondary effects (parasitic effects and losses can be taken into account improving the circuit or adding some extra electrical components). Fig. 2.13 reports the model of the electrical circuit that we used. The primary coils resistance is $R = 100\ \Omega$. $L_M$ is the inductance given by the material inside the Epstein frame. The final goal of this approach is to derive a value of $L_M$ and model it as a function of the cut-degraded material width. In this way we identify $L_M$ as:

$$L_M = \mu_0 N^2 S_{\text{air}}/l + \mu_0 \mu_r N^2 S_{\text{m}}/l, \tag{2.5}$$

where $N$ is the number of the loops, $l$ is the length of the coil and $\mu_r$ is the permittivity of the iron sample, while $S_{air}$ and $S_m$ are (respectively) the surface of the air and the iron sample. The inductance $L$ and the capacitance $C$ reported in Fig. 2.13 characterize a possible frequency response of our Epstein frame without loaded material. We call it vacuum response. One can distinguish between two possible behaviors of the electrical circuit:

- neglecting the presence of the material inside the Epstein frame, the vacuum response describes the frequency bandwidth of our system, as an $RLC$-circuit;
- the presence of the material inside the Epstein frame can modify the low frequency regime, as an $RL$-circuit.

In this study, the input signal is generated by a waveform generator (Agilent 33120A). The peak-to-peak amplitude is fixed to 10 V. The frequency is swept in the range from 50 Hz to 100 kHz. The output signal is sampled by a digital oscilloscope (Agilent DSO-X-2002A). The frequency response of the system is shown in Fig. 2.14. In the plot, two regions can be distinguished.

- **High frequency region**. In this region all the samples show the same behavior. A peak in the transfer function is observed at 100 KHz. The fact

that different samples exhibit the same response, can be explained by geometrical proprieties of Epstein frame **or by the of parasitic capacities existing between single loops or between the primary and secondary coils**. This region can not help to make a quantitative comparison between different cut processes of iron sheets.

- **Low frequency region**. In this region the system tends to respond differently as a function of the iron samples. Following our model exposed in Fig. 2.13, the transfer function $G(f)$ for low frequencies can be described as:

$$G(f) = \frac{ifM}{ifL_M + R} \qquad \Rightarrow \qquad |G(f)| = \frac{f/f_0}{\sqrt{1+(f/f_0)^2}}, \tag{2.6}$$

where $M$ is the mutual-inductance of the coils generated from the secondary coils to the primary one and $f_0 = R/L_M$ is the frequency response of the sample. Eq. (2.6) can be simplified by considering the primary coils equal to the secondary coils and assuming a perfect coupling between them. In this case $M = L_M$. According to our model, increasing the width of the samples inside the Epstein frame (and consequently $S_\mathrm{m}$), the value $L_M$ will increase following Eq. (2.5) and consequently $f_0$ will reduce. Such behavior is well observed in Fig. 2.14.

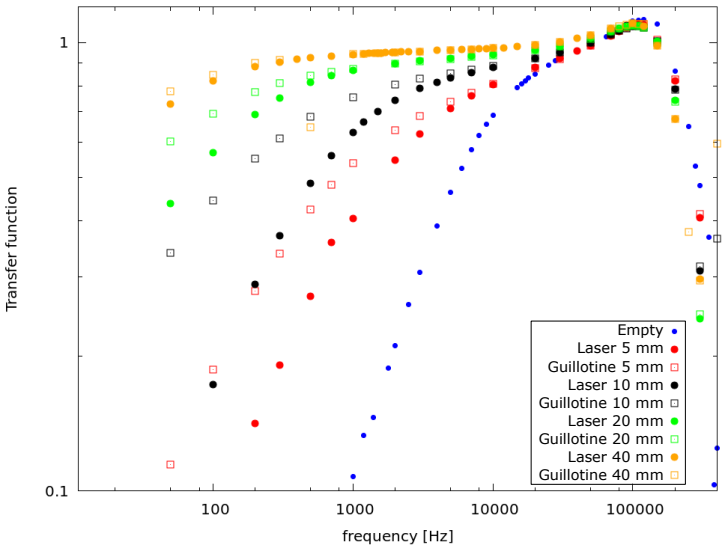


**Figure 2.14:** Transfer function for different samples. The laser-cut samples are shown with full circle points, the mechanical-cut ones with squared empty points. The blue points represent the response of the system without the iron sample, which we called vacuum response. The red, black, green, orange points represent the frequency response which correspond to different sample widths.

The value of $f_0$ is determined by means of a fit procedure and consequently $\mu_r$ is derived from Eq. (2.5) and Eq. (2.6).

From Fig. 2.14, it can be observed that (for fixed sample width) the two cutting methods behave differently in the low-frequency region of the plot: at the same frequency, the response of the mechanical-cut sample is higher than the corresponding one for the laser cut. The effect is well observed at small sample width. If we want to make a more quantitative comparison of how much the cut procedure modifies the magnetic proprieties of the material, the relative percentage variation $\Delta^c_{\%}$ of the inductance with respect to its vacuum value can be computed. Such percentage can be estimated as:

$$\Delta^c_{\%} = \frac{L^c_M - L_0}{L_0} = \frac{S_m(\mu^c_r - 1)}{S_m + S_{air}}, \tag{2.7}$$

where $c$ indicates the cut procedure ($l$ for laser cut, $s$ for mechanical cut) and $L_0 = \mu_0 N^2 (S_{\text{air}} + S_m)/l$ is the inductance of the Epstein frame without iron sample inserted. In details, the value $L_M$ can be extracted by fitting Eq. (2.6) with the data presented in Fig. 2.14. Once that $L_M$ is computed, $\Delta^c_{\%}$ can be estimated according to Eq. (2.7). Finally, as a figure of merit, it is interesting to compute the ratio between $\Delta^l_{\%}$ and $\Delta^s_{\%}$. This quantity is directly dependent on the magnetic properties of the material:

$$\frac{\Delta^l_{\%}}{\Delta^s_{\%}} = \frac{\mu^l_r - 1}{\mu^s_r - 1}. \tag{2.8}$$

We estimated the ratio defined in Eq. (2.8) for different sample widths. The results are reported in Fig. 2.15. For small sample widths, the difference in the magnetic proprieties is clear. By increasing the sample width, the relative contribution between the cutting processes tends to be smaller and smaller. This is a reasonable result, as both the cutting procedures create only a local edge defect on the material. When the size of the material is increased, the relative contribution of the local edge magnetic degradation becomes less evident.
This fact is in agreement with the conclusions led from the hysteresis analysis, where the difference in the two kinds of samples vanishes as the sample size is increased.

## 2.4 Simulation

As we have seen, laser cut samples exhibit worst magnetic properties than mechanical cut ones. It is reasonable to assume that this discrepancy is due to the different stress induced in the material by the cutting process.
In this section we focus on the simulation of the laser cutting process of the iron foil M270–50A. As it was discussed for the SEM images, during the laser cutting process the area of the material which directly interacts with the laser beam evaporates instantaneously due to the high power involved in the process. However, we suppose that also the surrounding regions can reach temperature values high enough to modify the structural and the physical properties of the material. Indeed, it is well known that when a ferromagnet, like iron, is heated above a certain value of temperature, called Curie temperature $T_C$, it looses its magnetic

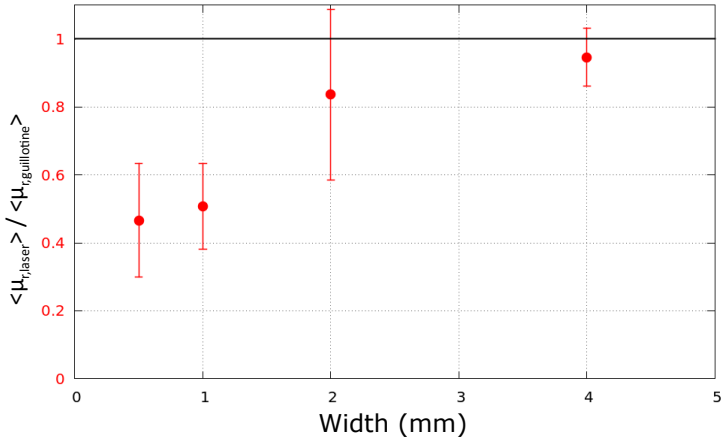


**Figure 2.15:** Ratio of the magnetic permeability between different cut processes as a function of the iron sample width.

behaviour and becomes paramagnetic [9].
With this situation in mind, we are interested in studying how the heat coming from the laser diffuses within the metal. With the aid of a FEM (Finite Element Method) software, the goal is to give an estimation of the amount of material damaged by the laser-cut process.

### 2.4.1 Geometry and parameters

Since M270–50A is composed by iron at 97%, as a first approximation we can consider it as pure iron. For this reason, we built in the simulation region a rectangular pure iron plate with length 250 mm, width 100 mm and thickness 0.5 mm, which can exchange heat by irradiation with air at room temperature.
On its bottom edge, we considered a smaller region of dimensions 100 mm × 5 mm × 0.5 mm with a finer mesh to optimize the computation. The actual shape of the sample is shown in Fig. 2.16. The mesh is made finer where the simulated laser cutting process happens, which is modelled by a moving gaussian heat flux, towards positive values in the $x$ direction, in the bottom side of the sample.
The properties of the heat flux, such as dimension of the source and its linear velocity, are consistent with the values of the machine used by the company producing the analyzed samples. However, since phase transitions are not implemented in the simulation, we cannot use the nominal value of power of the laser. As a matter of fact, by using the nominal power of the laser in the software, the temperature reached by the material is one order of magnitude greater than the evaporation temperature of the iron. Since this fact is physically meaningless, we set the power of the laser ad-hoc by fixing the maximum temperature reached in the simulation to be equal to the evaporation temperature of iron, which is $T_{\text{ev}} = 3134\,\text{K}$. In the following, a time–dependent analysis of the thermal distribution in the iron plate is outlined.

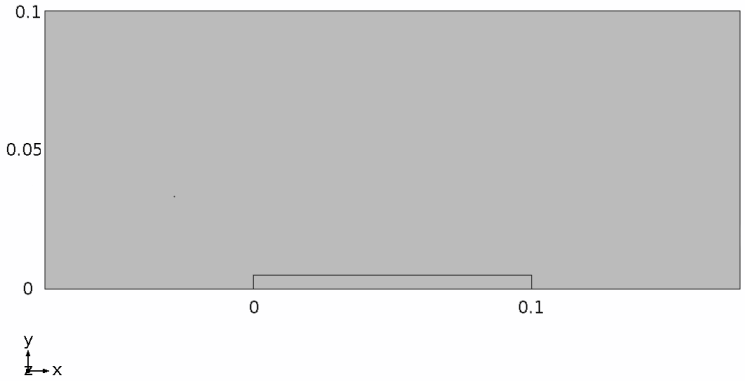


**Figure 2.16:** Simulated geometry.

### 2.4.2 Results

Fig. 2.17 shows a snapshot of the simulation results.
At first, we can notice that the maximum temperature value reached by the sample oscillates around $T_{\text{ev}}$, which we referred to be a systematic numerical error. This effect was attributed to our choice of the mesh, observing that it become less and less important choosing a finer one. However, in doing so, the computational time increased tremendously: it is possible to find a compromise, observing that this tradeoff does not spoil the goodness of the analysis since the shape of the isothermal curves does not change at different times.
We focused our attention on two characteristic isotherms: the Curie one at $T_C$ and the one corresponding to the melting temperature which is $T_{\text{melt}}$. These are reported in Fig. 2.18.
We set $T_C = 1043\,\text{K}$ and $T_{\text{melt}} = 1811\,\text{K}$, which correspond to the Curie temperature and the melting point of pure iron. Although we know that the presence of silicon (3%) lowers a little bit both $T_C$ and $T_{\text{melt}}$ of the iron, we did not find the the appropriate values in literature. A further improvement of the simulation should include them, to be more consistent with the sample composition.
In Fig. 2.19 the maximum temperature reached point by point along the perpendicular direction with respect to the motion of the laser ($y$ axis in our setup) is reported. This result tells us how deep the heat diffuses into the material in the laser-cut process.
From this information, we can actually give an estimation of the size of the area damaged by the laser cutting process. As a matter of fact, we assumed that the material which reached a temperature $T$ greater or equal to the melting one (*i.e.* $T \geq T_{\text{melt}}$) is damaged structurally causing a modification of its magnetic properties. However, a kind of magnetic modification occurs as well for those material

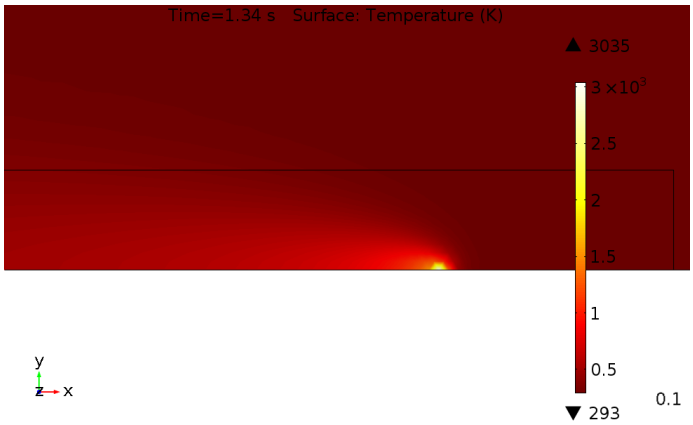


**Figure 2.17:** Thermal distribution in the sample at a fixed time. The brightest spot indicates the position of the laser.

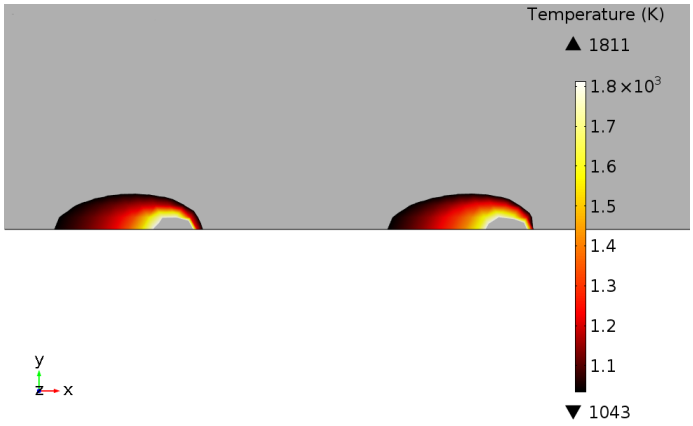


**Figure 2.18:** Thermal distribution between isothermal curves at Curie and melting temperature at two different times.

parts that have reached a temperature $T_{\text{melt}} \geq T \geq T_C$, since they exceeds the Curie temperature [2]. In order to know at which distance from the laser cutting line a given temperature $T$ has been reached, we fit the simulated data with the following double exponential function:

$$T_{\max}(x) = T_0 + T_a e^{-x/a} + T_b e^{-x/b}. \tag{2.9}$$

The fit parameters are reported in Tab 2.2. With this fit we observe that the melting temperature and the Curie one are attained respectively at $x \equiv x_{\text{melt}}$ and $x \equiv x_C$, whose values are:

$$x_{\text{melt}} \simeq 175\,\mu\text{m}, \qquad x_C \simeq 560\,\mu\text{m}. \tag{2.10}$$

The validity of these estimations could be experimentally checked and further investigated by adopting local probing techniques of the magnetic properties of

| $T_0$ [K] | $T_a$ [K] | $a$ [mm] | $T_b$ [K] | $b$ [mm] |
|---|---|---|---|---|
| 390 | 1548 | 0.23 | 802 | 1.3 |

**Table 2.2:** Fit parameters.

the material. One of this technique deals with Hall sensors [8].

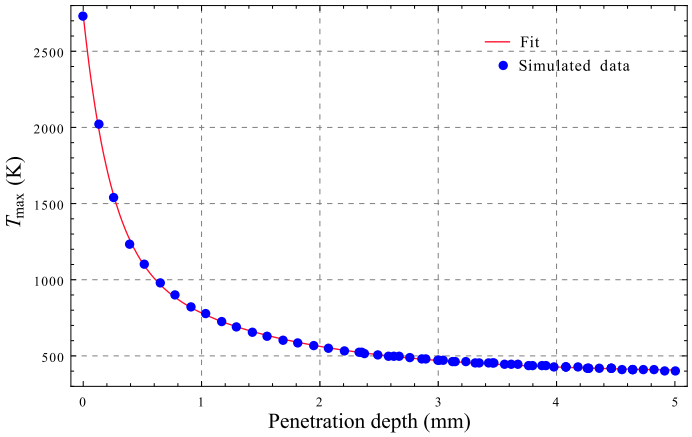


**Figure 2.19:** Maximum temperature reached by the material as a function of the penetration depth.

## 2.5 Conclusions and perspectives

During the IPSP2016 week event we followed three main approaches to solve the problem posed by the Bonfiglioli company: SEM images, magnetic measurements and simulations.
For what concerns the use of Scanning Electron Microscope (SEM), we were able to qualitatively appreciate the morphological differences in the samples between laser-cut and mechanical-cut. In particular, in the case of laser cutting, we have observed a small region of melted material (in the order of µm) where the sample magnetic property is degraded. This is confirmed also by the FEM simulation. In the case of guillotine technique, we observed a structural bent of about 50 µm wide. In this case, however, it is not easy to correlate the mechanical stress with a degradation of the magnetic properties. As a further step, we suggest to use SEM or other techniques to inspect magnetic domains in the bulk and on the edge of the laminations to estimate the damaged region by comparison between the size and the distribution of the domains.
We addressed the problem also from an experimental point of view, in order to estimate and predict the magnetic degradation of the laminations after the cut. We focused on three kind of measurements: hysteresis, power losses and frequency study.

- **Hysteresis**. This is an intrinsic source of energy loss and it must be taken into account in order to estimate the efficiency of an electric motor. We were able to explore the whole hysteresis curve for the 20 mm wide samples. We see a striking difference between the samples cut with the two methods, confirming the expected qualitative behavior: the laser-cut sample shows a reduced response (that is, a smaller magnetization at the same external field) with respect to the mechanical-cut one. For limitations in our instrumentation we were not able to do the same for the 40 mm wide samples, which have the greatest cross section, as we could not reach an high enough flux density to see saturation. From the hysteresis measurements we were able to compare the damage entity between the two different cutting methods.
  We suggest to improve this measure by using a higher range probe for measuring the $V_{out}$. In this way one could be able to see the saturation regime even in the wider samples.

- **Power losses**. This kind of measurement accounts for the total losses, a value ready to be implemented in any finite element simulation. Unfortunately, we were not able to find a definitive trend which characterizes the cutting techniques. As for the hysteresis measurement, an upgrade would then be to use a high current source. Consistent results may be achieved in future by increasing the statistics and by performing all the measurements systematically with the same overall steel mass, in order to minimize the errors in the measure.
  Moreover, in the Bertotti model (2.1) discussed in the introduction, which takes into account all the specific iron losses, the function for the power losses is fitted to BH curves measured at 50 Hz. However, it has been shown in Ref. [1] that the loss coefficients could be in principle both frequency and flux density dependent. Consequently, fitting the Bertotti model to BH curves measured at frequencies higher than 50 Hz, which is by the way the regime at which motors actually work, is advised in order to avoid underestimating additional sources of losses, which are expected to be relevant at higher frequencies.

- **Frequency study**. With this method we were able to evaluate the ratio between the averaged magnetic permeability of laser-cut and mechanical-cut samples. As expected, we found a lower permeability for the laser-cut ones. The measurement confirmed that the degradation effect is localized at the edge of the sample, as the effect was particularly evident in the case of thin samples, and becomes less important as the size of the specimen increases.

It is worth to remark that this measurements give as outcome a global result and can not provide a local study of the magnetic properties. However, to study the local properties of the material: one possible approach is the use of Hall probes, to recover a map of the magnetic permeability as a function of the plane coordinate of the lamination.
Finally, in the simulation we were able to evaluate the width $x$ of the damaged area from the sample edge for the laser cutting technique. This is intriguing, as

combining this study with the result of the hysteresis and frequency measurement it is possible to decouple the parameters of our effective model (cfr. Fig. 2.1). In particular, it is possible to estimate the value $\mu_{\mathrm{dmg}}$ of the magnetic response in the damaged area using the effective magnetic permeability measured in laboratory $\mu_{eff}$ and the tabulated magnetic permeability of FeSi provided by the supplier $\mu_{\mathrm{FeSi}}$.

$$\mu_{\mathrm{eff}} = \frac{x}{a}\mu_{\mathrm{dmg}} + \frac{a-x}{a}\mu_{\mathrm{FeSi}} \tag{2.11}$$

where $a$ is the total width of the iron foil. It would be interesting to check the validity of the simulation with a direct measurement of the surface distribution of temperature on the laminations $T(x, y)$ during the laser cut process.
It should be noted that a similar decoupling procedure can be done also for the mechanical-cut sample. Indeed, we know the ratio between the effective magnetic permeability from direct magnetic measurements and we can provide an estimation from SEM images of the damaged distance in the mechanical-cut sample.

# Bibliography

[1] M. Popescu, et al. "On the Physical Basis of Power Losses in Laminated Steel and Minimum-Effort Modeling in an Industrial Design Environment." Industry Applications Conference, 2007. 42nd IAS Annual Meeting. Conference Record of the 2007 IEEE. IEEE, 2007.

[2] R. Siebert, J. Schneider, and E. Beyer, "Laser cutting and mechanical cutting of electrical steels and its effect on the magnetic properties" IEEE Transactions on Magnetics 50.4 (2014): 1-4.

[3] C. W. Oatley, W. C. Nixon, and R. F. W. Pease, "Scanning electron microscopy." Advances in Electronics and Electron Physics 21 (1966): 181-247.

[4] Crevecoeur, Guillaume, et al. "Local identification of magnetic hysteresis properties near cutting edges of electrical steel sheets." IEEE Transactions on Magnetics 44.6 (2008): 1010-1013.

[5] Krings, Andreas, and Juliette Soulard. "Overview and comparison of iron loss models for electrical machines." 5th International Conference and Exhibition on Ecological Vehicles and Renewable Energies (EVER 10), Monte-Carlo, MONACO, MAR 25-28, 2010. 2010.

[6] `http://perso.uclouvain.be/ernest.matagne/ELEC2311/T2006/NOFP.pdf`

[7] `https://en.wikipedia.org/wiki/Power_factor`

[8] Besse, Pierre-A., et al. "Detection of a single magnetic microbead using a miniaturized silicon Hall sensor." Applied Physics Letters 80.22 (2002): 4199-4201.

[9] Crevecoeur, Guillaume, et al. "Analysis of the local material degradation near cutting edges of electrical steel sheets." IEEE Transactions on Magnetics 44.11 (2008): 3173-3176.

CHAPTER
# THREE

# BREAKING LOAD OF TWISTED YARNS

**P. Beraldini, S. Biasi, Z. Bisadi, T. Chalyan, M. Compri, D. Roilo, A. Gaspari, S. Piccione**

## 3.1 Introduction

### 3.1.1 The company

Eurotexfilati L.t.d. is a company based in Pietramurata, Dro (Trento) that was founded in 2012 as a company spin-off. Eurotexfilati is divided into two business units: the *Textile* section and the *Industrial* section. The Textile section commercializes yarns around the world. In the Textile section the dynamics of the market are analyzed to provide the best service for different applications such as technical clothing, hosiery, circular knitting and weaving (Fig. 3.1). The most


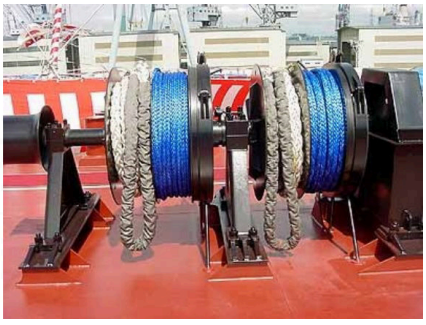

**Figure 3.1:** Some of the final applications of the half-processed products

treated yarns are Nylon6, Nylon66, polyester, polypropylene and elastic yarn (air jet and covered). The Industrial section processes industrial yarns such as high tenacity Nylon6, polypropylene and polyester by combining and twisting. These products are used by the customers in the production of ropes and braids, in particular for applications in the marine and fisheries sectors and for safety ropes.

### 3.1.2 The problem

The problem that Eurotexfilati L.t.d. proposed for IPSP2016 is related to the study of the variation of yarn breaking load as a consequence of processes such as twisting and splicing. Samples of the following materials were provided:

- 1880 Dtex PA6 HT (high tenacity Nylon6)
- 1100 Dtex PP HT (high tenacity polypropylene)

The processing steps to which these yarns are subjected are described in the following:

- pairing and torsion: the initial plies are paired and twisted in a single process to form the twisted yarn. The number of assembled ends is varying in a range of $3 \div 50$ and the number of twists is from a minimum of 8 TPM (twists per meter) to a maximum of 600 TPM. The instruments used to this task are the following: Twistechnology ® TWV-5/250 (TWV-300-1M), Roblon ® Tornado T300;
- re-winding: after the step of pairing and torsion, the twisted yarn is collected on metal spools. Therefore, a further operation is required to return the yarn on a cardboard tube (the standard support). This operation consists of simply withdrawing the half-processed product from the metal spool to the tube;
- splicing: it is an optional process aimed to limit the waste of material and optimize the production process. The principle of the process is to join two ends of different plies through an air welding in order to minimize the leftovers. The full bobbins can be re-used for the production of twisted yarns to be sold separately from the twisted yarns obtained from non-spliced yarns.

The solution to this problem would allow Eurotexfilati to improve the production efficiency (resulting in reduced waste) and provide a better ability to predict the properties of the products.

### 3.1.3 The strategy

Different approaches were used in the search for solutions to the proposed problems:

1. a literature overview was performed, in order to acquire information needed to better understand the physics underlying the studied phenomena and to get a general idea about the state of the art of the study about the breaking load of twisted yarns;
2. a systematic set of traction measurements was carried out on a set of samples as wide as possible, in order to compare the theoretical model with the experimental results;

3. numerical simulations were performed in order to cross-check both the model and the experimental data for the breaking load of twisted yarns;

4. traction tests were carried out also with spliced plies to shed some light on the phenomenology related to spliced joints and formulate some hypothesis on their use for commercial yarns.

## 3.2 Theory

### 3.2.1 Fundamentals of stress-strain analysis

In order to understand the behavior of the yarns when increasing loads are applied to them, it is worth to briefly introduce how a general material responds when an external force is applied to it. When a force is applied to an object, it causes a change in the object's shape or size, which is referred to as a deformation or strain. When this occurs, internal inter-molecular forces arise to oppose the applied force. These could be sufficient to completely resist the applied force and allow the object to return to its original state once the load is removed. If this is the case, it can be said that the object has undergone a reversible deformation, which is referred to also as an elastic deformation and is governed by the Hooke's law:

$$\sigma = E\epsilon, \tag{3.1}$$

where $\sigma$ is the applied stress (measured as a force per unit surface), $E$ the Young modulus of the material (having the dimensions of a stress), and $\epsilon$ the resulting dimensionless strain. The elastic behavior is described by a linear stress-strain relation (see Fig. 3.2, left) and lasts until the material reaches its yield strength. At this point the resulting deformation becomes irreversible and is referred to as a plastic deformation. When a material is plastically deformed, it does not return to its original shape after the removal of the applied force. Under tensile stress, a plastic deformation can be characterized by a strain hardening region and a necking region (see Fig. 3.2, right). During strain hardening the material becomes stronger through the movement of atomic dislocations. The necking phase is indicated by a reduction in cross-sectional area of the specimen. Necking begins after the ultimate strength is reached. During necking, the material can no longer withstand the maximum stress and the strain in the specimen rapidly increases. Plastic deformation ends with the fracture of the material.

### 3.2.2 Breaking load of twisted yarns

In the following, we will introduce a model able to describe the breaking load of a twisted yarn, which depends on several factors, such as the breaking force of each ply, the number of plies, the twisting angle, and the friction between the plies and the fibers constituting the plies themselves.
A simple model can be formulated as [3]:

$$F_{ty} = n\, F_p\, \cos(\beta), \tag{3.2}$$

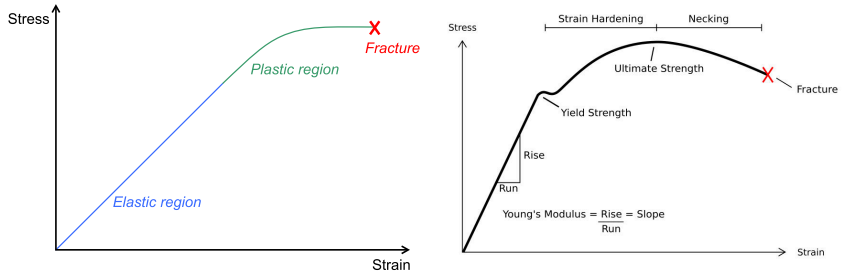


**Figure 3.2:** Examples of stress-strain curves, indicating the various stages of deformation. Reproduced from Refs. [1] (left) and [2] (right).

where $F_{ty}$ is the breaking force of the twisted yarn, $F_p$ the breaking force of a ply, $n$ the number of plies and $\beta$ the twisting angle, i.e. the angle between the axis of a ply and the applied load (see the graphical illustration reported in Fig. 3.3). The angle $\beta$ can be calculated using the following formula [3]:

$$\beta = \arctan(\pi\, d\, n_{tw}), \tag{3.3}$$

where $d$ is the diameter of a ply and $n_{tw}$ is the number of twists per meter. Equation 3.2 intuitively models the breaking load of the twisted yarn as being:

1. proportional to the number of plies and
2. decreasing with increasing twisting angle, as a consequence of the fact that $\beta$ is a measure of the misalignment between the plies (and hence the single fibers) and the direction of the applied load.

However, the simple formula in Eq. 3.2 does not take into account the effects of friction between plies and the ply characteristics (such as length, mobility and arrangement of the single fibers). To take this factors into account, a second term in Eq. 3.2 can be added [4]:

$$F_{ty} = n\, F_p\, \cos(\beta) - k\, n\, F_p\, \cot(\beta) = n\, F_p\, \cos(\beta)[1 - k\, \mathrm{cosec}(\beta)], \tag{3.4}$$

where $k$ is a coefficient accounting for the effects of friction and the properties of the single plies and where $n$ (not explicit in the original equation as reported in Ref. [4]), was introduced in order to take into account the presence of multiple plies making up for the twisted yarn. The former term on the right-hand side of the equation yields a decrease in the breaking force with the increase in twist and the latter yields an increase in the breaking force with increasing twist. The factor $k$ depends on ply properties as fiber length, radius and coefficient of friction. In particular, $k$ decreases (and therefore $F_{ty}$ increases) for increasing fiber friction coefficient.
A graphical representation of the theoretical relationship between the breaking load and twist (the number of turns per meter) is reported in Fig. 3.3. Starting from 0 TPM, as the twist increases, the breaking force increases up to a maximum (optimum twist) and then decreases. Schwartz [4] explains qualitatively

this relationship as follows. At zero twist, the fibers are aligned along the yarn's axis but without any binding forces. When the twist increases, the interaction between fibers increases due to the increase in traverse pressure. The breaking load increases since it must first overcome the friction between fibers (we note that in the general case a ply can be made of fibers shorter than the ply itself and that in the absence of fiber interaction, they may just slip out of the ply when a small load is applied to it). The binding between fibers will increase with increasing twist, and eventually the fiber breaking load will become the major contribution to the breaking load of the yarn (in fact, for sufficient fiber-fiber interaction, the slipping of fibers becomes irrelevant). For high twists, the angle between the fibers and the applied load gets large enough for the yarn breaking load to start decreasing.

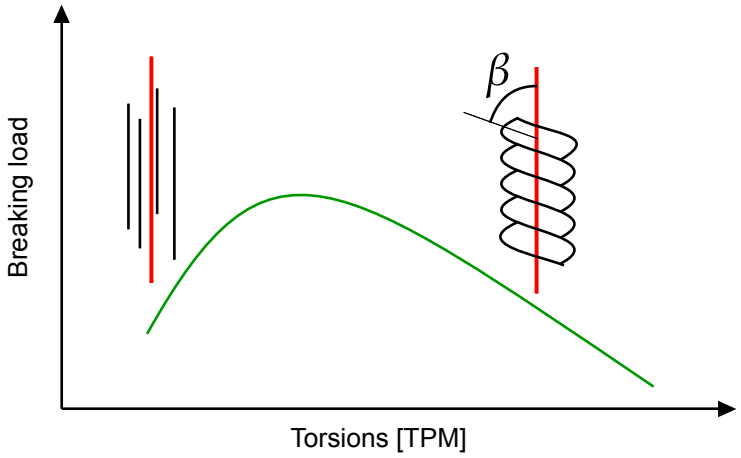


**Figure 3.3:** The theoretical breaking load-twist relationship.

The breaking load is not the only parameter to be influenced by the twist: a twisted yarn with a high level of twist behaves like a coil spring. It has low breaking force but high fatigue resistance. But the one with low level of twist acts more like a rod with higher breaking force but lower fatigue resistance [5]. Therefore, depending on the desired application, the twist level should be adjusted to achieve the specific intended properties.

## 3.3 Experimental

The apparatus used to measure the breaking load of the yarn is a metals traction test machine (Galdabini PMA10, see Fig. 3.4, left). In order to carry out measurements on polymeric yarns, the machine needed to be adapted as the clamps - designed for metal samples - could bias the measurements. Therefore, two self-made adapters were produced (see Fig. 3.4, right) and fixed to the machines

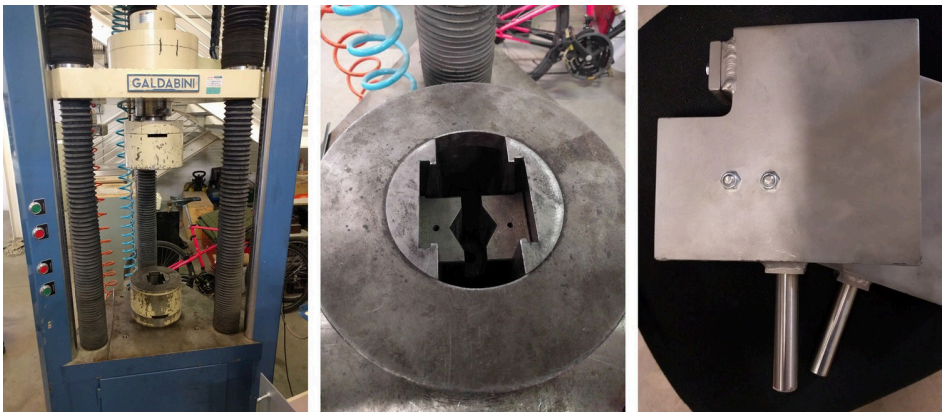


**Figure 3.4:** The traction machine used for the experiments (left), one of its clamps (centre) and the adapters used (right).

clamps.
The machine is controlled through a graphic user interface which permits to set the working conditions for every measurement. The experiments were carried out at constant rate of extension with the following conditions:

1. initial length of the sample: 250 mm;
2. extension speed: 100 mm/min;
3. maximum applicable load: 500 daN (lowest allowed value).

All the tests have been carried out at room temperature. Once a measurement starts, the traction machine applies the load needed for the extension to be constant in time at the specified value. The extension and the applied load are constantly recorded during the experiment. When the sample breaks, the measurement is automatically interrupted. The machine provides, at the end of each measurement, a printed output containing the following information:

1. parameters of the measurement;
2. breaking load and final load;
3. breaking extension and final extension;
4. stress-extension plot.

The analysed samples are made of two different materials: Nylon6 1880 Dtex and Polypropylene 1100 Dtex. Yarns of each material have been tested by changing the number of plies and the number of twists. Spliced yarns were also tested. The samples used for testing are indicated below:
1. Nylon6 (PA6):

- 1880 x6 parallel (no twist)

- 1880 x6 S20-S60-S80-S120
- 1880 x12 S20-S60-S80-S90-S100
- spliced plies

2. Polypropylene (PP):

- 1100 x6 parallel (no twist)
- 1100 x6 S20-S60-S120

Each twisted yarn is identified by a letter indicating the direction of the twist and a number indicating the TPM. In our case, all yarns were S-twisted, meaning that the twist is clockwise [6].
In order to allow software analysis of the stress-strain curves, the plots printed by the testing machine have been digitized. To cross-check the obtained results and maximize the available experimental information, a further set of measurements was commissioned by Eurotexfilati to an independent laboratory based in Pastrengo (Province of Verona, Italy).

## 3.4 Results and discussion

The systematic study performed on twisted yarns of Nylon6 and polypropylene allowed us to analyse the breaking load as a function of the TPM and to compare the experimental results with the analytical predictions discussed in section 3.2.2. Each yarn has been tested by measuring the breaking load for at least three samples. As a result, an average value of the breaking load and a standard deviation have been computed for each sample.
In the following, we report the sets of data which have been obtained by two different laboratories and testing machines (i.e. the results obtained at the University of Trento, labeled as UniTn, and the ones obtained by the independent laboratory based in Pastrengo, labeled as IndLab). It was observed that the results obtained by the two laboratories were in agreement with each other (measurements carried out on the same samples by the two laboratories gave compatible results inside the experimental errors in the large majority of the cases), demonstrating the reliability of the measurements performed in the IPSP week. Thanks to the observed reproducibility, the data obtained at the University of Trento and the data obtained by the independent laboratory could be analyzed together as a single data-set. As it has already been explained in section 3.3, during an experiment the twisted yarns are slowly extended up to breaking by the testing machine. During the proof, the force applied is recorded as a function of the sample deformation.
Figure 3.5 shows the applied force against the elongation of 6 parallel yarns of Nylon6. The linear part of the graph consists in an elastic reversible elongation of the system. The second part of the graph is characterized by a nonlinear behavior. Here, it is worth noticing that in contrast to the usual stress-strain curves of the metals (see for example Ref. [7]), where typically the derivative of the applied force with respect to the strain decreases, in the Nylon6 curve such derivative

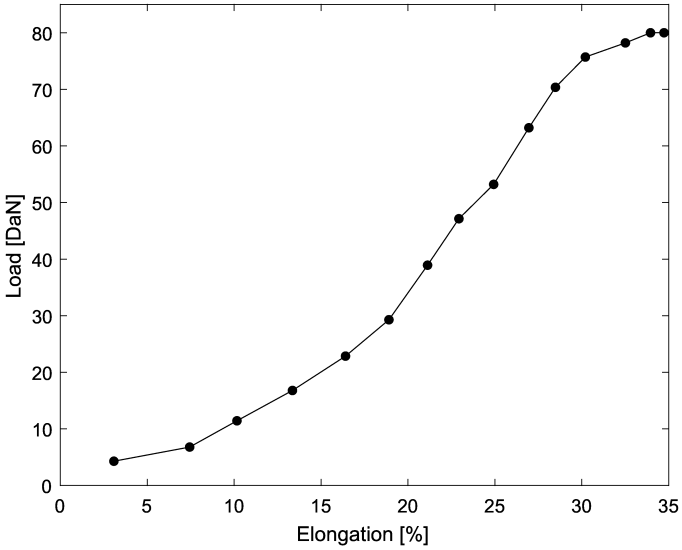


**Figure 3.5:** Experimental load applied as a function of the elongation for 6 parallel (0 TPM) plies of Nylon6.

increases. This strain-stress behavior can be connected to the alignment, along the traction axis, of the fibers composing the plies and to the corresponding increase of their cohesion. In fact traction has two effects on the ply: i) the fibers align parallel to the load and ii) they are brought closer together and interact more. These two effects will become clearer soon in the following, on a more macroscopic level, for twisted yarns where the alignment of the fibers brings an increase of the cohesion and produces an increase of the tensile strength. The deformation is extended until the maximum of the strain curve, also known as *final load*, is reached. This gives us the experimental value of the breaking load for the system under consideration. Such a measurement has been performed at least five times so that an average value of the braking load for the 6 parallel plies has been computed. In this way, we could obtain a first estimation of the breaking force $F_p$ of a ply.

Figure 3.6 shows the plot of the applied force as a function of the elongation of 6 parallel plies of polypropylene. Such medium displays a larger linear region with respect to that observed for Nylon6 (see Fig. 3.5). The final load reached is lower than it is for Nylon6 and the nonlinear deformation does not exhibit the peculiar behaviour followed by the Nylon6 curve. This effect can be physically interpreted in terms of the friction between the fibers in the hypothesis that the friction coefficient of Nylon6 against itself is lower than that of polypropylene against itself, as reported in Ref. [8]. A higher coefficient of friction limits the relative movement of the fibers composing the plies, thus leading to a larger increase of the applied force derivative with respect to the elongation in the nonlinear regime. In our

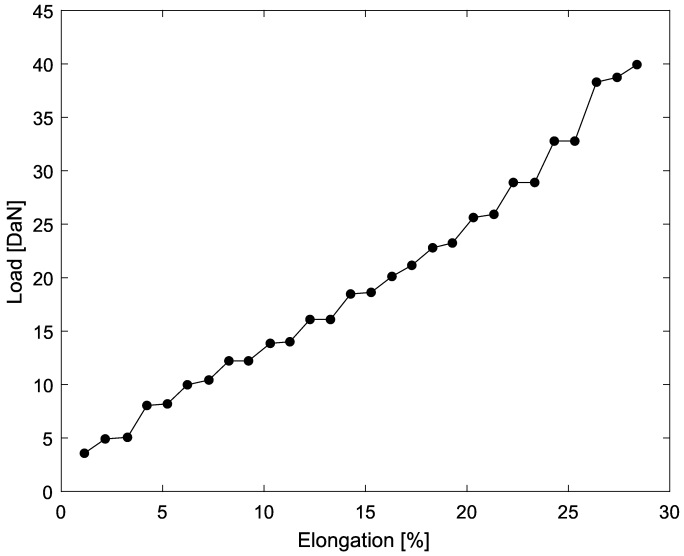


**Figure 3.6:** Experimental load applied as a function of the elongation for 6 parallel plies of polypropylene.

case, it has not been possible to directly measure the friction coefficient of the materials making up for the plies under investigation.
Figure 3.7 shows the force applied against the elongation for a 12 ply yarn of Nylon6 with a twist number of 60 TPM. As previously mentioned, there is a sensible increase of the derivative of the applied force with respect to the elongation after the linear regime. This effect can be attributed to the rearrangement of the fibers which leads to a distribution of the force along the traction axis and then an increase of the strain derivative.
Figure 3.8 shows the experimental breaking load as a function of the TPM for 12 ply twisted yarns of Nylon6. The data are fitted by using the analytical model described by Eq. (3.4) so that the red curve is obtained. We have used as fit parameters the $k$ coefficient, the ply diameter $d$ and the breaking force of a ply $F_p$. The green dots represent the data measured by the independent lab (IndLab), while the blue dots represents the values obtained at the University of Trento (UniTn). The theoretical model is in good qualitative agreement with the experimental results. Looking at the fit parameters reported in the figure caption, we notice that the dimensionless $k$ value is much smaller than one (it is of the order of $10^{-5}$ for all samples comprising 6 ply Nylon6, 12 ply Nylon6 and polypropylene), meaning that for these yarns, the role of friction is limited. Hence, it can be stated that the main contribution to the dependence of the breaking load on the twist is given by the projection of the load on the yarn's axis, even for relatively low TPM.
Let us analyze the behavior of the breaking load as a function of the twist. At

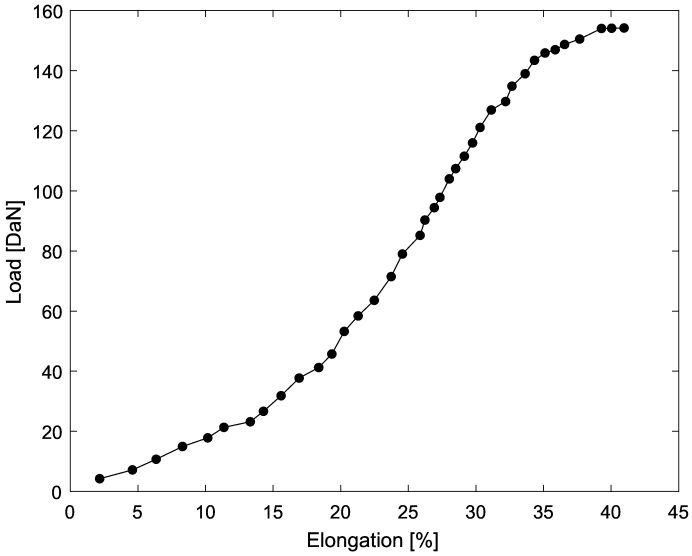


**Figure 3.7:** Experimental load applied as a function of the elongation for 12 ply yarns of Nylon6 with 60 TPM.

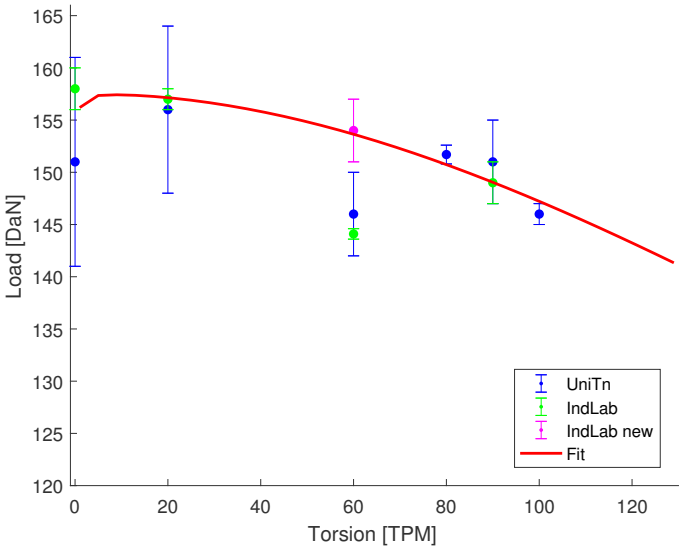


**Figure 3.8:** Experimental average breaking load against the number of twist for 12 ply twisted yarns of Nylon6. Fit parameters: $k \simeq 3.6 \times 10^{-5}$, $d \simeq 1.22$ mm , $F_p \simeq 13.1$ DaN

zero TPM, the breaking load is not at its maximum, as it would be expected according to the simple theory described by Eqs. (3.2) and (3.3). For low TPM, the lack of cohesion between the fibers leads to a non-maximum breaking force. With increasing twists, the breaking load increases due to a higher interaction between the fibers and, increasing the twists further, the breaking load decreases as a consequence of the increasing angle $\beta$ between the fibers and the load direction.
The points for the 60 TPM sample reported in Fig. 3.8 show a divergence from the expected value for both the IndLab and UniTn measurements (samples from the same reel have been analysed by the two laboratories). This discrepancy has been attributed to some structural defects of the samples used in the proof. Actually, successive tests on new Nylon6 trials (60 TPM) exhibited experimental values of the breaking force in agreement with the theoretical curve (see the magenta point in Fig. 3.8).
Figure 3.9 displays the experimental breaking force against the number of twist for 6 ply Nylon6 yarn. Here, the analytical curve is in good agreement with the measurements of both testing machines. Moreover, the fit parameters of 12 ply and 6 ply yarns of Nylon6 are comparable. However, it has to be noted that the obtained value for $F_p$ ($\approx$ 13 DaN) is not compatible with the specifications of the plies. The data sheets, in fact, report for these plies a tenacity of 80.5 cN/Tex and a linear mass density of 1905 Dtex, resulting in a breaking load of approximately 15.3 DaN (we remind that the tenacity is the ratio between a yarn's breaking load and its linear mass density). This discrepancy has been detected independently by both laboratories and its origin is still an open point.
Figure 3.10 shows the breaking load as a function of the twist number for 6 ply yarns of polypropylene. Here, too, the fit with the analytical model reproduces the experimental data. In any case, the diameters of the plies are comparable with the data sheet values, and for this material also the measured breaking force ($F_p$ = 6.83 DaN) of a single ply is in agreement with the one declared in the datasheet (in the range 6.9$\div$7.3 DaN) .

## 3.5 Numerical simulation

To validate the proposed theoretical model, numerical simulations were performed. This was possible with the use of a *Finite Element Method* (FEM) software, which exploits a numerical technique to obtain approximate solutions for partial differential equations. The problem can be solved by reducing it into smaller and simpler parts, which are called finite elements. The equations modeling the entire problem consist of the sum of all the simpler equations which describe each single finite element.
It was decided to run the simulation only for yarns composed of Nylon6. The reason for this choice is mainly due to the experimental data with which we can compare the results from the simulation.
The simulation was performed in order to understand the mechanical response of the yarns, for different numbers of torsions per meter, under an applied force. The used software module took into account also the nonlinear behavior of the

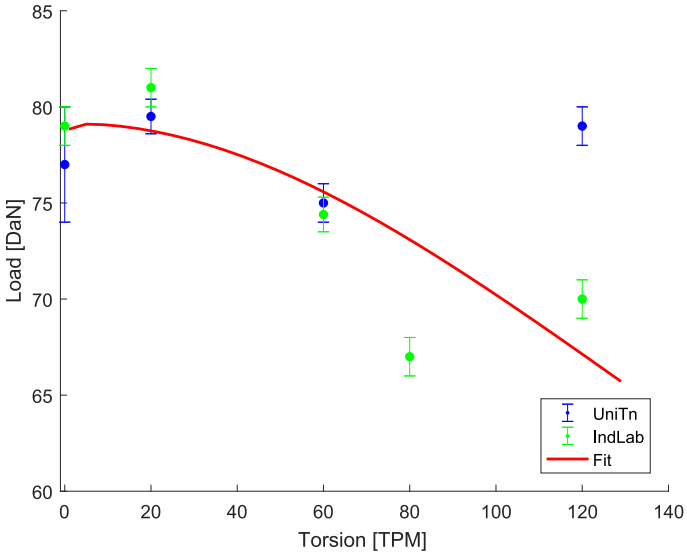


**Figure 3.9:** Experimental average breaking load against the number of twist for 6 ply twisted yarns of Nylon6. Fit parameters: $k \simeq 2.37 \times 10^{-5}$, $d \simeq 1.66$ mm, $F_p \simeq 13.2$ DaN

material.
The first step in the simulation was the study of the plastic regime for the different geometries, without considering the eventual fracture of the yarn. The simulation has been performed in the perfect plasticity regime, which refers to the property of materials to undergo irreversible deformation without any increase in stresses or load. Two common criteria are used to describe the material yielding: the Tresca and the Von Mises criteria.
The Von Mises criterion, which is the one used in the simulation, can be formulated in terms of the equivalent tensile stress or von Mises stress, $\sigma_y$, a scalar stress value that can be computed from the Cauchy tensor. This last consists of nine components that completely define the state of stress at a point inside the material, in the deformed state. The von Mises stress can be defined as:

$$\sigma_y^2 = \frac{1}{2}\left[(\sigma_{11}-\sigma_{22})^2 + (\sigma_{22}-\sigma_{33})^2 + (\sigma_{33}-\sigma_{11})^2 + 6\left(\sigma_{23}^2+\sigma_{31}^2+\sigma_{12}^2\right)\right]. \tag{3.5}$$

A material is said to start yielding when its von Mises stress reaches the critical value, also known as the yield strength, $\sigma_y$. The von Mises stress is used to predict yielding of materials under any loading condition from results of simple uniaxial tensile tests. Details can be found in Refs. [9] or [10].
To correctly run the simulation it is necessary to know both the Young modulus and the yield strength. In literature it was found that the Young modulus is equal

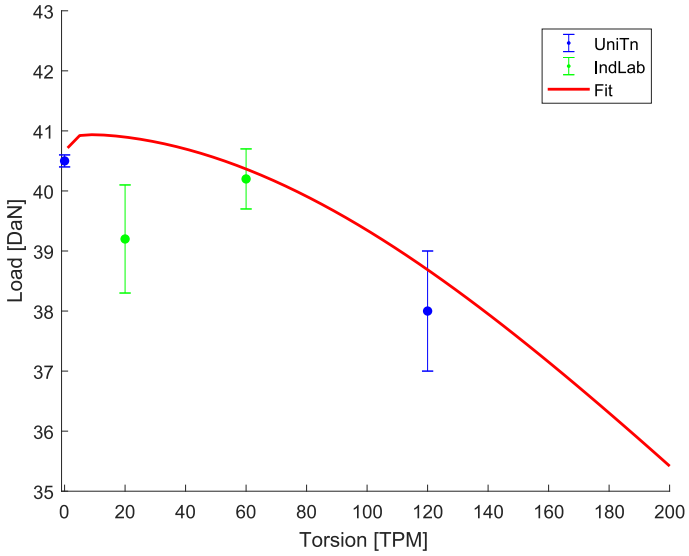


**Figure 3.10:** Experimental average breaking load against the number of twist for 6 ply twisted yarns of polypropylene. Fit parameters: $k \simeq 1.87 \times 10^{-5}$, $d \simeq 0.93$ mm , $F_p \simeq 6.83$ DaN

to $E = 2.7$ GPa, while it was not possible to find an unique value for the yield strength. By looking at Ref. [11] we set $y_s = 100\,\text{MPa}$.
The simulated structure consisted of six single plies twisted together. Fig. 3.11 shows an image of the used geometry. In the simulation it has been neglected the viscous contribution due to the ply-ply frictions, which opposes to the applied load. This is of course an approximated study, but allowed to reduce the computational time. A more accurate study is necessary to make a good comparison between the experimental data and the simulation results possible.
Figure 3.12 evidences the plastic behaviour of the twisted yarn, showing the dependence of the strain on the applied load, for different number of torsion per meter. From Fig. 3.12 it is immediately possible to see the differences between the three cases.
To validate the proposed theoretical model, the knowledge of the breaking load for each twisted yarn was necessary. However, the performed simulation, up to now, is not able to tell us this value correctly. Fortunately, thanks to the collected experimental data, we know what is the maximum strain, in percent, that can be reached by the yarn before the fracture. At this point it is possible to evaluate the value of the load corresponding to that strain, for different values of torsion per meter, or twisting angle. The obtained results are reported in Fig. 3.13.
The simulated trend resembles the proposed theoretical behaviour, as it is shown by the red curve in Fig. 3.13 resulting from the fitting of the simulated values with a cosine function.

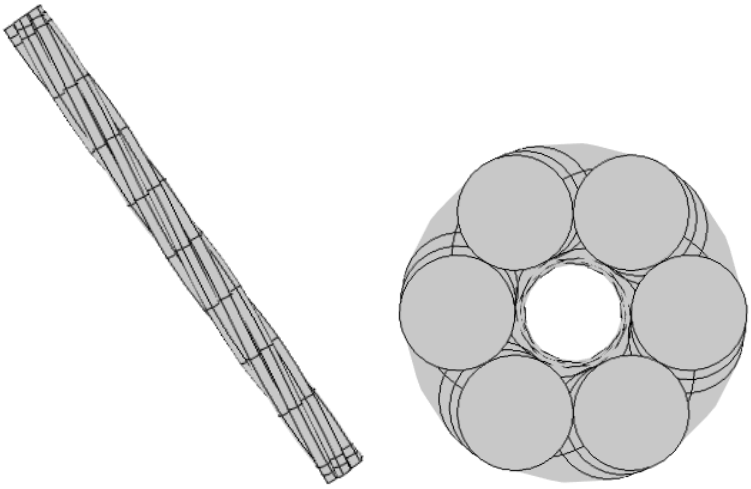

**Figure 3.11:** Simulated geometry. Six plies twisted together.

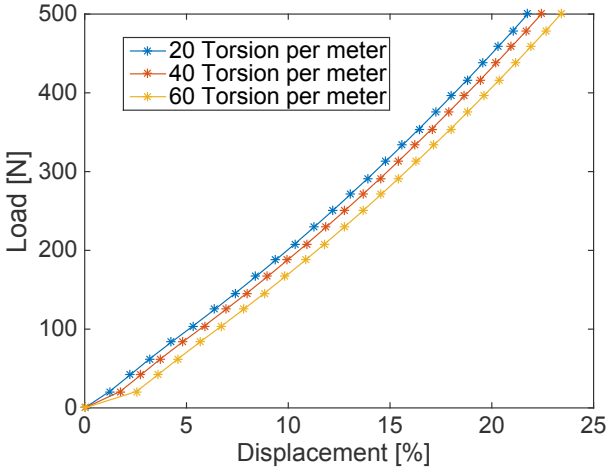


**Figure 3.12:** Simulated stress-strain curve for different values of torsions per meter

The simulation performed describes a simplified model and a more accurate study would be necessary to draw a conclusion, nevertheless it is possible to see a similarity with the proposed theoretical model, which is a further proof of correctness.

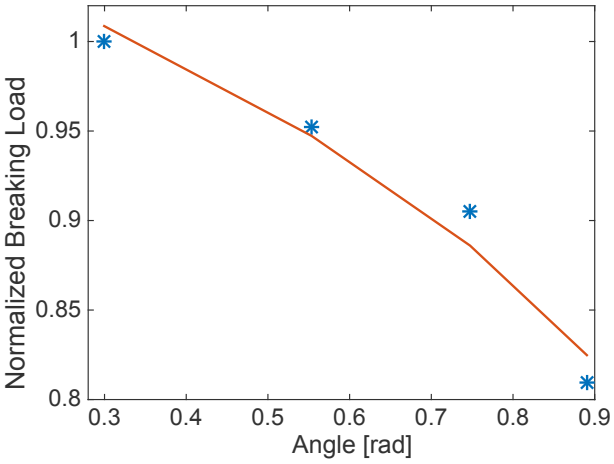


**Figure 3.13:** Simulated dependence of the breaking load on the twisting angle. The red curve is the result of the fitting procedure.

## 3.6 Splicing

### 3.6.1 Overview on the technology

Today splicing is the most used technique for joining plies. It consists on a pressurized air jet that entangles the ends of the two plies, joining them into a continuous element (Fig. 3.14). The effectiveness of type of junction depends on

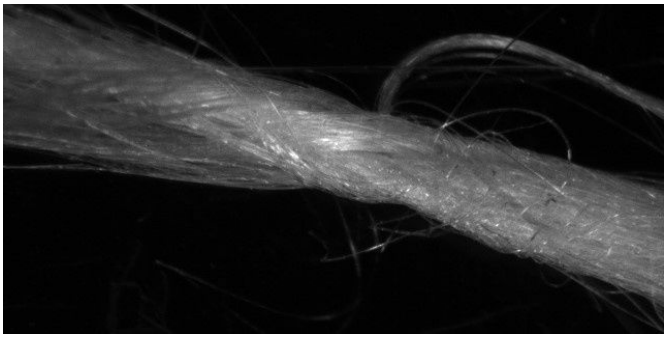

**Figure 3.14:** A spliced yarn

the equipment and on the operator using it, so it is hard to have the certainty that every connection is well made. Moreover it is almost impossible to develop a theoretical model or study the problem with a finite elements software due to the random nature of the process. The machine used for tests was a manual splicer that usually works at an air pressure of 9 bars (Fig. 3.15).

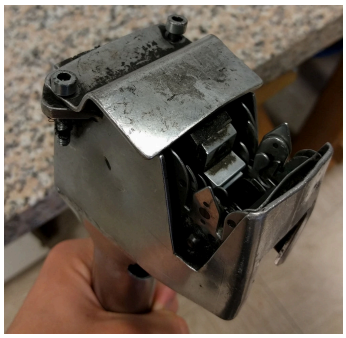

**Figure 3.15:** The splicer used for the experiments

| Pressure [Bar] | Breaking load loss $\ell$ [%] | | # of slipped joints | # of broken plies |
|---|---|---|---|---|
| | Average | Stand. Dev. | | |
| 5 | 61 | 11 | 16 | 9 |
| 7 | 29 | 6 | 2 | 4 |
| 9 | 25 | 4 | 4 | 16 |

**Table 3.1:** The average breaking load loss $\ell$ of the tested plies and the number of slipped joints/broken plies for different splicer operating pressures.

### 3.6.2 Experimental

Our task was to determine how many joined yarns would be possible to put in a multi-yarn in order to guarantee an adequate level of security. We made almost 50 tests on a PA6 1880, pulling plies spliced at different pressures. Due to the limited availability of the traction machine described in section 3.3, some of the measurements on spliced yarns were carried out with a simple dynamometer, which did not allow to control the extension speed. We observed two possible outcomes for the traction tests on spliced plies:

- the ply breaks when the breaking load of an intact ply is reached;
- the spliced joint slips at a lower load.

The results, shown in Tab. 3.1, are expressed in *breaking load loss* $\ell$, obtained subtracting from one the ratio between the slipping point load ($F_{sp}$) for a spliced ply and the breaking point for an intact ply:

$$\ell = 1 - \frac{F_{sp}}{F_p}. \tag{3.6}$$

The average measured values for $\ell$ at different splicer's operating pressure are reported in Fig. 3.16. We can see that for low splicer's operating pressure, many spliced joints slip at a very low load, whereas for an operating air pressure of 9 bars the number of jointed plies that slip is very low.

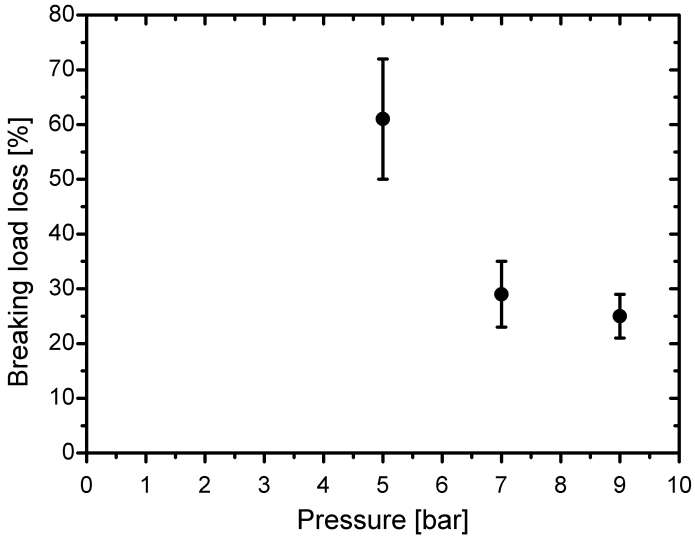


**Figure 3.16:** The average breaking load loss of spliced plies, plotted as a function of the splicer's air pressure

### 3.6.3 Results and discussion

Starting from the measurements presented above, a simple model can be proposed in order to tell how many plies have to be added to the yarn in order to compensate for the loss of breaking load due to the presence of spliced plies. This model implies three assumptions: i) all the spliced plies have the same breaking load loss $\ell$ (note that in principle this is not verified: the loss in breaking load is different for every spliced ply and in the above section we gave an average value for it); ii) the load applied to the yarn is evenly distributed across all plies composing it and iii) the role of impulsive loads (i.e. loads applied in a very short time) can be neglected, as long as they do not exceed the breaking load of the plies. The latter assumption corresponds to assuming that the breaking load of a ply does not depend on the extension speed.

If the above assumptions hold, every spliced ply will fail when a load $F_{sp} = F_p(1 - \ell)$ is applied to it. Therefore, if the yarn is composed of $n$ plies, the spliced plies will fail when a load $F_l = n\,F_p(1 - l)$ is applied to the yarn, no matter how many spliced plies are present in it. For the yarn not to break when a spliced ply fails, it is necessary that the not spliced plies together have a breaking load higher than $F_l$. Calling $n_S$ the number of spliced plies contained in the yarn, $n_{NS} = n - n_S$ the number of not spliced plies contained in the yarn it can therefore be written that, in order for the yarn not to break when a spliced ply fails, the following condition has to hold:

$$n_{NS}F_p \geq nF_p(1 - \ell), \tag{3.7}$$

from which the following relation can be obtained:

$$n \geq \frac{n_S}{\ell}. \tag{3.8}$$

We note that the above relation does not give information on the breaking load of the yarn.

### 3.6.4 Future perspectives

The model proposed is very simple and based on a limited number of samples. It has been studied for a specific combination of hypothesis, so it gives only a direction for a future study, not a working standard. A future study should investigate the splicing method for pressures higher than 9 bar and improve the proposed model applying it to twisted yarns. The effect of the presence of intact plies around the spliced one (and therefore the presence of friction and cohesion) should be investigated to study whether the spliced plies could give a contribution to the breaking load, independently from the quality of the splicing point. If this would be the case, yarns containing spiced plies could be put on the market and a minimum (worst case scenario) breaking load could be estimated. Anyway, at the current point it must be stressed that, starting from the studies carried out so far during the week of IPSP, no conclusion can be drawn on the breaking load of twisted yarns containing spliced plies.

## 3.7 Conclusions

During the IPSP week, different approaches have been adopted to investigate the proposed problem. First of all, the current literature on the topic has been studied in order to learn what factors have the strongest influence on the breaking load of twisted yarn and to see whether theoretical models already existed. Repeated experiments have been carried out using a traction testing machine in order to collect a systematic set of data on yarns of different materials and having different number of plies and twist. Although being relatively simple, Eq. 3.4 has been found to correctly reproduce the breaking load measured in two different laboratories. The fit parameters obtained from the analysis of the experimental data can therefore be used as a good starting point to qualitatively estimate the breaking load of the twisted yarns. A further confirmation of the validity of the model was provided by the numerical simulation.
It must be noticed that other factors can play a role in determining the breaking load of the yarns, as it has been demonstrated by the fact that measurements on different samples having the same nominal specifications (specifically, the 12 ply S60 Nylon6 in our case) can yield different breaking load values. Systematic measurements carried out on a larger set of samples would give more complete information on the breaking load of twisted yarns.
For what concerns the splicing, some points become evident from the study carried out. First of all, the efficiency of the splicer depends on the pressure of the air with which it works. It seems that higher air pressure corresponds to higher

splicing quality, i.e. the plies spliced at high pressure have a higher probability to break away from the splicing, displaying the same breaking load as an intact ply. Secondly, it is impossible to predict the behavior of spliced plies: some of them have the same breaking load of intact plies and break in points away from the spliced joint. In other cases, anyway, the spliced joint simply slips off when a small load is applied. This observation evidences the fact that it is possible to obtain spliced plies having the same breaking load and the intact plies. Hence, it cannot be excluded that further studies and improvements of the splicing technique and of the tools used for it may lead to fully reliable spliced plies.

# Bibliography

[1] Moondoggy. Stress-strain1.svg. https://en.wikipedia.org/wiki/File:Stress-strain1.svg, 2008. Licensed under the Creative Commons Attribution-Share Alike 3.0 Unported license.

[2] Breakdown. Stress Strain Ductile Material.png. https://commons.wikimedia.org/wiki/File:Stress_Strain_Ductile_Material.png, 2008. Licensed under the Creative Commons Attribution-Share Alike 3.0 Unported license.

[3] J. Stepanovic, D. Radivojevic, V. Petrovic, and S. Golubovic. Analysis of the breaking characteristics of twisted yarns. *FIBRES & TEXTILES in Eastern Europe*, 18(2):40–44, 2010.

[4] P. Schwartz. *Structure and mechanics of textile fibre assemblies.* Elsevier, 2008.

[5] A.S. Hockenberger and S. Koral. Effect of twist on the performance of tire cord yarns. *Strain*, 2:3, 2004.

[6] A. Barnett. *Examining Textiles Technology.* Heinemann, 1997.

[7] ASM International. *Atlas of Stress-strain Curves.* ASM International, 2002.

[8] A.J. Peacock. *Handbook of Polyethylene: Structures, Propertues, and Applications.* Marcel Dekker, 2000.

[9] Abdel-Rahman A. Ragab and Salah Eldin Ahm Bayoumi *Engineering Solid Mechanics: Fundamentals and Applications.* CRC Press, 1998.

[10] W.F. Hosford *Mechanical Behavior of Materials.* Cambridge University Press, 2005.

[11] http://www.gplastics.com/pdf/cast-nylon-6.pdf.

CHAPTER

# FOUR

# THE COOLING PROCESS OF A REFRACTORY BRICK

**M. Borghi, M. Brighenti, C. Castellan, M. Cervino, G. Germogli, M. Rossignoli, A. Saha, S. Signorini**

## 4.1 Introduction

### 4.1.1 The company

Saint-Gobain is a multinational corporation based in Paris, with more than 350 years of expertise in engineered materials. Nowadays, it is one of the world leading companies in the fields of habitat and construction markets [1]. It designs, manufactures and distributes building products, transforming raw materials into advanced products with an extreme interest to innovation. Saint-Gobain is one of the top 100 industrial groups in the world, providing in 2015 €43.2 billion of sales with about 193 000 employees in 64 countries.
SEPR Italia Spa is part of the Saint-Gobain Group [2]. It was founded in 1960 in Mezzocorona (Trento, Italy), and operates in the production of refractory materials for the glassmakers. The products of SEPR Italia are realized for being part of glass furnaces in multiple fields, which span from flat glass to container glass, wool fiberglass, reinforcement fiberglass and special glasses. SEPR Italia products are realized by AZS, which are composites of alumina ($Al_2O_3$), zirconia ($ZrO_2$) and silica ($SiO_2$). The zirconium dioxide percentage characterize the quality of the product: the larger the zirconia percentage, the larger the resistance of the refractory block to corrosion.

### 4.1.2 The production process

The main step for the production of the refractory bricks is the fusion of the AZS powder. This process is achieved by means of electrofusion. Three graphite electrodes are suspended over the powder, liquefying it through electrical discharges.

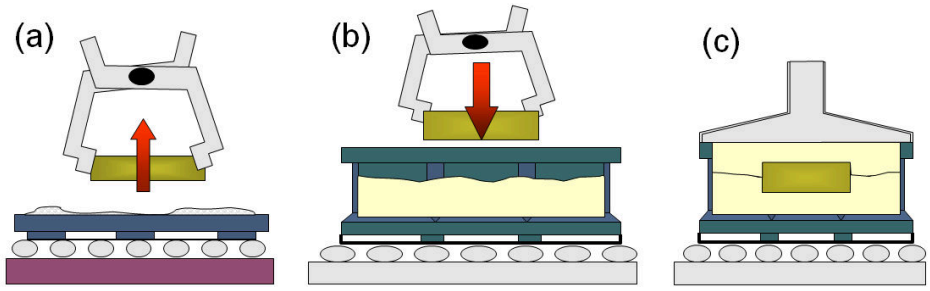


**Figure 4.1:** Transfer of the refractory block from the sand mold to the cooling box. (a) Extraction of the block from the sand mold. (b) Deposition in a box filled partially by the insulating material. (c) Final filling of the box with the insulating material.

The fused material at about 1800 °C is then poured into the sand mold. As soon as the external crust of the brick begins to harden, it is moved from the sand mold to another box, where it is completely surrounded by alumina. This transfer process is represented in Fig. 4.1. Alumina is a good heat insulator and allows the slow cooling of the refractory brick, preventing the formation of cracks in the final solid product. When the brick is cold, it is extracted from the box. After some mechanical processing, it is ready to be mounted for its final application.

### 4.1.3 The problem

The problem proposed by SEPR Italia is related to the optimization of the cooling process of the refractory bricks. The company requires to individuate the best insulating material to use for the coverage of the block during the cooling process, comparing the material which is currently used (alumina) with some other insulants present on the market (such as vermiculite or diatomaceous earth). Moreover, the company is interested in the individuation of a new method for the choice of the cooling time of the blocks. Up to now, it is determined taking into account only the mass of the blocks, using a table where only 6 categories are present. However, it is a matter of fact that also the shape of the block matters, determining different cooling times for blocks with the same mass but with different shape. For this reason, the company requires to individuate a new method to determine the cooling time, taking into account also a factor related to the shape of the block. All this study is motivated by the interest to understand better the cooling process, in order to optimize the cooling time of the blocks, reducing the lead time, in order to detect more quickly the production waste and to optimize the entire production process.

### 4.1.4 The strategies

During the IPSP2016 week, the group of young researchers working to the problem proposed by SEPR Italia was divided in two subgroups.
One group was dedicated to the comparison of the alumina thermal properties with the thermal properties of vermiculite and diatomaceous earth. This part is

described in section 4.2. For doing that, three methods were used. First of all, the cooling process was reproduced in laboratory by heating a refractory block in an oven and measuring its cooling temperature variation when surrounded by different insulating materials. Moreover, a thermal conductivity measurement was performed using the hot wire method. The results obtained from hot wire measurements were then validated using another approach to estimate the alumina thermal conductivity.
The other group studied the cooling process of the blocks. This work is described in section 4.3. First of all, a new prescription for the cooling times has been proposed, passing from the actual 6 groups to 24 groups and reducing the average storage time of about 9%. Moreover, the experimental cooling measurements were compared with the results deriving from finite element simulations. By means of these simulations, the effect of the block shape on its cooling time has been analyzed, introducing a new factor that takes into account the shape of the block and that can reduce the cooling time of more than 20% for some bricks. Moreover, the simulation study allowed to determine a new important parameter in the cooling process that the company was not taking into account, which is the position of the block in the cooling box.

## 4.2 Thermal features of the insulating materials

In this section, the experimental analysis of the thermal properties of the different cooling materials is proposed. Alumina, vermiculite and diatomaceous earth are compared in two ways. From one side, the block cooling process is reproduced in laboratory. From the other side, an experiment based on the hot wire method is performed in order to determine the material thermal conductivity. Finally, to compare the different methods, the alumina thermal conductivity is estimated monitoring the cooling temperature at three different distances with respect to the refractory block.

### 4.2.1 Estimation of the cooling performances by reproducing the brick cooling process

The first experimental analysis of the brick cooling process has been designed to reproduce the one performed by the company, which is depicted in Fig. 4.1(b-c) and consists in the following steps.

1. Partial filling of the empty box with the insulating material.
2. Transfer of the brick in the box.
3. Complete filling of the box with the insulating material for the cooling process.
4. Storage of the box in the warehouse to guarantee a slow cooling of the brick.
5. Removal of the brick from the box when its temperature is about 150 °C.

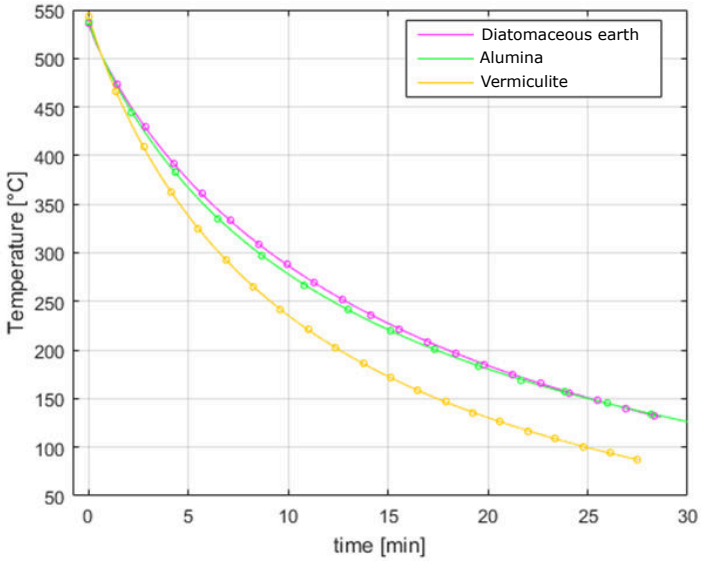


**Figure 4.2:** Brick annealing process reproduced in laboratory. The brick cooling temperature as a function of time is taken using the insulating materials listed in the legend.

During the IPSP2016 week an experimental apparatus able to reproduce this process in laboratory and to collect the cooling curves has been realized. Without lack of generality, the cooling box has been reproduced with a stainless steel tube with an internal diameter of 7.15 cm, a thickness of 0.5 cm and a height of 25 cm. We used a small cylindrical refractory brick produced by SEPR Italia with a height of 2.6 cm and a diameter of 0.85 cm. The refractory brick was placed in an oven, heating it to the temperature of about 1200 °C. During the heating of the sample the basis of the tube was filled with the insulating material. The hot sample was then moved in the prefilled tube, and a thermocouple was placed on the top facet of the brick. In order to ensure all the temperature measurements to be taken in the same position, a small hole was previously realized on the top facet of the refractory brick. The sample was then covered with the insulating material and the temperature was recorded until reaching about 100 °C.
This procedure was repeated three times for each of the three insulating materials: alumina, vermiculite and diatomaceous earth. The cooling curves referring to a set of measurements for the three materials are shown in Fig. 4.2, reporting the temperature registered by the thermocouple as a function of time. They show that diatomaceous earth and alumina have nearly the same insulating performances, while vermiculite lets the bricks cooling down faster. It is known from the company that a fast cooling of the brick causes the formation of residual stresses in the material that may compromise it. Therefore, for the company's purposes vermiculite is the worst material, while diatomaceous earth and alumina show a similar behavior according to our experimental setup.

### 4.2.2 Thermal conductivity measurement using the hot wire method

The performance of the three insulating materials can be estimated also by a direct measurement of their thermal conductivity. Thermal conductivity is the property of a material that quantifies the heat conduction capability of the material itself, and is measured in $[\mathrm{Wm^{-1}K^{-1}}]$. Heat transfer occurs at a higher rate across materials with high thermal conductivity than across materials with low thermal conductivity.

During the IPSP2016 week, a standard method for the thermal conductivity measurement was realized. This method is referred in literature as transient hot wire method [3]. The method is a transient dynamic technique based on the measurement of the temperature rise at a defined distance from a linear heat source embedded in the test material. By assuming the heat source having a constant and uniform output along the length of the test piece, the thermal conductivity can be estimated from the resulting change in temperature over a known time interval [4].

The mathematical model used to describe this process is based on the assumption that the hot wire is ideal, infinitely thin and long, surrounded by an infinite volume of homogeneous and isotropic material, with a constant initial temperature $T_0$. Let $q$ be the constant quantity of heat production per unit time and per unit length of the heating wire (measured in $[\mathrm{Wm^{-1}}]$) initiated at time $\mathrm{t} = 0$. Then a radial heat flow around the wire occurs, and the temperature rise $\Delta T(r,t)$ at radial position $r$ from the heat source is described by the following equation [5]:

$$\Delta T(r,t) = T(r,t) - T_0 = -\frac{q}{4\pi k}\mathrm{Ei}\left(-\frac{r^2}{4at}\right), \tag{4.1}$$

where Ei refers to the the exponential integral function, $k$ is the thermal conductivity of the material and $a$ its thermal diffusivity, defined as $a = k/\rho c_p$, being $\rho$ the density and $c_p$ the isobaric heat capacity. For a sufficiently long time $t$ and a small distance $r$ the exponential integral can be simplified getting the following simplified formula:

$$\Delta T(r,t) = \frac{q}{4\pi k}\ln\left(\frac{4at}{r^2 C}\right), \tag{4.2}$$

where $C = \exp(\gamma)$ and $\gamma$ is the Euler constant ($\gamma \sim 0.577$). By considering the slope $K$ of the temperature rise $\Delta T(r,t)$ as a function of the natural logarithm of the time evolution $\ln(t)$, one can derive the thermal conductivity as:

$$k = \frac{q}{4\pi K}. \tag{4.3}$$

In our experiment, we prepared the setup shown in Fig. 4.3. A metallic wire with high resistivity ($R/L = 0.96\ \Omega/\mathrm{m}$) was tightened by a weight in the center of a metallic cylinder of 20 cm of height and 6.5 cm of diameter. The position of the wire was set using two metallic sticks in order to provide a reproducible positioning below 1 mm. Two thermocouples entered laterally from two holes, purposely designed at half of the height of the cylinder, and were placed at a distance from

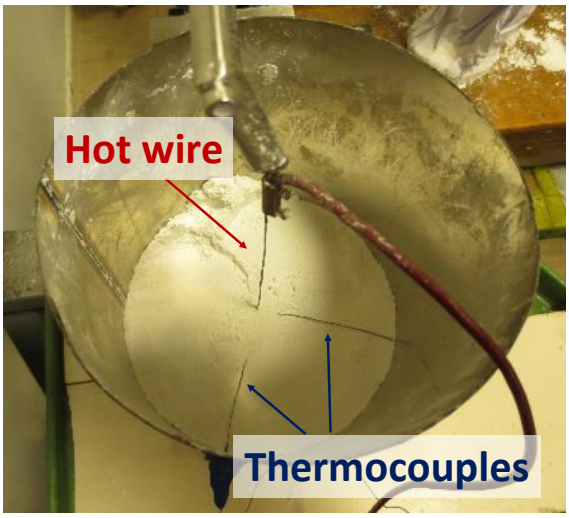


**Figure 4.3:** Experimental setup for the thermal conductivity measurement with the transient hot wire method.

the wire of (1.0±0.1) cm and (2.5±0.1) cm respectively. The cylinder was then completely filled with the insulating material, in such a way that the distance between the thermocouples and the wire was one order of magnitude lower than the length of the wire and of the amount of insulating material. A continuous potential of few volts was applied to the extremes of the wire. The electrical current flowing through the wire produced heat through the Joule effect, which progressively caused the heating of the surrounding material. In such a heating regime, the temperature as function of time was simultaneously recorded with the two thermocouples. The experimental curves are reported in Fig. 4.4. A linear fit of temperature against $\ln(t)$ was done after the first transient, where the wire impedance effect take place. The results are reported in Tab. 4.1, and show that the thermal conductivity of alumina is comparable with the one of diatomaceous earth, while they are both about 4 times smaller than vermiculite. These results agree with the ones reported in section 4.2.1, where the cooling of a refractory brick was studied.
In the right column of Fig 4.4 a zoom of the temperature behavior in the first few minutes of heating is shown. One can observe a larger delay in the temperature rise of the most distant thermocouple in the case of alumina (i.e. 550 seconds at a distance of 1.5 cm), with respect to the cases of vermiculite and diatomaceous earth (respectively of $\approx$ 20 s and $\approx$ 40 s at the same distance). This effect is due to the different thermal inertia of the materials, that is related to their different specific heat.
So, in our experiment we observed a lower heat propagation velocity in alumina with respect to other materials. This fact guarantees a better performance of this powder in the industrial application, where a slow cooling process is required.

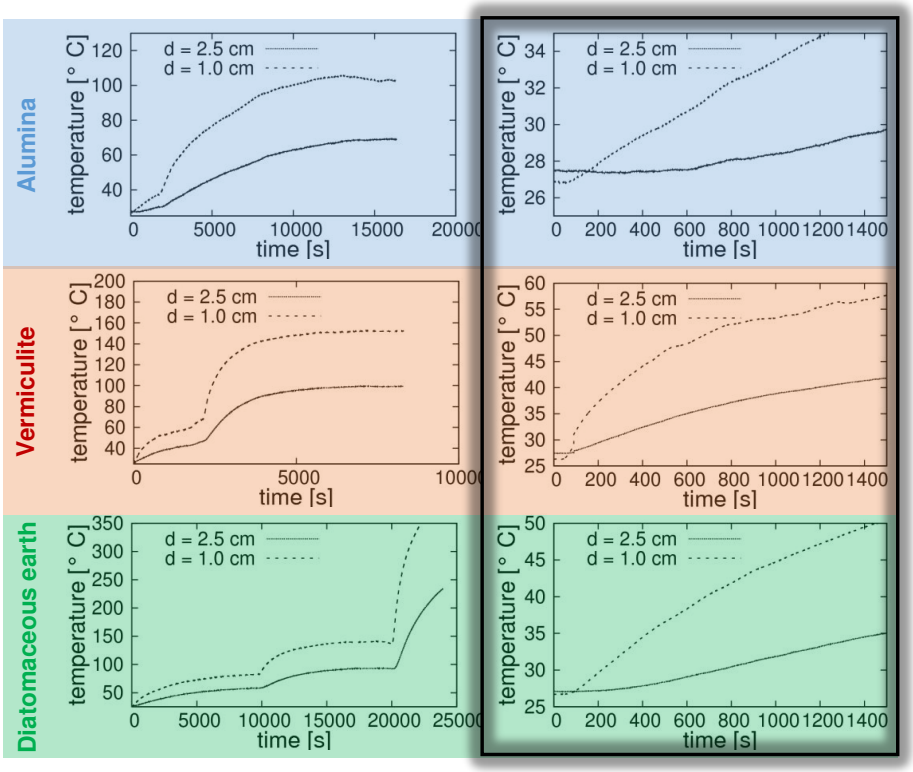


**Figure 4.4:** On the left column the experimental curves obtained by heating alumina, vermiculite and diatomaceous earth are shown. Each discontinuity in the plots is given by a variation of the current through the hot wire. On the right column, it is reported a zoom on the first heating region of the plots shown on the left side.

| Material | Thermal conductivity ($\mathrm{Wm^{-1}K^{-1}}$) |
|---|---|
| Alumina | $0.165 \pm 0.015$ |
| Vermiculite | $0.53 \pm 0.05$ |
| Diatomaceous earth | $0.143 \pm 0.015$ |

**Table 4.1:** Thermal conductivity of alumina, vermiculite and diatomaceous earth measured using the hot wire method.

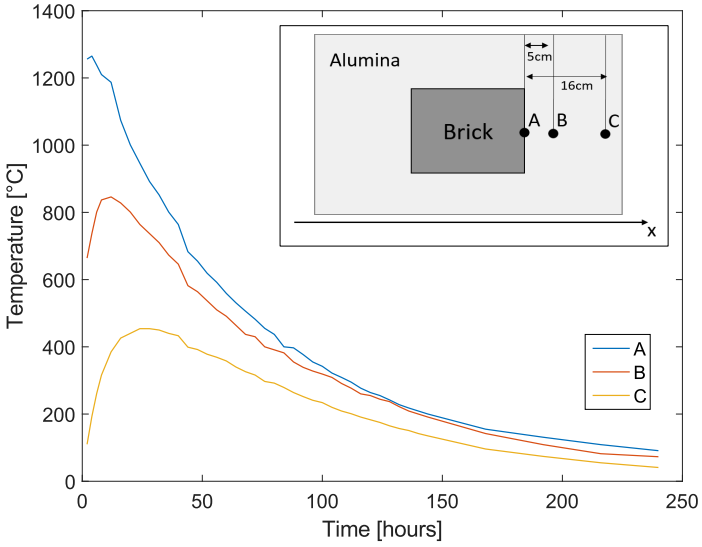


**Figure 4.5:** Cooling curves at the spatial positions A (blue), B (red) and C (yellow) defined in the inset.

### 4.2.3 Alumina thermal conductivity measurement using the double derivative method

In this section another method used for the estimation of the alumina thermal conductivity is shown. This procedure has been used to validate the measurements taken in the previous section using the hot wire method. This method is based on the heat equation, which describes the behavior of the material temperature $T$ in time and space:

$$\frac{\partial T}{\partial t} - a\nabla^2 T = 0, \tag{4.4}$$

being $t$ the time coordinate and $a$ the thermal diffusivity of the material. Simplifying the heat conduction problem to a one dimensional problem, Eq. (4.4) can be rewritten as:

$$\frac{\partial T}{\partial t} - a\frac{\partial^2 T}{\partial x^2} = 0, \tag{4.5}$$

being $x$ the heat propagation direction.

The company provided us some experimental cooling curves taken on a parallelepiped block with dimensions of $(60 \times 40 \times 30)$ cm$^3$ using alumina as cooling material. The cooling measurements were taken by means of three thermocouples at three different positions from the brick surface, which are respectively 0 cm, 5 cm and 16 cm, as it is described in the inset of Fig. 4.5. This means that, for each of the three positions along the $x$ direction (A, B, C), there is an experimental cooling curve of the brick, as it is shown in Fig. 4.5. From these curves

the space and time derivatives can be evaluated, and reassembling Eq. (4.5) it is possible to evaluate $a$ as:

$$a = \frac{\partial T}{\partial t} \Big/ \frac{\partial^2 T}{\partial x^2}. \tag{4.6}$$

Once that $a$ is known, the thermal conductivity $k$ can be derived from the definition of the thermal diffusivity $a = k/\rho c_p$, since $\rho$ and $c_p$ are known for alumina. According to this approach, we found $k = (0.21 \pm 0.06)$ $\mathrm{Wm^{-1}K^{-1}}$. The agreement of this result with the measurement performed with the hot wire method provides a further validation of the results obtained in that way.

## 4.3 Optimization of the cooling process

In this part we describe the study realized on the brick cooling process. First of all, a new storage mechanism able to reduce the mean storage time of about 9% is proposed. Some experimental cooling curves are then analyzed, from which some inexplicable features appear. In order to find an explanation to these facts, we developed a computational model, on the basis of which the role of the brick shape and of its position in the cooling box are analyzed.

### 4.3.1 New storage mechanism

The actual prescriptions adopted by the company to determine the cooling time required by the blocks is based on the principle that blocks of the same mass (and so, the same volume) require the same time to cool down. However, in the table currently used only 6 categories are present, and blocks of very different masses are stored for the same cooling time. At the same time, blocks with similar masses can be stored for a very different time if they belong to the boundaries of different categories. We proposed to improve this fact increasing the number of the storage categories. Fitting with a polynomial curve the storage times that the company is currently using, we got a new classification formed by 26 categories. Assuming to have a family of blocks equally distributed between 0 and 900 kg, it is estimated that this new mechanism can lead to a reduction of the average storage time of the in-stock blocks of about 9%.

### 4.3.2 Experimental study of the bricks cooling times

In order to study and optimize the cooling times of the bricks during the cooling process, we analyzed some experimental cooling curves provided by the company and referred to blocks with different shapes. In this way we aimed to give an estimation of the characteristic time required by the bricks to cool down. We analyzed the cooling curves of bricks having the following shapes:

- 2 cubic blocks of edge length 40 cm and 42.4 cm respectively;
- 3 spheres of radius 20 cm, 24.8 cm and 29.3 cm respectively;
- 1 parallelepiped with dimensions $(30 \times 40 \times 60)$ $\mathrm{cm^3}$.

| Shape | Dimensions | Mass (kg) | Fitted cooling time (days) |
|---|---|---|---|
| Sphere 1 | r = 20.0 cm | 120 | 11 |
| Sphere 2 | r = 24.8 cm | 247 | 13 |
| Sphere 3 | r = 42.4 cm | 406 | 20 |
| Cube 1 | L = 40.0 cm | 247 | 15 |
| Cube 2 | L = 42.4 cm | 294 | 14 |
| Parallelepiped | $(30 \times 40 \times 60)$ cm$^3$ | 278 | 12 |

**Table 4.2:** Characteristic cooling time estimated by the fit of the experimental data.

Some examples of the cooling curves provided by the company are reported in Fig. 4.6. The data were collected by means of a thermocouple placed on the surface of the brick. The initial temperatures are between 1200 °C and 1400 °C, while after 120 hours $300-400$ °C are reached. The temperature value in time was fitted with an exponential profile of the form $\exp(-t/\tau)$, through which the characteristic time constant $\tau$ was extracted. From the analysis of the experimental cooling curves we obtained an estimation of the cooling time by taking $4\tau$, in order to consider the cooling process fully ended. The results of this analysis are shown in Tab. 4.2 and in Fig. 4.7. From the analysis of these results, two contradictions appear.

1. Considering the parallelepiped, which is more massive than one of the two cubes, we can see that it takes less time to cool down. This contradicts the principle currently used by the company, which prescribes longer cooling times for the more massive blocks. This fact points out that it is necessary to introduce a new parameter for the estimation of the cooling time which has to take into account also the block shape.

2. Considering the two cubes, the cooling time of the more massive brick is shorter than the cooling time of the smaller one. In this case the shape of the two blocks is the same, but the larger one takes less time to cool down. This fact is a further contradiction of the principle currently used by the company, and states that the mass cannot be used to estimate the cooling time even for blocks with the same shape.

These contradictions will be treated in the following sections and, by the help of finite element simulations, an explanation will be provided. Moreover, some hints for the better estimation of the cooling times of the blocks will be given.

### 4.3.3 Introduction to the FEM model

In order to provide a tool for the study of the cooling process of the bricks, a computational model based on the Finite Element Method (FEM) has been implemented. With a computational model it is possible to simulate the physical

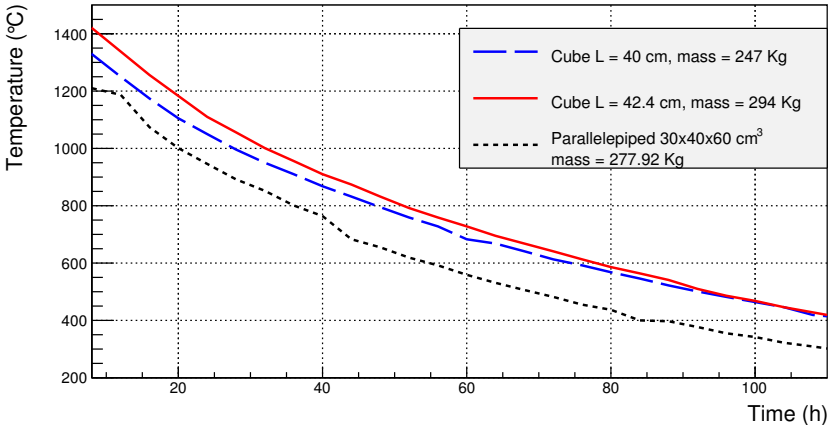


**Figure 4.6:** Experimental cooling curves of bricks having different masses and shapes. The curves refer to two cubes and to a parallelepiped. The cooling curves relative to other blocks show similar behaviors.

behavior of samples that have not been built practically. This is a great advantage, because with a simulation it is possible to explore a wider amount of physical conditions and configurations than with an experiment, in a faster, easier and cheaper way.

We considered first of all the geometry of the problem. As it is sketched in Fig. 4.8, the cooling of the brick occurs in a metallic box filled by alumina. The thickness of the alumina layer on the different sides of the brick can change depending on the shape, volume and position of the brick itself. The thermal conductivity of the metallic box is so high that it is almost transparent to the heat flux involved in the cooling process and so it is not considered in our simulation.

After the geometry, we defined the physical properties of the materials involved in the simulated system. Since we have to study the cooling process of the brick, we need to provide to the model the thermal properties of the materials, which are the density $\rho$, the heat capacity at constant pressure $c_p$ and the thermal conductivity $k$.

At this point we had to define the boundary conditions of the problem. As it is shown in Fig. 4.8, the simulation takes into account a geometry where all the faces of the alumina cladding are exposed to air, except for the bottom side, that is in contact with the ground. According to this, we considered the effect of the air convection on the boundaries that are not in contact with the ground. Due to the thermal connection with the ground, the bottom side was assumed to be at a constant temperature.

With all these parameters fixed, the model is complete, and the FEM software can be used to compute the thermal response of the system. The software solves the heat equation over all the regions defined by the geometry and takes into account all the properties defined by the materials and by the boundary conditions. From

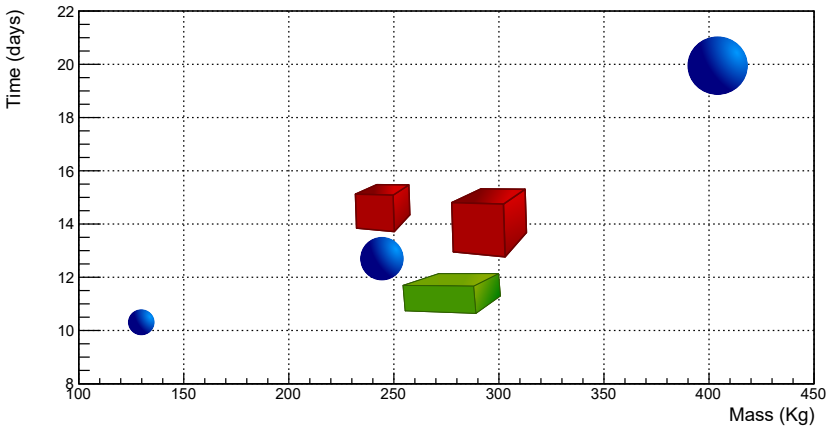


**Figure 4.7:** Experimental cooling times for blocks with different mass and shape.

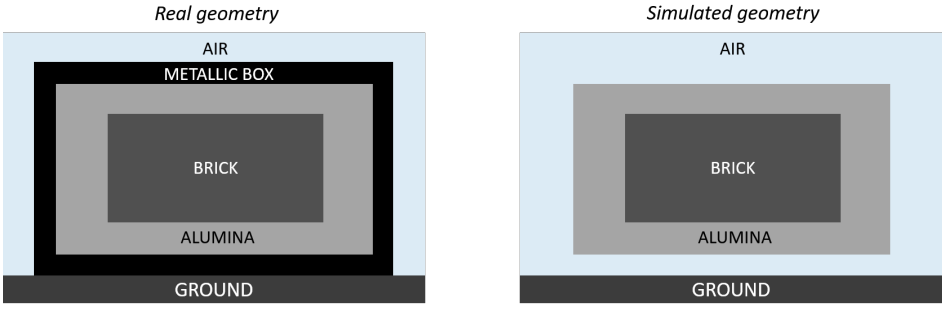


**Figure 4.8:** (Left) Geometry of the system involved in the cooling process of the brick. (Right) Geometry used in the FEM model.

the output of the simulation it is possible to obtain the thermal behavior in time, that is the cooling curve of the system.
However, the model considered here assumes all the involved materials as solid, while in reality the alumina is a powder. Moreover, the real cooling process involves phase transitions, that are not taken into account in our simulation. In order to consider these effects without simulating them practically, we adopted an effective approach. The idea is to compare an experimental cooling curve with the one simulated for the same geometry of the experiment. An arbitrary coefficient is multiplied to the thermal conductivity, and this coefficient is changed until the simulation fits the experiment. In this way, we find an effective thermal conductivity to reproduce the experimental results getting rid of the approximations related to the phase transitions and the powder nature of alumina.
In Fig. 4.9 the comparison between the FEM model and the experiment is reported for one specific geometry, showing that the simulation reproduces well the reality. Moreover, in Fig. 4.9 it is also reported a fit of the experimental cooling

curve with a double exponential function. The double exponential fit offers a better agreement with the experimental curve than a single exponential fit. This fact suggests the presence of two distinct dynamics in the cooling process, one faster (related to the heat conduction) and one slower (due to convection). This means that two distinct characteristic times are associated to these two dynamics. The contribution to the brick cooling due to the convection appears after the conduction because the convection can lower the temperature only when the heat reaches the interface between alumina and air. So the main contribution to the cooling process comes from the conduction, that is always present. The presence of these distinct processes is confirmed also by the analysis of the simulated cooling curve, which shows the double exponential behavior if we consider both the conduction and the convection processes. If we neglect the convection mechanism in the simulation, the cooling curve behaves as a single exponential.

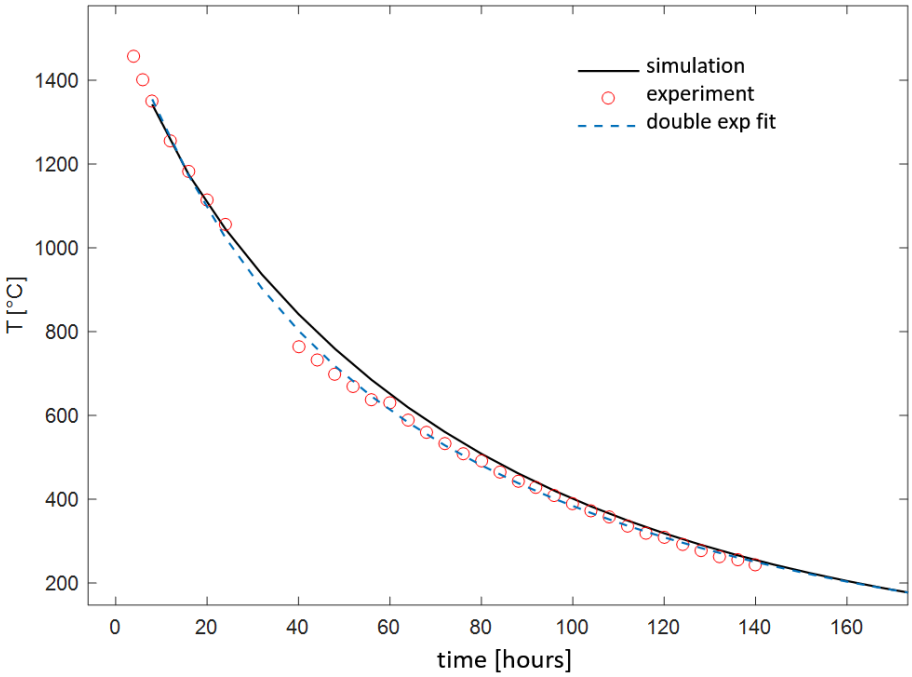


**Figure 4.9:** Comparison between the simulated and the experimental cooling curve. The plot refers to a parallelepiped block with dimensions $(30 \times 40 \times 60)$ cm$^3$. Some of the experimental data in the plot are missing due to a temporary switch off of the thermocouple. In the plot it is also reported a double exponential fit of the experimental cooling curve.

From now on, for reasons of simplicity, we consider the brick temperature $T$ as its average temperature when analyzing the results coming from the simulation. Moreover, we consider the cooling time $\Delta t$ as the time taken by the brick to pass from the average temperature of 1400 °C to an average temperature of 200 °C.

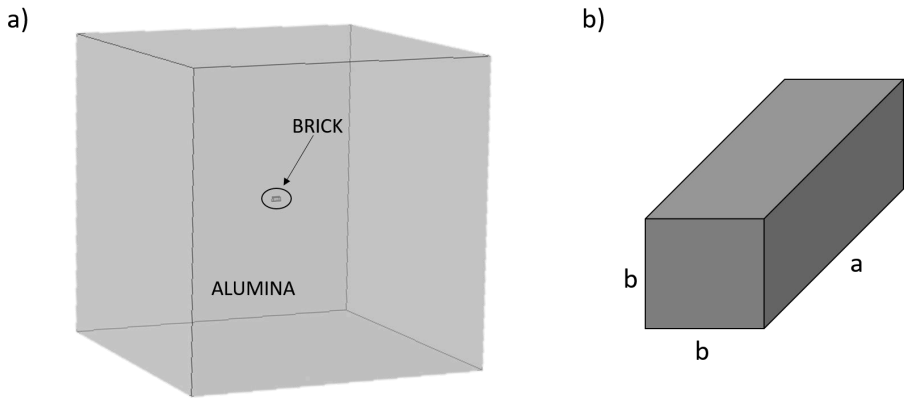


**Figure 4.10:** (a) Configuration used for the study of the role of the brick shape on the cooling time. The brick is covered by a large amount of alumina, in order to avoid the border effects. (b) Brick geometry used in the simulation.

### 4.3.4 The role of the brick shape

Using the FEM model described so far, the first contradiction reported in section 4.3.2 has been investigated. That contradiction refers to the fact that, among the experimental cooling curves of the bricks, there is a parallelepiped of 278 kg that takes 12 days to cool down, while a cube of 247 kg takes 15 days. This result goes against the common idea that a longer cooling time is required by a brick with a larger mass. However, it can be observed that the two compared bricks have different shapes. In order to investigate further this fact, we studied the role of the brick shape in the cooling process.
To study the shape effect on the cooling mechanism, we got rid of the border effects by covering the brick with a thickness of alumina that is enough to avoid the effect of the air on the cooling process, as it is shown in Fig. 4.10(a). Moreover, we considered several bricks with the same mass (and so, the same volume), but with different shape. By performing the simulations with these constrains, the changes in the cooling time are due only to the shape of the brick. To simplify the simulations the brick has been chosen as a square based parallelepiped with a base side $b$ and a depth $a$, as it is shown in Fig. 4.10(b). The idea was to change $a$ and $b$ while keeping fixed the volume of the brick. In this way we simulated several bricks with the same mass but different shape. The result is reported in Fig. 4.11, where the cooling time $\Delta t$ is plotted as a function of the brick depth $a$. From the plot it can be observed that the longest cooling time is required by the block with the minimum surface, which corresponds to the cubic shape. Shorter cooling times are computed with larger surfaces, i.e. with parallelepiped shapes. From this outcome we concluded that the shape plays an important role in the cooling time. In particular, keeping constant the mass, blocks with larger surface to volume ratio require a smaller cooling time. Considering the company typical

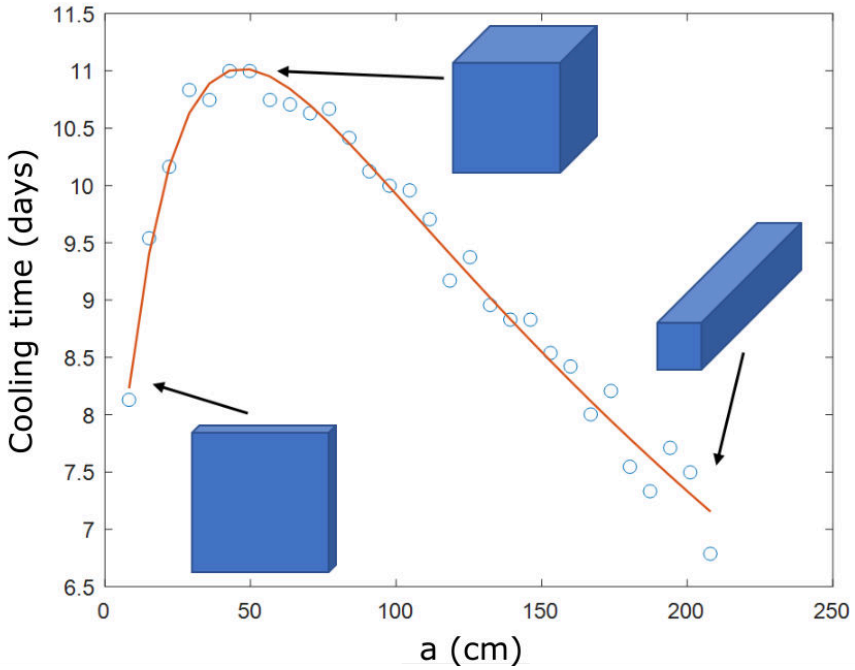


**Figure 4.11:** Simulated cooling time as a function of the geometric parameter $a$. The red curve is fit of the simulated data with the double exponential function defined in Eq. (4.7).

dimensions, which range from 10 to 120 cm, the relative variation of the cooling time can reach the 20%.

### 4.3.5 Estimation of the brick cooling time considering its shape

In section 4.3.4 we showed the significant effect of the brick shape on its cooling time. Therefore, we aimed to introduce a new prescription for the estimation of the cooling time able to take into account not only the mass of the block, but also its shape. To do that we considered as an example the results reported in Fig. 4.11, where we simulated the cooling times for parallelepipeds sharing the same volume but with different dimensions. In that simulation two of the three dimensions of the block are kept equal. Since we considered a brick with fixed volume $V$, only one parameter (which we called $a$) is independent. These results can be easily generalized to a parallelepiped with independent dimensions, obtaining the block cooling time dependence on all the dimensions of the block. The cooling time of the block as a function of the dimension $a$ shown in in Fig. 4.11 has been fitted by a double exponential equation of the form:

$$\Delta t(a) = c_1 e^{c_2 a} + c_3 e^{c_4 a}, \tag{4.7}$$

where $c_1$, $c_2$, $c_3$ and $c_4$ are the fit parameters. The result of the fit is the red curve reported in Fig. 4.11. We already noticed that the parallelepiped requiring more time to cool down is the cube, since it is the shape with the smallest surface to volume ratio. For this reason we can introduce the cube cooling time $\Delta t_{cube} = \Delta t(a = \sqrt[3]{V})$ as a reference. At this point, it is possible to define for the generic block of height $a$ and volume $V$ the adimensional factor $\eta_V(a)$ as follows:

$$\eta_V(a) = \frac{\Delta t(a)}{\Delta t_{cube}}. \tag{4.8}$$

This factor relates the proper cooling time of a generic block of depth $a$ and the cooling time of the cube with the same volume. Clearly, it always occurs that $\eta_V(a) \leq 1$, and the equality is valid for a cubic block. As an example, the factor $\eta_V(a)$ is evaluated in Tab. 4.3 for parallelepipeds with different dimensions. We can see how, especially for very elongated blocks, the factor $\eta_V(a)$ can be significantly smaller than 1.
The procedure that the company is currently using assumes that blocks with the same mass need the same time to cool down. However we noticed from the simulations that, among the parallelepipeds, the cube is the shape requiring the largest cooling time. Therefore, in a very conservative way, we can consider the time $T_0$ that is currently used by the company as the proper time for the cooling of a cube. This time can be taken directly by an interpolation of table which the company is currently using to estimate the cooling time of the blocks. Therefore, once that $\eta_V(a)$ is known from the simulation, the new cooling time $T^*$ can be evaluated as the product $T^* = \eta_V(a)T_0$.
As we already discussed, this model has been studied for parallelepipeds where two dimensions are kept equal. However, this model can be easily generalized to a generic parallelepiped, providing a way to evaluate the factor $\eta_V(a, b)$ (in this case the third dimension of the block is fixed by the other two dimensions and its volume). In this general case, once that the factor $\eta_V(a, b)$ is tabulated for the different possible volumes and dimensions of the brick, it can be used for the evaluation of the proper cooling time of the block taking into account also its shape. Moreover, the model can be generalized to blocks with other shapes (such as, for example, the spheres). We emphasize that, as it results from Fig. 4.11, for some blocks the cooling time can be reduced of more than 20%.

### 4.3.6 The role of the alumina volume

The model introduced in section 4.3.3 can be used to investigate also the second contradiction introduced in section 4.3.2. This contradiction refers to the counter intuitive behavior exhibited by the cubes in Fig. 4.7, in which the one with the largest volume (hence mass) show a lower cooling time with respect to the lightest one. Following the same approach used in section 4.3.4, we simulated the cooling curves of cubes of different volumes when they are immersed in a thermal bath of alumina, and from these we extracted the cooling times. The result of this simulation is shown in Fig. 4.12. As one can appreciate, the time needed for the cooling of the block monotonically increases with the volume of the cube,

| Mass (kg) | $a$ (cm) | $b$ (cm) | $\eta_V(a)$ |
|---|---|---|---|
| 288 | 80 | 30 | 0.87 |
| 300 | 40 | 40 | 1.00 |
| 150 | 20 | 10 | 0.97 |
| 250 | 40 | 15 | 0.93 |
| 450 | 80 | 50 | 0.92 |

**Table 4.3:** Cooling times for parallelepipeds with squared basis of side $b$ and depth $a$. The time reduction factor $\eta_V(a)$ relates the cooling time actually used by the company to the one that can be used considering the brick shape.

following what is expected by intuition. By the way, this does not solve the issue. This fact suggests that the contradiction should arise from an effect which has not been considered in our model.

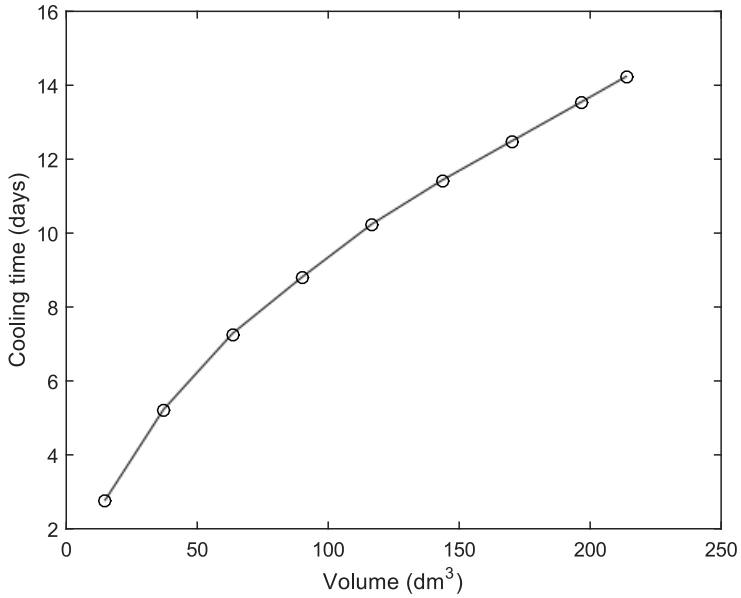


**Figure 4.12:** Simulated cooling times of cubes as a function of their volume. The model considers the block immersed in a thermal bath of alumina.

So far, the influence of the finite size of the alumina which covers the block has been neglected by considering it as immersed in a thermal bath. In this way, border effects are decoupled from the volume and the shape of the brick. In order to investigate the impact of this approximation, we simulated the cooling times as a function of the thickness of alumina from the edges of a parallelepiped of dimension $(60 \times 40 \times 40)$ cm$^3$, keeping the volume of the latter constant. The result is shown in Fig. 4.13, and indicates that the cooling time is increased by the thickness of the alumina. The company indicated the typical variation of the

alumina layer thickness as ranging from 20 cm to 60 cm. In this interval, the cooling time increases by more than the 50%. From 80 cm to higher thickness, the effect is less remarked, with an increase of less than the 10%. This simple analysis points out that the finite volume of alumina strongly influences the cooling rate. Therefore, one has necessarily to consider this effect to correctly model and quantitatively predict the cooling time.

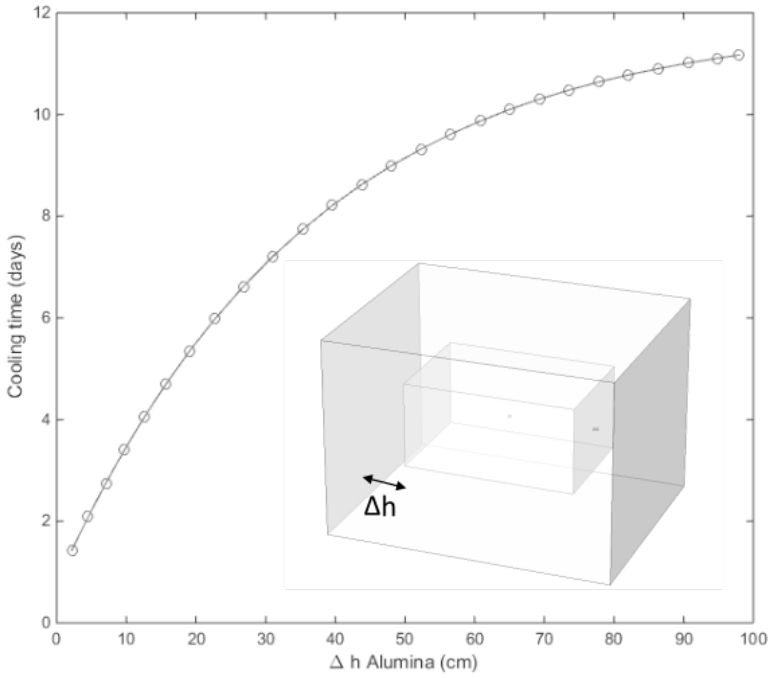


**Figure 4.13:** Simulated cooling time of a parallelepiped of dimensions $(60 \times 40 \times 40)$ cm$^3$ as a function of the thickness $\Delta h$ of alumina (this quantity is shown in the inset).

Due to this fact, we performed a simulation in which the volume of the cube is changed while the one of the alumina is fixed to $(160.6 \times 110 \times 75)$ cm$^3$. This is the volume of the boxes used by the company for the cooling process of the bricks. We also compared the cooling times of the cubes with the ones of parallelepipeds of equal volumes, in which the three edges are $a = \gamma a_0$, $b = \gamma b_0$ and $c = \gamma c_0$, being $a_0 = 60$ cm, $b_0 = 40$ cm, $c_0 = 30$ cm and $\gamma$ a common scaling factor. The results are shown in Fig. 4.14. For both shapes, we have a monotonic increase of the cooling time with the volume up to 150 dm$^3$. Then, for larger volumes, the cooling time starts to decrease, even if the mass is still increasing. This constitutes a big discrepancy with respect to the results shown in Fig. 4.12, in which borders effect are neglected. The curves shown in Fig. 4.14 can be interpreted

in this way: for small volumes ($< 30$ dm$^3$, which corresponds to about 150 kg), the bricks behave as if they were immersed in a thermal bath of alumina, so their cooling time increases with the mass. Then, as the volume further increases, the effect of the finite size of the alumina starts to manifest. At very large volumes ($> 200$ dm$^3$, corresponding to about 800 kg), the heat capacity of alumina is so small that it is no more able to act as a thermal buffer, and the heat is rapidly dissipated by convection into the external environment. This happens with a rate which is sufficient to overcome the concurrent increase of the heat capacity of the bricks. In general, parallelepipeds cool faster than cubes, due to their higher surface to volume ratio. Therefore, Fig. 4.14 explains the apparent contradiction reported at the beginning of this section: cubes with larger volumes can cool faster than cubes with smaller mass because of the reduction of the heat capacity of alumina.

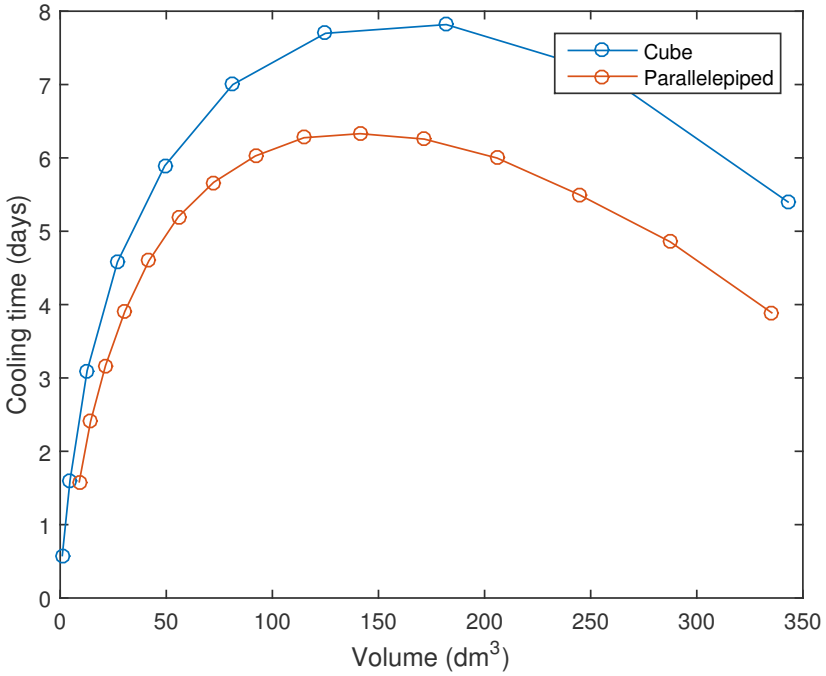


**Figure 4.14:** Simulated cooling time of cubes and parallelepipeds as a function of their volume. The blocks are immersed in a box of alumina of dimensions $(160.6 \times 110 \times 75)$ cm$^3$.

### 4.3.7 The role of the brick position

The results of section 4.3.6 and of Fig. 4.13 indicate that the thickness of alumina plays a crucial role in determining the cooling rate. It is then expected that this would be also a function of the position of the brick inside the box. In order to investigate this fact, we simulated the cooling times of a brick of dimension

$(60 \times 40 \times 40)$ cm$^3$, lying in a box of alumina of size $(160.6 \times 110 \times 75)$ cm$^3$, for different positions of the brick center with respect to the one of the box. As it is sketched in Fig. 4.15(a), the horizontal position spans the interval $[0 - 50]$ cm, while the vertical position spans the interval $[0 - 35]$ cm. In Fig. 4.15(b) the relative cooling times with respect to the central position ($(X, Y) = (0, 0)$) are reported. The cooling rate is minimum at the center of the box, since it is the point where the average distance from the edges of the box is maximized. As the brick approaches the vertical or the horizontal edges of the box, the cooling rate increases, reaching a maximum when a face of the brick comes into contact with one of the box. As it is shown in Fig. 4.15(b), it is possible to displace the horizontal position of $\sim 35$ cm and the vertical position of $\sim 17.5$ cm keeping the cooling rate variation below the %5 with respect to the central position. This gives an important indication on the tolerances with which the bricks can be positioned inside the cooling box.

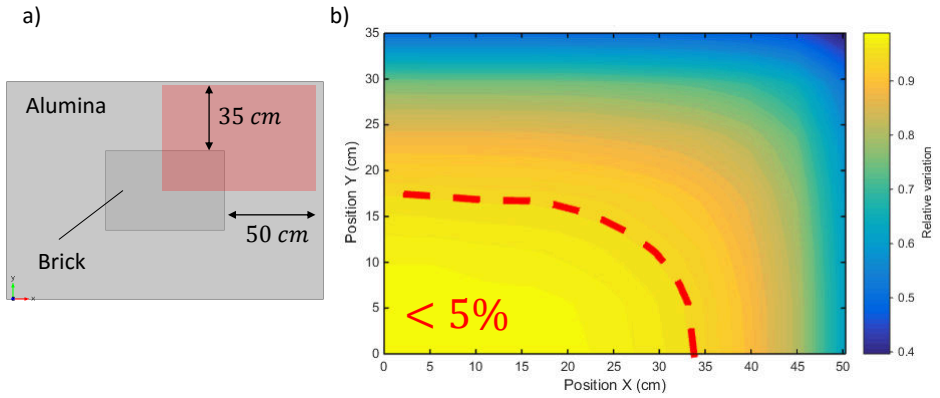


**Figure 4.15:** (a) Geometry of the simulation and distance from the brick faces to the edges of the external box. (b) Simulated cooling time of a parallelepiped of dimension $(60 \times 40 \times 40)$ cm$^3$ in a box of alumina of dimension $(160.6 \times 110 \times 75)$ cm$^3$. The $X$ and $Y$ positions refer to the displacement of the center of the brick with respect to the one of the box.

## 4.4 Conclusions

During the IPSP2016 week, the team working on the problem proposed by SEPR Italia was divided into subgroups, each devoted to the analysis of one of the two parts of the problem proposed by the company.
Regarding the first part, we were able to evaluate alumina as the best insulating material for the purposes of the company. In fact, even if its thermal conductivity can be compared to the one of diatomaceous earth, it is about 4 times smaller than the one of vermiculite. Moreover, we observed that the heat propagation velocity in alumina is slower than both in vermiculite and diatomaceous earth. This fact is due to the different thermal inertia of the materials, which is in turn due to their different specific heats. Therefore, being the company interested in

having a slow cooling process, alumina can be considered as the best material for their purposes, both in terms of thermal conductivity and thermal inertia.
Regarding the optimization of the cooling process of the blocks, we proposed two novel storage mechanisms that provide a reduction of the mean storage time of the blocks. The first mechanism is still based on the block mass and ensures that, increasing the number of categories that determine the block cooling times, the average cooling time can be reduced of about 9%. The second mechanism is based on the finite element model that we performed, and introduces the block shape as a crucial parameter in the determination of its cooling time. About this fact we estimated that, for the more elongated blocks, the cooling time can be reduced of more than 20% by taking into account their shape.
In the end we also analyzed a problem that the company was not taking into account, which is related to the role of the correct positioning of the brick in the cooling box. From this analysis we established the crucial role of the amount of insulating material around the block. If this fact is missed, the cooling process for the larger bricks can speed up without control, causing the formation of cracks that can strongly affect the block quality.

# Bibliography

[1] More information at `https://www.saint-gobain.com/en`.

[2] More information at `http://www.sefpro.com/en/sepr-italia.aspx`.

[3] Healy, J. J., De Groot, J. J., Kestin, J. (1976). "The theory of the transient hot-wire method for measuring thermal conductivity". Physica B+ C, 82(2), 392-408.

[4] Davis W. R., "Hot-Wire Method for the Measurement of the Thermal Conductivity of Refractory Materials". In Magli K D, Cezairliyan A, Peletsky V E, (Eds.) Compendium of Thermophysical Property Measurement Methods, Vol. 1 Survey of Measurement Techniques, 1984, New York, London, Plenum Press, p. 161.

[5] Carslaw, Horatio Scott, and John Conrad Jaeger. "Conduction of heat in solids". Oxford: Clarendon Press, 1959, 2nd ed. (1959).

# CREDITS

## The entire group at the opening day

**From left to right:** T. Pradella, B. D'Emilio, L. Giusti, A. Lugnan, A. Marchesini, C. Nidasio, E. Mulas, C. Corrà, G. Giacomozzi, M. Eccel, M. Barbiero, P. Beraldini, M. Quaglia, M. Compri, A. Gaspari, G. Germogli, D. Covi, S. Biasi, C. Piotto, R. Isola, S. Piccione, A. Mazzi, G. Tait, A. Cernuto, T. Chalyan, A. Zanolli, C. Mordini, E. Fava, A. Saha, M. Rossignoli, M. Cervino, M. Brighenti, C. A. Maestri, M. Borghi, C. Pross, Z. Bisadi, S. Leoni, S. Signorini, D. Roilo, S. Chinellato, M. Bertolla, C. Castellan

*Foto Giuseppe Froner - Archivio Università di Trento*

## Arconvert team

**From left to right:** C. Castellan, M. Bertolla, C. Piotto, C. A. Maestri, A. Mazzi, R. Isola, D. Roilo, A. Cernuto, M. Mancinelli, C. Corrà, A. Lugnan

*AgF Bernardinatti Foto - Archivio Università di Trento*

## Bonfiglioli Mechatronic Research team

**From left to right:** D. Roilo, C. Castellan, E. Mulas, A. Marchesini, M. Barbiero, M. Bertolla, C. Mordini, G. Giacomozzi, M. Quaglia
**Not in figure:** E. Fava

*AgF Bernardinatti Foto - Archivio Università di Trento*

## Eurotex Filati team

**From left to right:** M. Compri, C. Castellan, P. Beraldini, A. Gaspari, S. Biasi, D. Roilo, M. Bertolla, Z. Bisadi, S. Piccione, T. Chalyan


*AgF Bernardinatti Foto - Archivio Università di Trento*

## Sepr Italia team

**From left to right:** D. Roilo, A. Saha, M. Rossignoli, M. Brighenti, G. Germogli, M. Cervino, M. Bertolla, C. Castellan, S. Signorini, M. Borghi


*AgF Bernardinatti Foto - Archivio Università di Trento*

# ACKNOWLEDGMENTS

First of all we would like to thank the co-organizers of IPSP2016. The Department of Physics and the Doctoral School in Physics of the University of Trento, represented by Prof. Lorenzo Pavesi and Prof. Giovanni Andrea Prodi respectively, for supporting the whole event. The Research Support and Knowledge Transfer Division of the University of Trento that helped us in the first contacts with the companies and in the field of intellectual properties, in particular dott.ssa Vanessa Ravagni, ing. Claudio Nidasio, ing. Massimo Eccel and dott. Lino Giusti. Confindustria Trento in the person of dott. Alessandro Santini, that assisted us in finding some potential participating companies. Trentino Sviluppo - Polo Meccatronica, represented by dott. Paolo Gregori, for his commitment in involving the companies belonging to the Polo Meccatronica.
We thank the participating companies and their representatives for trusting in the initiative, in particular Arconvert (ing. Sabrina Leoni, ing. Andrea Zanolli), Bonfiglioli Mechatronic Research (ing. Tomas Pradella), Eurotexfilati (dott.ssa Marina Mariani and dott.ssa Chiara Pross) and SEPR Italia (ing. Giorgio Tait). The young researchers that took up the challenge of IPSP2016 are worth a special mention for their hard work and the enthusiasm they have put in it.
Our sponsors helped us concretely in the organization of the event. We would like to thank our main sponsor Tecnoclima s.p.a. and the sponsors Cassa Rurale Pinetana Fornace e Seregnano, Famiglia Cooperativa di Povo, Elettrica s.r.l. and RS Components s.r.l. A special thanks goes to dott.ssa Sara Chinellato of the Communications and events office for her work, professionalism, advices and good taste. We would also like to thank those who helped us in the promotion of the event, especially dott.ssa Alessandra Saletti and dott.ssa Elisabetta Andreina Brunelli of the Press Office of the University of Trento.
We are grateful to the staff of the Didactic Laboratories, the Mechanic Service Facility, the Electronic and Designing Service and the professors of the Department of Physics.
We thank the the Department of Civil, Environmental and Mechanical Engineering (DICAM) of the University of Trento for allowing us to carry out experiments with their traction machine.
Thank you also to the Scientific Committee of IPSP2015 for passing us the torch of Industrial Problem Solving with Physics. A special thanks goes to the founders of the event: the Scientific Committee of IPSP2014.
Finally, we are thankful to all the people and friends who have supported us in the organization.

ART>UNITRENTO
March 2017

**IPSP2016**, Industrial Problem Solving with Physics, is a one-week event organized by the Department of Physics, the Doctoral School in Physics and the Research Support and Knowledge Transfer Division of the University of Trento, in collaboration with Confindustria Trento and Polo Meccatronica - Trentino Sviluppo.

4 companies and 4 groups of *brains* (master's students, PhD students and research fellows), selected among several applicants, worked together to find reliable solutions to the practical industrial problems submitted by the participating companies.

Young and motivated researchers had thus the chance to show off their own skills in tackling new practical challenges. The participating companies, from their side, obtained concrete solutions to the submitted problems and experienced an alternative problem solving strategy.

**SCIENTIFIC COMMITTEE**

**Maddalena Bertolla**, Department of Physics
**Claudio Castellan**, Department of Physics
**David Roilo**, Department of Physics

**ADVISORY BOARD**

**Lorenzo Pavesi**, Department of Physics
**Giovanni Andrea Prodi**, Doctoral School in Physics
**Vanessa Ravagni**, Research Support and Knowledge Transfer Division
**Alessandro Santini**, Confindustria Trento
**Paolo Gregori**, Polo Meccatronica

**http://events.unitn.it/en/ipsp2016**

Participant companies

ARCONVERT
Bonfiglioli Forever Forward
eurotex filati find the thread
SAINT-GOBAIN SEPR ITALIA S.p.A.

Main sponsor

tecnoclima PRESIDIO DELL'ARIA

Sponsors

CASSA RURALE PINETANA FORNACE E SEREGNANO BANCA DI CREDITO COOPERATIVO
coop Trentino
microlease
Elettrica www.elettrica.net
RS

**ISBN 978-88-8443-712-9**